Loughborough University

Thesis Access Form

Copy No……...…….**Location**……..……...…

Author Benedikt J. Knauf

Title Polymer Bonding by Induction Heating for Microfluidic Applications

Status of access OPEN / ~~RESTRICTED / CONFIDENTIAL~~

Moratorium Period:……Ø……years, ending……../……200…….

Conditions of access approved by (CAPITALS):……

Supervisor (Signature)……...……...

Department of……...……

Author's Declaration: *I agree the following conditions:*

Open access work shall be made available (in the University and externally) and reproduced as necessary at the discretion of the University Librarian or Head of Department. It may also be digitised by the British Library and made freely available on the Internet to registered users of the EThOS service subject to the EThOS supply agreements.

*The statement itself shall apply to **ALL** copies including electronic copies:*

This copy has been supplied on the understanding that it is copyright material and that no quotation from the thesis may be published without proper acknowledgement.

Restricted/confidential work: All access and any photocopying shall be strictly subject to written permission from the University Head of Department and any external sponsor, if any.

Author's signature…….Date……...……...……...

users declaration: for signature during any Moratorium period (Not Open work): ***I undertake to uphold the above conditions:***			
Date	Name (CAPITALS)	Signature	Address

Loughborough University

CERTIFICATE OF ORIGINALITY

This is to certify that I am responsible for the work submitted in this thesis, that the original work is my own except as specified in acknowledgments or in footnotes, and that neither the thesis nor the original work contained therein has been submitted to this or any other institution for a degree.

…….. (Signed)

…….. (Date)

Polymer Bonding by Induction Heating for Microfluidic Applications

by

Benedikt J. Knauf

A Doctoral Thesis

Submitted in partial fulfilment of the requirements

for the award of

Doctor of Philosophy (PhD) of Loughborough University

November 2010

Abstract

Microfluidic systems are being used in more and more areas and the demand for such systems is growing every day. To meet such high volume market needs, a cheap and rapid method for sealing these microfluidic platforms which is viable for mass manufacture is highly desirable.

In this work low frequency induction heating (LFIH) is introduced as the potential basis of a cost-effective, rapid production method for polymer microfluidic device sealing. Thin metal layers or structured metal features are introduced between the device's substrates and heated inductively. The surrounding material melts and forms a bond when cooling.

During the bonding process it is important to effectively manage the heat dissipation to prevent distortion of the microfluidic platform. The size of the heat affected zone (HAZ), and the area melted, must be controlled to avoid blockage of the microfluidic channels or altering the channels' wall characteristics. The effects of susceptor shape and area, bonding pressure, heating time, etc, on the heating rate have been investigated to provide a basis for process optimisation and design rules. It was found that the maximum temperature is proportional to the square of the susceptor area and that round shaped susceptors heat most efficiently. As a result of the investigations higher bonding pressure was identified as increasing bond strength and allowing the reduction of heating time and thus the reduction of melt zone width. The use of heating pulses instead of continuous heating also reduced the dimensions of melt zones while maintaining good bond strength. The size of the HAZ was found to be negligible.

An analytical model, which can be used to predict the heating rate, was derived. In validating the model by numeric models and experiments it was found that it cannot be used to calculate exact temperatures but it does correctly describe the effect of different heating parameters. Over the temperature range needed

to bond polymer substrates, cooling effects were found not to have a significant impact on the heating rate.

The two susceptor concepts – using thin metal layers (metal-plastic bonds) or structured metal features (plastic-plastic bonds) – were tested and compared. While the metal-plastic bonds turned out to be too weak to be useful, the bonds formed using structured susceptors showed good strength and high leakage pressure.

Based on the knowledge gained during the investigations a microfluidic device was designed. Different samples were manufactured and tested. During the tests minor leaks were observed but it was found that this was mainly due to debris which occurred during laser machining of the channels. It was concluded that induction bonding can be used to seal plastic microfluidic devices.

The following guidelines can be drawn up for the design of susceptors and process optimisation:

- Materials with low resistivity perform better;
- For very thin susceptors the effect of permeability on the heating rate is negligible;
- The cross-sectional area of the susceptor should be as large as possible to reduce resistance;
- The thickness of the susceptor should be of similar dimensions to the penetration depth or smaller to increase homogeneity of heat dissipation;
- The shape of the susceptor should follow the shape of the inductor coil, or vice-versa, to increase homogeneity of heat dissipation;
- The susceptor should form a closed circuit;
- Higher bonding pressure leads to stronger bonds and allows reduced heating times;
- Pulsed heating performs better than continuous heating in terms of limited melt area and good bond strength.

The drawbacks of the technique are explained as well: introducing additional materials leads to additional process steps. Also the structuring and placement of the susceptor was identified to be problematic. In this project the structured susceptor was placed manually but that is not feasible for mass manufacture. To be able to use the technique efficiently a concept of manufacturing the susceptor has to be found to allow precise alignment of complex designs

Keywords

Microfluidic Systems, Induction heating, Plastic bonding, Packaging, Sealing, Susceptor design

List of Publications

B.J. Knauf, D.P. Webb, C. Liu and P.P. Conway, ''Packaging of polymer based microfluidic systems using low frequency induction heating (LFIH)'', Proceedings of the 2008 International Conference on Electronic Packaging Technology & High Density Packaging (ICEPT-HDP 2008), Shanghai, PRC, July 2008, pp 1-6.

B.J. Knauf, D.P. Webb, C. Liu and P.P. Conway, ''Plastic Packaging Using Low Frequency Induction Heating (LFIH) for Microsystems'', Proceedings of the 10th International IEEE Electronics Packaging Technology Conference (EPTC 2008), Singapore, December 2008, pp 172 - 180, ISBN 9781424421183.

D.P. Webb, B.J. Knauf, C. Liu, D.A. Hutt and P.P. Conway, ''Productionisation issues for commercialisation of microfluidic based devices'', Proceedings of Microtech 2009, Edinburgh, UK, March 2009, pp 1-10.

B.J. Knauf, D.P. Webb, C. Liu and P.P. Conway, ''Packaging for Polymer Microfluidic Systems Using Low Frequency Induction Heating (LFIH)'', Proceedings of the 3rd Annual Lab-on-a-Chip European Congress (LOACEC2009), Stockholm, Sweden, May 2009, 27 pp.

D.P. Webb, P.P. Conway, D.A. Hutt, B.J. Knauf and C. Liu, ''Processes for Integration of Microfluidic Based Devices'', 17th European Microelectronics and Packaging Conference (EMPC), Rimini, Italy, June 2009, pp 1-7.

B.J. Knauf, D.P. Webb, C. Liu and P.P. Conway, ''Low frequency induction heating for the sealing of plastic microfluidic systems'', Microfluidics and Nanofluidics, vol. 9, pp. 243-252, 08/01, 2010.
DOI: 10.1007/s10404-009-0539-x

D.P. Webb, B.J. Knauf, C. Liu, D.A. Hutt and P.P. Conway, ''Productionisation issues for commercialisation of microfluidic based devices", Sensor Review, 29(4), 2009, pp 349-354, ISSN 0260-2288.

B.J. Knauf, D.P. Webb, C. Liu and P.P. Conway, “Induction Heating for Efficient Lid Sealing of Thermoplastic Lab-on-a-Chip”, Poster, Transalpnano 2010, Como, Italy, June 2010.

B.J. Knauf, D.P. Webb, C. Liu and P.P. Conway, “Polymer bonding by induction heating for microfluidic applications”, Proceedings of the 2010 Electronics System Integration Technology Conference (ESTC 2010). Berlin, Germany, September 2010, 8pp.

Pending:

B.J. Knauf, D.P. Webb, C. Liu and P.P. Conway, ''Polymer bonding by low frequency induction heating for microfluidic systems''
To be submitted to Microfluidics and Nanofluidics

Acknowledgments

The research presented in this thesis has been carried out at Wolfson School of Mechanical and Manufacturing Engineering at Loughborough University, UK. It has been sponsored by the EPSRC grand challenge project 3D-Mintegration.

The path towards this thesis spans three years of work and many people have been involved and contributed to the presented ideas and understanding gained. The author acknowledges his debt to those whose stimulations and discussions were very helpful for the realization of this project.

In particular, I wish to express my gratitude to my supervisors, Prof. Paul Conway, Dr. Patrick Webb and Dr. Changqing Liu, for their continued encouragement and invaluable suggestions during this work.

Furthermore I am deeply indebted to the technical staff and other PhD students of Wolfson School for sharing their experiences about the problem issues as well as helping to develop solutions to the identified problems. I would specially like to thank Andy Sandaver, Jagpal Singh, Yi Qin and Dave Britton for their extremely valuable experiences, support, and insights. Many others at Loughborough University that have been involved also deserve recognition but it is not possible to list them all here. Their support in this effort is, however, greatly appreciated.

Finally I want to thank my family and friends. Their encouragement and support is a powerful source of inspiration and energy.

Table of Contents

Index of Figures

1 Introduction

As micro systems are getting smaller and smaller and the environments they are used in are sometimes very harsh, the requirements of the packaging are growing. The packaging must protect the system against dirt, humidity, stresses, etc and, depending on the application, provide electrical, fluidic or optical interconnection and thermal management.

A special task is the packaging of microfluidic systems. Microfluidic systems are networks of channels with width and depth in the micron scale, designed to do continuous flow chemistry with small volumes of fluid. Microfluidic devices are also referred to as lab-on-a-chip (LOC) or, if they are more complex, micro total analysis systems (µTAS). They not only have to be protected against external influences, but also have to withstand internal pressures.

The demands on a world-to-chip interface, i.e. the interconnection scaling the fluid channels from macro down to micro dimensions and bringing them into the microfluidic system, are also different to those of “normal” MEMS. These interfaces have to be strong and flexible; they have to be sealed and must connect reservoirs of millilitres or litres to systems with a capacity of micro or even nanolitres.

Microfluidic systems are used for many different purposes and the materials being used depend on the demands of the applications. Glass is chemically inert but it is expensive and difficult to process. Silicon can be used to make active parts like micro valves or pumps but it is expensive. Polymers are capable only of passive channel networks, but due to being cheap in acquisition and easy to process, they are suited to mass manufacture.

Typically microfluidic systems are composed of platforms containing open microfluidic channel networks and/or functional parts with a lid sealing those channels, as shown in Figure 1-1a. Lid and platform have a thickness of a few

mm while the channels in the platform can have a width and depth smaller than 100µm. To be able to access the microfluidic channels holes with a diameter of about 500µm or more are formed into the lid working typically as ports for micro tubing as shown in Figure 1-1b.

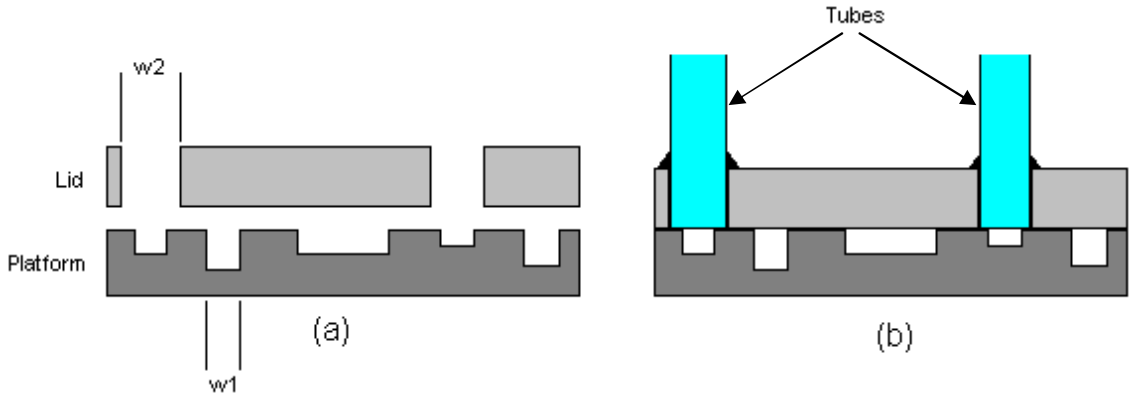

Figure 1-1. Principle of the assembly of microfluidic devices with w1 = channel width and w2 = port width

Depending on the material used, these systems can be sealed using different processes, such as anodic bonding, thermal bonding, laser bonding, and so on. The world-to-chip interface is realised by techniques that use adhesive, clamps, and interlocking structures to fix the tubes.

The processes and techniques used have differing drawbacks, such as using high temperatures and pressures, needing laboratories or microwave chambers, and changing the characteristics of the microfluidic channels. Most of the processes are cost-intensive and slow compared to other manufacturing steps, so the sealing and interfacing of microfluidic systems is the bottleneck in mass production. Hence, rapid and cheap techniques to seal and interconnect microfluidic chips are needed. A single technique able to do both sealing and interconnecting, sequentially or even at the same time, would be the optimum solution.

The focus of this project was the sealing and interconnecting of thermoplastic polymer based microfluidic systems. Thermoplastics were chosen because they

pose the best choice for large-scale production of microfluidics as they are cheap and easy to process.

Although there are few reports concerning the use of induction heating for micro manufacture, there are several reasons to believe it would make a good alternative to the common techniques for microfluidic packaging. Induction heating has been used commercially for about 60 years. The largest use is in the steel industry for hardening, melting, soldering, welding, and annealing, but more and more it is also used in other areas such as heating fillings in dental medicine, cap sealing, MEMS packaging, etc. The advantages of this technique are manifold. It is a very rapid heating process with a small scaling loss, the start-up is very fast, it is energy saving, and the technique is capable of high production rates. The most important advantages for the use of induction heating in this project are its selectivity and the reproducibility of the results.

Since polymers are non-conductive a *susceptor* is needed. A susceptor in this case is a material with the ability to absorb electromagnetic energy, i.e. a conductive material, such as nickel or steel. The idea is to use a few microns thick (structured) metallic susceptor as an intermediate layer between two substrates of the microfluidic system. The susceptor is heated inductively causing the surrounding material to melt. While cooling a bond should be created between the two substrates. Two main concepts of using susceptors can be conceived. The material can cover the whole plastic substrate, which leads to bonds between plastic and susceptor material, or the susceptor can be structured into thin metal tracks following the microfluidic channels on both sides. The latter would lead to direct bonds between the polymer substrates.

So far, either thick susceptor layers or high frequency induction heating generators have been used (see sections 2.1.2.5 and 2.2.1), but low frequency induction heating might be powerful enough to heat thin film susceptors or even structured, small area susceptors, to the forming temperature of polymers (<250℃). There are several advantages of using thi s method. Induction heating is a rapid, reproducible and highly selective heating technique. Low frequency

generators (f < 1MHz) fit into 19” racks, which makes them suitable for the use in the field, provided that access to cooling water is available, and using structured thin susceptor layers keeps the quantity of additional material in the microfluidic device as low as possible. Low frequency induction heating (LFIH) is not only a potential basis of a cost-effective, rapid production method for polymer microfluidic device lidding, it could also be used for connecting microfluidic chips to the macro world.

The aim of this project was to analyse and test the possibilities and limitations of induction heating for the sealing and packaging of polymer microfluidic systems. It was evaluated whether it was possible to heat thin film susceptors using low frequency induction heating. An analytical model to predict the heating rate in dependency of different heating parameters was derived and the functionality of small feature susceptors and the effect of small areas and different susceptor shapes and materials on the heating rate were investigated.

There were three major objectives:

1. Understanding and optimising the heating rate of the susceptor.
2. Determining whether the analytical equation is a good model for the heating rate of the susceptor
3. Understanding and optimising the formation of polymer bonds.

First a literature review was undertaken (Chapter 2) to gain some knowledge of common techniques for sealing and interconnecting of microfluidic devices. Their advantages and disadvantages were investigated to establish how this technique is used at the moment and to evaluate if induction bonding poses an appropriate alternative. Also, the functional principles of induction heating were reviewed to identify the parameters likely to affect the efficacy of the process.

In Chapter 3 the experimental techniques, materials and equipment used during this project are presented. The decision to use nickel as susceptor and PMMA as substrate material is explained and the two concepts of using susceptors –

whole layer vs. structured features – and the techniques to obtain them are described. Some results of this work could not be easily obtained by experiment. Hence, numeric modelling was used as a supporting technique. The last section of the chapter describes the model parameters, constitutive equations and boundary conditions.

The experimental work is described in Chapters 4-7: Chapter 4 feasibility – Chapter 5 process parameters – Chapter 6 susceptor design – Chapter 7 bonding mechanisms.

In order to undertake the work it was necessary to determine which equipment was fit for the purpose. Low frequency induction heating equipment (< 1MHz) is the most desirable from the point of view of cost but it was not clear that thin susceptors would heat adequately at this frequency range. In sections 4.1 and 4.2 the results of initial trials and feasibility testing with low and high frequency equipment and different susceptors is reported. As a result of the trials the use of low frequency induction equipment was judged to be feasible.

In Chapter 5 the experimental, numerical and theoretical investigations of the effects of LFIH process parameters, such as heating time, working distance and output current on the heating rate are reported. In a first approach to describing those effects, basic physical equations were used to estimate the dependence of the heating rate on the different process parameters (Section 5.1). The assumptions were first compared with the results of numeric models and then validated experimentally. But knowing the basic dependencies is not enough, as there are also interdependencies between the parameters. An analytical model including all variable parameters was needed. Such a model could not be found in the literature hence it had to be derived and validated by experiments (see Section 5.2). In Section 5.3 the temperature dependency of resistivity is discussed and added to the model. Also, it had to be considered if high resistivity leads to higher temperatures. This is examined in Section 5.4. The last section of Chapter 5 deals with cooling effects, as they were not considered in the model.

The analytical model could be used to estimate the behaviour of the heating rate when certain parameters were altered but the model ignored a very important ‘external’ parameter: the susceptor design. The effects of susceptor area and shape had to be investigated in order to optimise the heating process. In Section 6.1 the dependence of heating rate on susceptor area was compared with the predictions of the analytical model. Then experiments were made, heating round, square and triangular shaped susceptors and susceptors of different sizes and the heating rates were also compared. In Section 6.2 the assumption that cooling effects do not have an impact for the temperatures used for polymer bonding was confirmed by analysing the previous experiments.

Investigations of the mechanisms of polymer bond formation are reported in Chapter 7. First it was investigated how the flatness and cleanness of the substrates might affect the heating and bonding process by creating thermal barriers. Bond strength, melt zone, bond area and HAZ then were measured and compared. In previous experiments the susceptors were found to reach temperatures above 200℃ rather quickly. The proces s was optimised by using heating pulses instead of continuous heating, to avoid burning the polymer while supplying a temperature above the glass transition point throughout the bonding process. The concept of using a whole layer susceptor was then tested. PMMA substrates were bonded with different parameters. Having established the effects of different bond parameters and knowing that a structured susceptor was needed to gain proper bond strengths, a microfluidic device was designed, manufactured and tested.

In the final chapter (Chapter 8) conclusions are drawn as to the optimisation, and to the advantages and disadvantages of the low frequency induction heating for thermoplastic microfluidic packaging. The technique is also compared to current alternatives and an outlook of what further development is required to make the technique fit for industrial use is provided.

2 Literature Review / Technical Background

In order to develop a new technique for the bonding of microfluidic systems it is critical to know the background of the subject. In this chapter it is reported where microfluidic systems are being used and how they are manufactured. Common techniques for sealing and interconnecting of microfluidic devices are described and their advantages and disadvantages are investigated to establish if induction bonding presents an appropriate alternative and how this technique is used at the moment. Also, the principles of induction heating are reviewed to establish what variables had to be considered in its application.

2.1 Microfluidic Systems

Nowadays microfluidic systems can be found everywhere. Ink-jet printers rely on the technology as well as micro fuel cells and many applications in biotechnology, such as chips for environmental monitoring [1], for analysing DNA, proteins, cells [2], and so on. In the automotive industry microfluidics find their application in fuel injection, oil quality monitoring, exhaust gas analysis, and they can be used for local cooling of electronics. Microfluidics are used in analytical chemistry for chemical monitoring [3], micro reactors and mixers. They are used for drug delivery and diagnostic systems (e.g. blood sugar or alcohol tests) in medical applications and even agriculture benefits from the technology, with micro lubrication devices for instance. High pressure systems are used in micro engine and micro rocket devices [4] and for high precision spacecraft thrusters.

As micro system technology becomes more and more sophisticated, more functions can be integrated in microfluidic systems. They are no longer designed for single tasks, like mixing liquids, but contain mixers, micro pumps, valves, reaction chambers, opto-electrical analysis systems [5], micro dispensers, heaters, filters, and are able to do complete analysis or processing

(micro separation, mixing, etc.) of a liquid. These systems are referred to as a lab-on-a-chip (LOC) or micro total analysis system (µTAS). For instance, the “smart pill” is such a highly integrated system, analysing the environment and dispensing drugs at appropriate times in appropriate volume.

2.1.1 Manufacturing of Microfluidic Systems

Most of the manufacturing principles of microfluidic systems are similar, no matter which material they are made of. One or more microfluidic platforms containing channels and/or functioning parts, e.g. piezoelectric materials, are sealed with lids. The manufacturing processes depend on the material and the function of the microfluidic platform. As this is not the main topic of this report only a brief review is given here for context. Although it is easy enough to make/interconnect microfluidics, the difficulty is to do it cheaply in mass manufacture. Also, it is difficult to find reports of commercial manufacturing/interconnecting of microfluidic systems so almost all of the papers mentioned in this report are academic.

For Silicon/glass based systems etching is the method of choice for creating microfluidic channels and structures. All bulk etching processes, such as buffered oxide etching [6], HF etching [7], dry etching [8], deep reactive ion etching [9] and many more can be used showing different advantages (like high aspect ratio) and disadvantages (e.g. isotropic etch distribution).

Polymer based systems are easier to process. Depending on the application there are plenty of polymers that can be used. As shown in Figure 2-1, S. Garst et al. provide a good overview of the properties of polymers [10].

Figure 2-1. Properties of polymers [10]

As polymers have a low forming temperature, hot embossing is a good method to create microstructures, e.g. channels, in the substrate [11]. First, a negative stamp has to be manufactured. With application of heat this stamp is pressed into the polymer forming the structures as shown in Figure 2-2.

Figure 2-2. Hot embossing process [11]

As the most time consuming step is the machining of the stamp this method is appropriate for mass production.

Casting polymers over a master, as described by D.C. Duffy et al., is also a method for fabricating microfluidic platforms [12]. First a master is made by rapid prototyping and prepolymer is poured over it. After curing the prepolymer

the master can be removed and the microfluidic platform can be sealed (see Figure 2-3).

Figure 2-3. Process steps of the polymer casting technique [12]

This method is good for manufacturing single systems for test issues but as the whole process takes about 24 hours it is only fit for limited service in mass production.

A similar procedure that can be used for mass production is injection moulding. The master is put into a chamber and polymer is injected as shown in Figure 2-4. After cooling the ready-made microfluidic platform can be released and the process can start again.

Figure 2-4. Principle of injection moulding [13]

Despite these replication techniques there are many other methods to create structures in polymer microfluidic platforms. Laser ablation [14], oxygen plasma etching, and liquid photo polymerization [13] are only three to mention.

SU-8, an epoxy polymer that is not listed in Figure 2-1, was used by S. Tuomikoski to manufacture microfluidic systems [13]. SU-8 was patterned lithographically and even multilevel structures were possible.

To get more complex channels J.R. Anderson et al. developed a procedure they called the “membrane sandwich” method [15]: a membrane with channel structures was sandwiched between two thicker slabs providing structural support. To demonstrate the capability of this method Anderson et al. created “basket weave” structures (see Figure 2-5) by filling the channels and removing the top slab and the membrane.

Figure 2-5. "Basket weave" structures [15]

Again, this is a method for rapid prototyping single systems. It is not capable of being used for mass production.

In this project the focus is put on polymer based systems. Polymers are taking an increasing market share of microfluidics for many reasons. Polymers are easier to process and cheaper than glass or Silicon and many of them are transparent to white light, that makes them attractive for analytical applications.

They are benign to most of the liquids used in medical applications and as there are many methods for low cost mass production of microfluidic platforms the financial aspect is a major reason for this trend [16].

2.1.2 Sealing of Microfluidic Systems

Sealing of microfluidic systems can be regarded as first level packaging. Hence, many common packaging methods of MEMS can be used for that purpose.
A requirement for this packaging is to make the microfluidic system leak-proof and protect it from the outside world's influences. The method must not cause a blockage of the microfluidic channels or change their wall properties. If an additional material is used, it must be benign to the fluids/materials used in the system's application.

2.1.2.1 Adhesive / Thermal Bonding

Thermal bonding uses heat and pressure to create a bond between the same or different material. As the name implies, adhesive bonding uses adhesives as the bonding agent. Pressure, heat, UV light etc. may be needed to create the bond. If adhesive bonding is used to seal microfluidic devices the main issue is to prevent the adhesive from blocking the channels.

Both bonding techniques are presented together in this section as it is often not possible to distinguish whether a method should be categorised as adhesive or thermal bonding.

C.H. Lin et al. developed a method for sealing PMMA based microfluidic systems in 7 minutes at room temperature [17]. First the substrates' surfaces were cleaned using acetone. Then a few drops of the bonding solvent (DE-20; 20% 1.2-dichloroethane and 80% ethanol) were applied to the contact surfaces of the substrates. The layers were clamped between two glass slides to keep

them parallel and a pressure of approximately 10 N/cm^2 was applied, as shown in Figure 2-6. After 5 minutes the clamp was removed and the remaining solvent was removed from the micro channels using vacuum suction.

Figure 2-6. Schematic illustration of solvent bonding process [17]

According to the authors the bond withstood pressures, on average, of 3.8MPa. This bonding method is rapid, provides good bond strength and as it can be carried out at room temperature there is no thermal stress occurring. The major drawback is the limitation to PMMA based systems.

S. Lai et al. presented a bonding technique for microfluidic devices called resin – gas injection [18]. Both layers of the system were clamped together before the bonding agent was injected to fill all channels, reservoirs and the gap between top and bottom layers. Nitrogen gas was then pumped into the microfluidic channels and reservoirs to replace most of the resin. The residual resin was cured using UV light.

Figure 2-7. Schematic of resin - gas injection bonding [18]

As shown in Figure 2-7b, the bonding agent could also be cured locally for wall modification/functionalisation. The uncured resin then had to be flushed out.
Lai did not mention the resultant bond strength but several biomedical experiments were performed, for which the microfluidic chip did not show any leakage.

J. Oberhammer and G. Stemme used benzocyclobutene (BCB) contact printing for full-wafer adhesive bonds [19]. Soft cured BCB spacers slightly larger than the MEMS structure were fabricated on a substrate. Liquid BCB was put on top of the spacers using an auxiliary substrate and a Pyrex slide was used as a lid. After curing the BCB with application of pressure and temperature (250℃) the overlapping Pyrex was cut (see Figure 2-8).

Figure 2-8. Process flow of the packaging technique [19]

When performing tensile strength measurements the average bond strength was able to withstand 11.34MPa. This is a very good result for an adhesive bonding process but due to the high temperatures used during curing the method cannot be used for polymer based microfluidic systems.

SU-8 and PMMA can be used as intermediate layers to seal microfluidic systems, as reported by B. Bilenberg et al. [20] (see Figure 2-9). The microfluidic platform was composed of structured SU-8 on a Pyrex glass slide. SU-8 / PMMA was spun onto Pyrex lids working as intermediate layers. The substrates were brought together and several bond processes were carried out using a temperature between 50℃ and 150℃ and a bo nding load between 1000N and 2000N.

Figure 2-9. Assembly with intermediate layer: (a) PMMA and (b) SU-8 [20]

The maximum bond strength for the system with an SU-8 intermediate layer was determined to be approximately 14MPa – thereby a bonding pressure of 1000N was used at a bonding temperature of 90°C. Using PMMA as the intermediate layer the maximum bond strength was achieved at application of a bonding pressure of 2000N and a temperature between 110°C and 120°C during the bonding process. The system withstood pressures of up to 16MPa.

K.W. Oh et al. spun Teflon-like polymer onto silicon and glass slides to use it as bonding agent [21]. The bond was created at a pressure of 4MPa and a bonding temperature of 160°C and was made for silicon-silicon, silicon-glass and glass-glass constructions. The method could be used for modular assembly of microfluidic systems as shown in Figure 2-10.

Figure 2-10. Modular assembly of microfluidic systems using Teflon bonding [21]

The best result was achieved with Silicon-Silicon systems which could withstand pressures of up to 4.3MPa.

Z. Chen at al. used thermal bonding to build up a PMMA based microfluidic system [22]. A PMMA sheet on a glass layer was put onto an imprinted PMMA slide and the whole assembly was put into a 112℃ oven at a vacuum pressure of 10mbar. This led to a tight bond between the two PMMA sheets (see Figure 2-11).

Figure 2-11. Bonded PMMA micro device [22]

The bond strength was determined to be 153kPa.

To lower the temperature during bonding G. Chen et al. used in situ polymerization to join two PMMA layers [23]. A PMMA layer was coated with MMA and clamped onto another PMMA slide with micro channels. The assembly was put into a convection oven and the bond was created at a temperature of 95℃ which is lower than the glass transition temperature of PMMA (105℃).

Another approach to lower temperature was made by R.T. Kelly and A.T. Woolley [24]. They clamped a blank PMMA layer and one with micro channels together and put the setup into boiling water for about one hour. The so bonded system had a failure pressure of 130kPa and had the advantage to stay hydrated throughout the assembly process, which might be useful for permanent incorporation of membranes into microfluidic systems.

D. Sparks et al. used a metal ring around a micro machine and a congruent solder layer on a cap wafer to create a vacuum seal for MEMS [25] (see Figure 2-12). Cap and device wafer were brought together and heated up (oven or heat plate) causing the solder to reflow.

Figure 2-12. Cross section of the solder bonded device [25]

After cooling down, the solder bond sealed the MEMS hermetically and was able to sustain a vacuum pressure of about 200Pa inside the cavity.

2.1.2.2 Laser Welding

In laser welding two layers are brought together and compressed with a certain pressure (~ 0.5-10MPa). A laser beam goes through the first, transparent, layer and gets absorbed at the junction to the second, opaque layer. This causes local fusion bonding or creates a bond between the layers by melting their surfaces as shown in Figure 2-13.

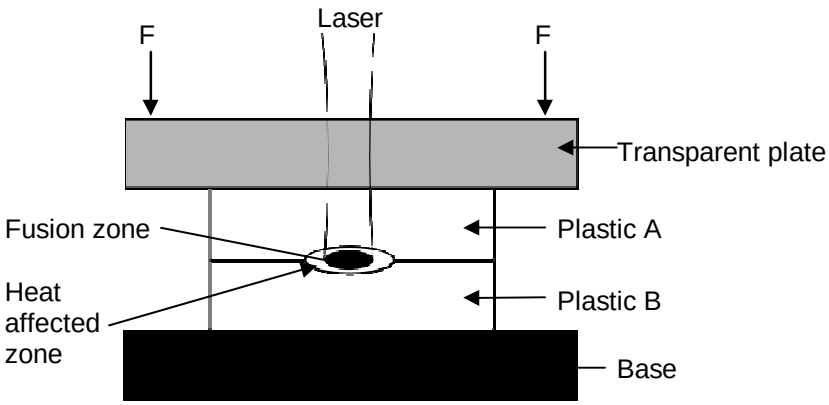

Figure 2-13. Principle of laser welding, re-drawn from [26]

According to J. Lai at al. heat influence on the peripheral zone can be ignored due to the laser dwell time being very short [26]. They bonded two PMMA layers – the bottom one was coloured to be opaque to the laser – using laser welding and found their system to be able to withstand pressures of up to 32MPa, depending on surface status, bonding velocity, laser power, and applied pressure.

Laser welding can be used for packaging of microfluidic systems constructed from different materials like polymers, glass, and metal [27; 28].

2.1.2.3 Ultrasonic Welding

The principle of ultrasonic welding is the transmission of high frequency sound vibrations to the bond area. This melts the plastic just enough to create a bond. [29, p.8].

H. Kuckert et al. used this method to bond a 0.5mm thick metal sheet onto a glass substrate [30]. The joining partners were positioned on an anvil with a static pressure of 20 to 60MPa. The sonotrode, oscillating because of the movement of the converters (20kHz piezoelectric effect), was brought into contact with the metal sheet bonding it to the glass layer (Figure 2-14).

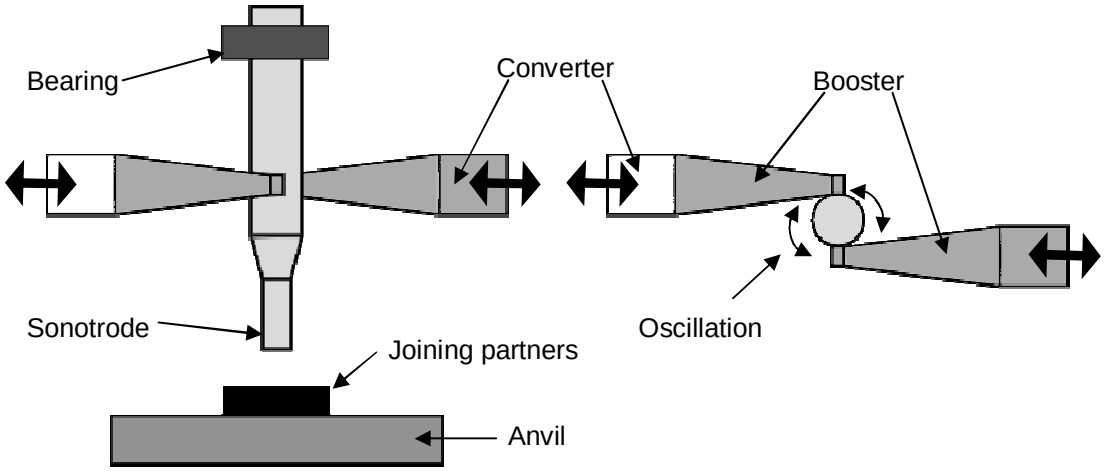

Figure 2-14. Arrangement of the oscillation generation and the positioning of the joining partners, re-drawn from [30]

The bond thus created was able to withstand pressures of up to 20MPa.

2.1.2.4 Microwave Bonding

Microwaves can be used in various ways for packaging microfluidic systems. They can create a plasma, cleaning and activating the surfaces of polymer substrates, or heat up conductive parts of the system making the surrounding material melt and creating a bonding area.

A.Y.N. Hui et al. activated the surfaces of two PDMS slabs in a microwave plasma chamber [31]. The surfaces were brought together directly after plasma treatment to form an irreversible seal (Figure 2-15).

Figure 2-15. Schematic diagram of the plasma chamber [31]

The microfluidic devices manufactured with this method had a maximum leakage pressure of 290kPa. This method was also mentioned by P. Miller et al. [32]. They had already conducted some experiments with microwave conductive powder and polymer, but decided instead to focus on plasma activation of surfaces to create bonds.

N.K. Budraa et al. used microwave heating to bond 5mm x 5mm MEMS test pieces [33]. The test pieces were silicon dies with gold frames and every bond was made with two of them. The gold frames were put together and melted due to absorption of the microwave energy. The bonds so created withstood a pressure of more than 410kPa without showing leakage.

Gold as a susceptor was also used by K.F. Lei et al. [34]. They bonded PMMA to PMMA and Silicon by covering the material with gold as shown in Figure 2-16. The gold layers were melted and formed a bond during cool down. As there were problems with the flatness of the PMMA substrates a tin-lead preform was used for the PMMA-Silicon bond.

Figure 2-16. Illustration of die stack: (a) PMMA-PMMA bond and (b) Si-PMMA bond [34]

The bonded microfluidic systems were able to withstand a pressure of more than 685kPa.

A similar method was used by A.A. Yussuf et al. [35]. They did not use a conductive layer but channels adjacent to the microfluidic channels filled with a conductive polymer (Polyaniline) as shown in Figure 2-17.

Figure 2-17. Cross-section of the setup: (11) microfluidic channel, (15) channels filled with Polyaniline [35]

Yussuf improved this method by using a screen printing technique to deposit the Polyaniline [36]. This removed the need for channels containing the

conductive polymer as it could be printed along the microfluidic channels directly (see Figure 2-18).

Figure 2-18. SEM images of the sealed channels (cross-section view) [36]

Bond strength tests were made for PMMA and PC substrates. Average bond strength of PMMA substrates was about 1.918MPa and 1.43MPa for PC.

2.1.2.5 Induction Bonding

Induction heating has already been used for packaging of MEMS. The drawbacks of the methods used so far were the requirement for either thick susceptor layers or high frequencies.

H.A. Yang et al. used Ni/Co spacers and a Sn/Pb solder to bond Silicon to Silicon or glass [37]. Spacers with a height of more than 40µm were manufactured and a 10µm thick solder was electroplated on top of them. A coil generated an alternating magnetic field of 100kHz which caused the spacer to heat up and melt the solder as shown in Figure 2-19. During cooling down the solder created a bond between spacer and lid.

Figure 2-19. Packaging of MEMS using induction heating [37]

The maximum bond strength achieved between Silicon and Silicon wafer was higher than 18MPa.

W. Suwanwatana et al. al used induction heating to bond thermoplastic composites [38]. A 250µm thick matrix of polymer and nickel granules was used as the susceptor and was heated and melted by an alternating magnetic field with a frequency of 2.25MHz (Figure 2-20).

Figure 2-20. Experimental setup for induction bonding process [38]

Only vacuum pressure was applied to the work piece. The generated bond strengths were comparable to autoclave welded systems that had bond strengths of more than 20MPa.

As well as the use of induction heating for packaging MEMS there has been some work done to characterise the behaviour of MEMS and micro/nano particles in an alternating magnetic field.

Suwanwatana's group, for instance, studied the influence of particle size [39] and oxidation effects [40] on hysteresis heating. They found a matrix with nano scale nickel particles exhibited a better heating rate than a matrix composed of the same volume of nickel but with micro scale particles. The effect of oxidation seemed to be significant for all particles, with diameters between 0.7µm and 79nm being the worst.

H.A. Yang et al. investigated the heating rate for microstructures with different shapes and thicknesses [41]. As expected, the heating was more efficient for thicker structures in a round shape. This design allowed the current to flow more efficiently.

A means of using metallic particles shaped like flakes to heat up non-conductive materials inductively was patented by Y.A. Monovoukas [42]. He recommended using different materials for every application so that the Curie temperature of the particle material controls the maximum temperature of the compound. This should prevent overheating of the non-conductive material.

2.1.3 Interconnecting of Microfluidic Systems

Another packaging challenge for microfluidic systems is fluidic interconnect. This covers both the “World-to-Chip interface” and interconnections between different parts/modules of the system. However, this only applies to continuous flow systems. Many microfluidic applications such as lab-on-a-chip type diagnostic systems rely on capillary forces to draw in droplets of analyte fluid placed in an inlet reservoir.

For applications where the liquid is brought into the microfluidic system by a pipette, there has been some work done to optimise the system to reduce the pipette steps [43] or to simplify the sealing of unused ports in multi inlet systems [44]. However there are many implementations of microfluidics where these manual steps are not suitable or even impossible, so alternative methods are required. A connection to the outer world – a world-to-chip interface – is needed, which can feed and discharge the microfluidic system directly.

The world-to-chip interface has to be capable of scaling the fluids from the reservoir volume (ml or l) down to the capacity of the microfluidic system, which is in the range of µl, nl or even smaller. Hence it must withstand pressures from a few kPa to up to several MPa, depending on the application. It should have as little dead volume as possible and should be removable without destroying the microfluidic system.

Interconnections between different microfluidic modules are important for building up complete systems. For connection of different functions like micro pumps, valves, mixers, etc., the main issue is to have the least dead volume and a good seal between the modules to prevent contamination and the loss of pressure.

Currently available methods of interconnecting microfluidic systems are manifold and fit for many different applications and materials.

2.1.3.1 Interlocking Structures

Interlocking structures are used for interconnecting individual microfluidic components or modules. The shapes of these interlocking structures can vary and there are different solutions for sealing the junction.

C. Gonzáles et al. reported a silicon based system using fins for interlocking and Silicone O-rings for sealing [45] as shown in Figure 2-21.

Figure 2-21. Interlocking of parts with interposed O-ring [45]

The system was tested up to 140kPa when the glued connections of tubing failed.
According to Gonzáles the parts could be separated and reassembled several times.

B.L. Gray et al. did some similar work but varied the shape of the interlocking structures [46]. They did not only use fins but also notched cylinder – hole structures (see Figure 2-22). The junction of the microfluidic modules was sealed using gasketing material (wax) being coated onto one component.

Figure 2-22. Interconnecting microfluidic components: (a) fins and (b) cylinder - hole structures [46]

The system with fins was tested with a pressure up to 100kPa, the cylinder – hole interconnect structures withstood a pressure of about 70kPa.

Gray reported that although the interlocking structures were damaged often during disassembling, the systems showed no leakage for about three exchanges. Due to being less brittle than silicon Gray et al. also fabricated some plastic interconnects, suggesting that these would perform better than the Silicon interconnects and seal without any gasketing material. They have not reported any trials so far.

The method of using interlocking structures allows a quick exchange of microfluidic modules and components and there is no adhesive used that might block the channels.

At the moment the materials being used are limited to Silicon and glass. There is presently no example for systems based on polymers, and due to the area requirement of the interlock, it is only feasible for modules, not for single interconnections to the macro world.

2.1.3.2 Modular Approaches

Modular assembly is desirable for integrated systems like micro total analysis systems (µTAS) or Lab-on-a-Chip (LOC) as it saves space (planar solution) and time (all connections are made in one step). Apart from interlocking structures many other approaches have been taken to interconnect microfluidic components and modules.

T.S.J. Lammerink et al. built a mixed circuit board (MCB) to which modules such as sensors, mixers, pumps etc. could be connected [47]. The modules were bonded to the board as shown in Figure 2-23, whereas the bonding technique (anodic bonding, glue, soldering etc.) depended on the material of the module. The mixed circuit board contained electric connections to which the modules could be connected.

Figure 2-23. (a) Flow sensor on top of a Silicon - glass MCB, (b) MCB made of plastics [47]

This concept can be used for many different materials and provides an easy and quick solution for interconnecting different microfluidic components.
The main drawback of this method is that it is a difficult task to remove the bonded module without destroying the mixed circuit board.

A planar solution to connect separate fluidic chips was presented by P.F. Man et al. [48]. They manufactured flexible plastic connectors with large access holes on both ends that contained one or more capillaries (Figure 2-24).

Figure 2-24. Multi-channel connector bonded onto two microfluidic chips [48]

The connectors were bonded onto the microfluidic chips using epoxy and the systems were tested with a pressure up to 200kPa without showing leakage. Using flat connectors is a good way to save space and due to being flexible the step height between chip modules could be overcome.

Although it is possible to manufacture the connectors in batch processes it is a time consuming operation (see Figure 2-25).

Figure 2-25. Fabrication of microfluidic connector [48]

T. Liu et al. proposed a similar connector but it should be made of three plastic layers [49] as shown in Figure 2-26. At the time of writing this connector has not been manufactured, but it would be feasible for mass production as the layers are easy to fabricate.

Figure 2-26. Multichannel connector [49]

A totally different approach is to connect different modules and seal the microfluidic channels in one step, as E. Igata et al. reported [50]. In this case each module consists of a substrate with open channels / trenches, possibly containing functional parts such as a micro mixer. During bonding small parts of each substrate's micro channels are overlapping, creating the junction. Substrate 1 now seals the channels of Substrate 2 and vice versa (see Figure 2-27).

Figure 2-27. Schematic diagram of the interconnecting principle and photo of the microfluidic modules [50]

The modules were bonded in 15min using a UV crosslinkable polymer adhesive and could be disassembled in 5min by the use of a dichloromethane bath.

This method shows different advantages. It can be used for many materials and microfluidic components, different bonding techniques can be adopted, and the system can be disassembled easily without damaging the modules. For small microfluidic systems or for more than three layers the alignment might be critical.

A solution for stacks of interchangeable modules was proposed by T. Hasegawa and K. Ikuta [51]. They contained the modules in a holder unit using Silicone rubber films as intermediate layers. To seal the joints a pressure was applied (spring) as shown in Figure 2-28.

Figure 2-28. Stack of microfluidic modules [51]

P.C. Galambos and G.L. Benavides came up with a system using two scales of packaging [52]: A microfluidic chip is put into an Electro-Microfluidic Dual Inline Package (EMDIP) which could be manufactured as a moulded plastic part. The fluidic connections are realized by holes in the EMDIP coinciding with extended openings of the microfluidic chip; potential electrical connections are made by bonding (wire bonding, flip-chip bonding etc.). Then the EMDIP is plugged into a Fluidic Printed Wiring Board (FPWB), which contains sockets for the leads and fluid ports of the EMDIP (Figure 2-29).

Figure 2-29. Electro-Microfluidic packaging architecture [52]

The idea of Galambos and Benavides has not been realized yet, but it seems to be a good idea to use standardised parts in the design of microfluidic-electrical connectors.

All methods mentioned in this section so far are for the use of interconnecting microfluidic components / modules, only. They are not applicable for connecting the microfluidic system to the outer world - on the contrary they need a world-to-chip interface themselves.

C.K. Fredrickson and Z.H. Fan made an overview of macro-to-micro interfaces of microfluidic devices [53]. In their report they showed a modular solution by de Mello et al. which contains interconnections to the outer world. This concept is included to illustrate how complex modular solutions can be (see Figure 2-30).

Figure 2-30. Exploded view of the interconnect parts [53]

To quote from Fredrickson and Fan's report:
"Two halves (parts 4 and 5) are brought together to form a main body using rods and screws (parts 3 and 6). Capillaries (part 1) are passed through the connectors (part 2), the sealing membrane (part 7), three portholes of the chip (part 8), and protrude from the bottom surface of the main body. The spacer (part 9), the glass back-plate (part 10), and the base with the observation window (part 11) are assembled together with the main body using plastic screws (part 12), while pushing the capillaries back a little to have the right depth relative to the chip."

2.1.3.3 Clamps / Frames

Another class of solutions for connecting the microfluidic chip to the outer world is to use clamps or frames that fix the chip while pressing interconnecting tubes onto the openings of the microfluidic system.

A.A.S. Bhagat et al. [54] built a simple frame to contain a microfluidic chip. Port clamps with openings for the tubing were fixed with Nylon screws using O-rings to form compression seals as shown in Figure 2-31.

Figure 2-31. Schematic illustration of the microfluidic interconnect concept [54]

According to Bhagat, the system could withstand pressures of more than 1.5MPa at temperatures between 20 and 80℃.

Z. Yang and R. Maeda reported a similar system but with more interconnection options [55]. They used a socket with 28 pins integrated for the connection of electric signals and power (see Figure 2-32). The fluid connectors in the hinged lid were equipped with built-in valves to control the flow rates.

Figure 2-32. Schematic drawing of the cross-section and photo of the socket [55]

This pressure limit of this system was 0.2MPa and the current was limited to 1A.

Both systems allow easy and quick mounting and dismounting of microfluidic chips. No adhesive that might block the channels is used and it is compatible with every material. The main disadvantage is the size of the frame. It was designed for single chip use, not for integrated applications. Manufacturing the frame, especially the one from Yang and Maeda, takes time, so it is no solution for the bottleneck problem in mass production either.

2.1.3.4 Adhesive

A very common way of connecting a microfluidic chip to the outer world is to put capillaries into the opening of the chip and fix it with adhesive. To get non-permanent interconnections it is also possible to glue a Teflon tube, instead, and use it as ferrule for the capillaries as shown in Figure 2-33.

Figure 2-33. Teflon tubes glued onto microfluidic chip [56]

J.H. Tsai and L. Lin improved this method by using a polymer sealant before applying the adhesive [57] as shown in Figure 2-34. This prevented adhesive blocking the microfluidic channels – a major drawback of this interconnecting technique.

Figure 2-34. Demonstration of the concept: (a) discrete processing and (b) integrated processing [57]

Tsai and Lin reported the maximum pressure to be at 190kPa. The pull-out test proved the connection could withstand a pulling force of 2N.

A method with minimal dead-volume was presented by C.H. Chiou and G.B. Lee [56]. A metal wire was inserted into a capillary and both were brought into position at the microfluidic chip. PDMS was moulded between capillary/wire and micro channel. After curing the mould the wire was pulled out and exchanged with silica based capillary to connect the system to the outer world (see Figure 2-35).

Figure 2-35. Schematic of the PDMS casting technique [56]

To form a parabolic shape inside the channel, a pulling force was applied to the wire during curing of the PDMS. The maximum leakage pressure of the microfluidic system was tested with 565kPa but the capillary – PDMS interface was tested up to 1MPa without showing leakage. That suggests that the connector might withstand high pressures if the connection PDMS – microfluidic chip is enhanced. Depending on the contact area between capillaries and connector the maximum pull-out force was about 13N.
The major drawback of this reusable method is the relatively large moulding area. The possible connection density is very poor.

Using adhesive is an easy and rapid method for connecting microfluidic systems to the outer world but the drawbacks of this method are obvious. The glue needs a certain sticking area so the connection density is poor (low pitch). Also the adhesive might block the channels or change the wall properties of the microfluidic system. Using sealants as reported above is a possible solution to that problem but it means additional steps in the process flow and might cause dead volumes.

2.1.3.5 Couplers

Couplers are a widely used method to connect microfluidic systems to the outer world. They can either be designed directly on the top layer of the microfluidic chip or be manufactured separately and bonded onto the chip afterwards. The shape and the materials being used can also vary, depending on the application and the requirements to the interface. The possibilities of fixing microfluidic tubes/capillaries in these ports are manifold – some attachments are permanent, others are easy to remove.

S. Li and S. Chen presented a through-hole type and L-type PDMS interconnector, which could be bonded onto glass and PDMS microfluidic devices [58]. The bond was made with oxygen reactive ion etching (RIE) and UV curable epoxy - the latter could also be broken to detach the connector. Glass and plastic tubing could easily be attached by putting it into the holes of the connector (Figure 2-36).

Figure 2-36. Schematic of the PDMS interconnect: (a) through-hole type and (b) L-type [58]

This method showed low dead volume and had a maximum leakage pressure of 510kPa. The maximum pull-out force of the tubing was about 800mN.

To enhance maximum leakage pressure and pull-out force, both PDMS interconnect and tubing could be reinforced with epoxy as shown in Figure 2-37. If the tubing was fixed with epoxy the interconnection was non-reusable.

Figure 2-37. Schematic for epoxy glued PDMS interconnect: (a) reusable and (b) non-reusable [58]

Now the maximum leakage pressure was found to be 683kPa and the pull-out force of the glued tubing was 2N.

E. Meng et al. designed several couplers for Silicon based microfluidic applications [59]. They were fabricated using bulk micromachining techniques, moulding, or deep reactive ion etching (DRIE) and were designed with a certain shape or with a collar to fit into openings in the microfluidic chip (see Figure 2-38).

Figure 2-38. (a) Bulk, (b) moulded, and (c) DRIE couplers with capillarie tubing [59]

Since attaching every coupler to fluidic ports individually was very time-consuming a batch process was developed. Thermoplastic adhesive was spray coated onto the wafer before the couplers were separated and aligned to the ports. Then the microfluidic chip was heated up and cooled down to form the bond (Figure 2-39).

Figure 2-39. Process flow for the thermoplastic spray-coating technique [59]

The tubing was connected to the couplers using adhesive or by cryogenic insertion. In cryogenic insertion the end of the tubing is put into liquid Nitrogen to make it shrink. The shrunk part is led into the coupler and while warming up to room temperature it regains its old diameter and creates a press fitting (see Figure 2-40).

Figure 2-40. Cryogenic insertion technique [59]

Bulk and DRIE couplers were able to withstand a pressure of up to 8.9MPa, which was the limitation of Meng's experimental apparatus. The connection between moulded couplers and capillaries failed at a pressure of 6.2MPa.

B.L. Gray et al. came up with two different approaches to connect microfluidic systems to the macroscopic world using couplers [60]. In the first approach the coupler was manufactured directly in the top layer of the microfluidic system using deep reactive ion etching (DRIE). In essence it was a hole with a stop position containing the tubing. The tubing was then fixed with adhesive.

To prevent the adhesive from blocking the microfluidic channels another design of the coupler with a sleeve was used, as shown in Figure 2-41.

Figure 2-41. Schematic view of the couplers and SEM pictures of the coupler with sleeve [60]

The interconnection was tested with a pressure of 3.5MPa without showing any leakage. The limitation of 3.5MPa was determined by the test setup.

The second idea was to design a plastic coupler, which was fixed to the microfluidic chip with heat-staked pegs. The opening of the coupler was smaller than the outer diameter of the capillary creating a press fitting. The tubing could be attached and removed easily. G.T.A. Kovacs from Gray's group patented a method to manufacture these fluidic couplers [61] shown in Figure 2-42.

Figure 2-42. Schematic view and picture of the press-fit type Silicon / plastic coupler [60]

The junction was not leak proof so a Silicone gasket, cut from a 500µm thick sheet, had to be introduced between plastic and Silicon. The system was tested with a pressure of up to 414kPa and the maximum pull-out force of the capillaries was ranged from 1 to 2N. Another method of sealing the joint is to use a compliant seal inside the press fitting, as did C.R. Friedrich et al. [62].

E.S. Lee et al. drilled an hourglass shaped hole into a glass wafer and used it as a coupler [63]. Two cones were drilled into the layer, one on each side, using electro-chemical discharge machining (ECDM). Tubing with a diameter slightly larger than the waist of the holes was put into them forming a reusable press fitting (see Figure 2-43).

Figure 2-43. Hourglass fabrication process [63]

Using no adhesive to fix the capillaries the working pressure was limited. Maximum leakage pressure was about 103kPa.

Another idea is to integrate micromachined rubber O-rings in a Silicon microfluidic system, as T.J. Yao et al. did [64; 65]. Silicone rubber is squeezed into trenches, which are made by using deep reactive ion etching (DRIE). For better adhesion the trenches are covered with Silicon Nitride and, after etching the wafer from the backside, the O-ring is ready for use (see Figure 2-44).

Figure 2-44. Fabrication process for O-ring couplers [64]

This solution is space-saving and provides the possibility of quick attachment and detachment of tubing. Most of the O-rings showed no damage in a repetition test (>200 times) and, depending on the inner diameter of the tubing (all tested capillaries had an outer diameter of 500µm), the system could withstand pressures of about 550kPa. The maximum pull-out force was tested with more than 300mN.

A. Puntambekar and C.H. Ahn designed couplers with cavities in the top layer of a microfluidic system [66]. The system was heated up and tubing with an insert was put into the couplers, melting and filling the cavities. Another capillary

was then put into that tubing interconnecting the chip to the macroscopic world as shown in Figure 2-45.

Figure 2-45. Schematic diagram of serial interconnecting technique [66]

According to Puntambekar and Ahn the system could theoretically withstand a pressure of 2.6MPa (pull-out force of about 15N) but it was tested only with 207kPa.

A parallel connection technique which also can be used for polymer based systems was presented as well. The tubing was inserted in the top layer before the layers were bonded (see Figure 2-46).

Figure 2-46. Schematic diagram of parallel interconnecting technique [66]

The average pull-out force of about 39N led to a theoretical maximum leakage pressure of 6.6MPa. Again the system only was tested 207kPa.

A similar interconnection was used by A.V. Pattekar and M.V. Kothare [67] as shown in Figure 2-47. They placed a Silicon based microfluidic system on a hot plate and put a capillary into the opening of the upper layer. The tip of the tubing

was melted by holding it onto the hot bottom layer and then it was pulled back until the melted end sealed the top layer's opening. High temperature epoxy was then used to fix the capillary.

Figure 2-47. Capillary insertion and deformation / bonding [67]

The system was able to withstand 2.17MPa, the maximum pressure of the test setup. The maximum pull-out force of the interconnection was about 21.5N.

As the interconnect showed damages due to handling it was reinforced with another Teflon capillary working as sleeve (see Figure 2-48).

Figure 2-48. Reinforced interconnect [67]

This procedure prevented the tubing from getting damaged and increased the maximum pull-out force to more than 40N.

V. Saarela et al. manufactured a coupler by casting PDMS onto an etched Silicon mould [68] as shown in Figure 2-49. The Silicon mould was placed in a Petri dish and dummy capillaries were placed to form channels in the coupler. Then the PDMS was poured into the dish to a thickness of a few mm and the setup was put on a 70℃ hot plate for curing.

Figure 2-49. PDMS coupler casting setup [68]

After curing the PDMS was separated from the Silicon mould and the dummy capillaries were removed.

The coupler now was aligned to a microfluidic chip with matching surface relief and capillaries were aligned in the holes. The interconnection was effective but support with a jig allowed it to withstand higher pressures (see Figure 2-50).

Figure 2-50. (a) Coupler usage and (b) coupler reinforced with jig [68]

The normal setup was able to withstand pressures of up to 21kPa, if it was compressed by a jig the maximum leakage pressure was about 220kPa.
The couplers were reusable, but according to the authors only as long as they remained clean and did not suffer mechanical damage.

A fast interconnection method for polymer based microfluidic systems was presented by A.M. Christensen et al. [69]. A modified needle with a steep tip was used to core a PDMS layer. Unmodified needles then were pushed into the holes forming a compression seal (see Figure 2-51).

Figure 2-51. Schematic of the interconnect fabrication and picture of a realised interconnection [69]

Several setups of microfluidic systems were tested (PDMS bond, O_2 plasma bond, additional clamping) to determine the maximum leakage pressure of the interconnection rather than the bond strength. If the bond did not fail the coupling withstood a pressure of 700kPa, which was the limit of the pressure gauge.

This rapid and reusable interconnecting technique has the drawback of a low connection density. The fabrication process itself might be enhanced by not hand coring the holes as the authors did but to connect the tubing to the needles a certain area is still needed as shown in Figure 2-51.

T. Pan et al. used heat shrink tubing to connect micro tubes to Silicon based fluidic systems [70]. First a heat shrink tube sleeve was put onto the fluidic port (Silicon flange). The system was placed on a hot plate to make the tube shrink around the flange. After cooling down a capillary was put into the sleeve. Then the complete heat shrink tube was made to shrink by the use of a heat gun sealing the junction capillary – silicon flange (Figure 2-52).

Figure 2-52. Interconnecting using a heat shrink tubing [70]

The system showed no leakage at the maximum test pressure of 200kPa. Due to application of heat this easy to use method is not feasible for polymer-based systems.

The designs for microfluidic couplers are as multi-faceted as the applications of microfluidic systems. Many interesting designs are possible for Silicon and some for plastic systems, showing different values in maximum pressure, reliability, and number of manufacturing steps.

Most of the solutions presented in this section are either not easy to connect outside a lab, or need many process steps during manufacturing. It would be desirable to have a system-to-world interconnect solution for plastic microfluidics that can also be rapidly manufactured.

2.1.3.6 Threaded Interconnections

A special case of couplers are threaded interconnections. These couplers are designed with a thread and can be screwed into the fluidic ports. An attribute that makes them easy to remove - while being able to provide a good connection to the microfluidic chip.

E.S. Lee et al. drilled threaded holes into a glass substrate and used them to mould plastic screws [63]. In the first step cones were machined using electro-chemical discharge machining (ECDM). The glass slide was flipped over and the cones were opened out to cylinders. After imprinting the threads, the screws could be moulded (see Figure 2-53).

Figure 2-53. Threaded interconnect fabrication process [63]

The screws were now connected to capillaries and were ready to be used as couplers as shown in Figure 2-54. The glass slide with the threaded holes was used as top layer of the microfluidic system and a Silicone gasket was used between the screws and the glass layer to enhance sealing.

Figure 2-54. Microfluidic device with threaded interconnect [63]

All connections were tested satisfactorily at a pressure up to 206kPa, which was the limitation of the test setup.

In their patent specification of the Electro-Microfluidic Dual Inline Package (see Section *2.1.3.2 Modular Approaches*) G.L. Benavides et al. also came up with an idea for threaded couplers [71]. An O-ring seal is pressed onto a microfluidic chip being held in place by a hollow screw. The screw is threaded into an aluminium plate that is bonded to the chip (Figure 2-55).

Figure 2-55. Hollow screw used as coupler [71]

The screw worked as a coupler and capillaries could be put into it and fixed with epoxy.

To connect microfluidic chips to the outer world the capillaries don't have to be connected to the chip only, but also between each other or to fluidic ports of wells or other macroscopic parts. Therefore Upchurch Scientific® offers different solutions [72]. Many of them also use threaded connectors and receiving ports as shown in Figure 2-56.

Figure 2-56. Upchurch threaded interconnect with port [72]

Although threaded interconnections provide an easy and reusable coupling there are some drawbacks of this method. Time-consuming process steps are needed to manufacture the couplers and sometimes there is even an additional layer required to hold the screws. There are no practicable solutions for polymer based systems, yet, and the size of the connectors limits the connection density. Low density of connections prevents further miniaturisation of the microfluidic chips.

2.1.3.7 Overmoulding

D.P. Webb et al. realised the packaging of microfluidic systems by overmoulding them [73; 74]. Injection moulding was used to embed the microfluidic device in plastic and the usage of pins during the mould process provided access to the fluidic channels (see Figure 2-57).

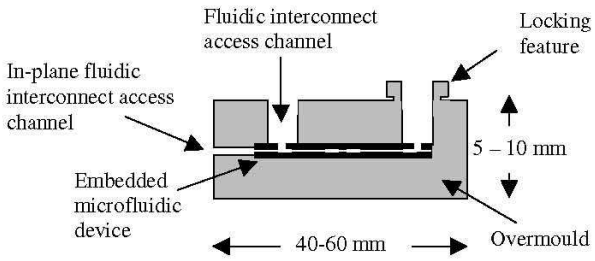

Figure 2-57. Cross-section view of the overmoulded device [73]

Depending on the design of the cast the microfluidic device could be sealed and equipped with features like couplers or locking structures (see Section *2.1.3 Interconnecting of Microfluidic Systems*) for connecting the system to the outer world in one step. The seal was tested with a pressure of 690kPa without showing leakage.

2.2 Induction Heating

The discovery of electromagnetic induction by Michael Faraday in 1831 led to the development of electric motors, generators, transformers and wireless communications devices. All the time heat loss was a major factor reducing the efficiency of these systems and researchers sought to minimize it. In the early 20th century the heat loss was utilized for the first time. This utilization was referred to as induction heating and nowadays it is used for many applications, such as melting, hardening, and welding of metals, and many more. The main benefits over other heating methods are the selectivity of the heated area, the fast response time, and a good efficiency.

An induction heating unit consists of a power generator, a tank circuit and a water cooling system as shown in Figure 2-58.

Figure 2-58. Induction Heating Unit [75]

The tank circuit consists of four or more capacitors in a housing and a coil. The housing of the capacitors provides power and cooling connections for the coil. During calibration the power generator checks the resonance frequency of this circuit and generates an alternating current of the same frequency. Then the work piece is put into the magnetic field of the coil to get heated.

2.2.1 Applications

As induction heating has long history there are many applications. Especially in the steel industry where it is commonly used. Induction heating is employed for forging, extrusion, welding, and brazing, melting of metals, hardening of steel, and annealing [76; 77; 78]. It can also be used for processing small parts, for instance annealing copper crimp connectors or brazing diamond tips on cutting tools as shown in Figure 2-59.

Figure 2-59. Diamond tips are brazed to steel shanks for high-speed machine tools [75]

Induction heating is used for rapid temperature variations during micro injection moulding to achieve structures with high aspect ratio [79]. It can also be used for heat staking as shown in Figure 2-60.

Figure 2-60. Inductive heat staking [80]

A metal thread is heated up inductively and inserted into a plastic part.

Induction heating can be used for fixing caps on cans with solder preforms [75] or for joining thermoplastics [81].

Cap sealing as it is done for milk and oil cans etc. is a very interesting application as well [82]. Polymer laminated aluminium foil is pressed onto the neck of a plastic container and heated inductively by flat helix coils above the setup. The polymer melts and bonds the foil to the container.

The effects of induction heating are not only adopted in industry but can also be found in a kitchen. Inductive cookers are common as they are more convenient and safer than electric or gas cookers [83]. Single devices like rice cookers also use induction heating systems [84].

A more experimental application is use with hinged microstructures [85]. Y.W. Yi and C. Liu used a magnetic field to actuate these structures as shown in Figure 2-61.

Figure 2-61. SEM picture and schematic view of hinged microstructures [85]

H.A. Yang et al. optimised this method by using the heating effects of the applied magnetic field [86]. The lifted microstructure was fixed by an inductively melted solder bump (see Figure 2-62).

Figure 2-62. Concept of lifting and soldering microstructures [86]

This concept could be used for the design of complex MEMS or micro mirror arrays etc.

If very high frequencies are used Silicon can be heated directly. K. Thompson et al. used a 13.57MHz generator for direct Si-Si boding [87]. During the process the wafers were heated to temperatures around 1000°C.

High frequency induction heating is adopted for melting silicon and controlling temperature in the melt during crystal growing.

2.2.2 Physical Principles

The fundamental theory of induction heating is similar to that of a transformer. The work coil used in induction heating is equivalent to the first coil, the load functions as a short-wired second coil.

2.2.2.1 Electromagnetic Induction

The premise of induction is that a change in magnetic flux induces a current in a circuit or conductor. The change in magnetic flux can be achieved by either altering the magnetic field or moving the conductor in the magnetic field [88]. The principle is expressed by Faraday's law:

$$E = -N\frac{d\phi}{dt} \qquad (2\text{-}1)$$

Where

E:	Induced voltage	[V]
N:	Windings of the coil	unitless
Φ:	Magnetic flux through a single winding	[Vs]
t:	Time	[s]

The minus sign means that the induced voltage E will cause a current to flow that generates a magnetic field counteracting the change in the inducing field (Lenz's Law).

Figure 2-63. Induction law of Faraday [76]

In Figure 2-63 the alternating magnetic field is generated by a coil connected to an ac power supply unit. The alternating current I_1 induces a voltage E in the secondary coil, which only has a single winding. The induced voltage would be

$$E = -\frac{d\phi}{dt} \qquad (2\text{-}2)$$

In Figure 2-63b the secondary coil is short-circuited so an alternating current I_K can flow in opposite direction of I_1 generating a magnetic field counteracting the magnetic field generated by the primary coil.

If a solid conductive load is placed inside the alternating magnetic field, eddy currents will be induced in that load (see Figure 2-64). The eddy currents heat the load according to the Joule effect.

Figure 2-64. Induction of eddy currents [76]

2.2.2.2 The Joule Effect

Every conductor offers resistance to a flow of a current that causes loss of power [89]. The loss of power is converted to heat energy and is described in Joule's law:

$$P = R \cdot I^2 \qquad (2\text{-}3)$$

Where

P:	Power dissipated in the conductor	[W]
R:	Resistance of the conductor	[Ω]
I:	Current induced in the conductor	[A]

This effect is also referred to as the Joule effect. For constant currents higher resistivity leads to higher heating power. However, the amount of current induced in the workpiece will also vary with resistivity, especially for a resistive load. Therefore both effects must be considered together to determine the optimum resistivity for greatest heating power. This aspect will be discussed later in more detail.

Table 2-1 presents some materials with their resistivity.

Table 2-1. Resistivity

	Resistivity [Ω·m]	Resistivity [Ω·mm^2/m]
Aluminium	2.64e-08	0.0264
Lead	2.20e-07	0.22
Iron	1e-07 to 1.5e-07	0.1 to 0.15
Gold	2.44e-08	0.0244
Graphite	8.00e-06	8
Carbon	3.50e-05	35
Copper	1.78e-08	0.0178
Nichrome (Nickel-Chromate alloy)	1.50e-06	1.5
Platinum	1.10e-07	0.11
Silver	1.59e-08	0.0159
Silicon	2,300	2,300,000,000
Steel	1e-07 to 2e-7	0.1 to 0.2
Tungsten	5.60e-08	0.056

2.2.2.3 Hysteresis Heating

For ferromagnetic materials in an alternating magnetic field a second heating effect occurs. The magnetic orientation of the domains of the susceptor aligns with and attempts to follow the rapidly varying field. The friction of this movement in the crystal plane heats up the metal and is referred to as hysteresis heating. If a ferromagnetic material is heated to its Curie temperature it becomes paramagnetic and hysteresis heating ceases.

2.2.2.4 The Skin - Effect

Alternating currents in a conductor generate a magnetic field. As the magnetic field changes as well, currents are induced counteracting their cause. This leads to an increase of currents on the conductor's outside and a decrease in its middle. This "skin-effect" is characterized by its penetration depth δ. The penetration depth is defined as the thickness of the layer, measured from the outside, in which 87% of the power is developed [76] (see Figure 2-65).

Figure 2-65. Penetration depth [76]

For an alternating current of frequency f the penetration depth is given by

$$\delta = \sqrt{\frac{2 \cdot \rho}{\mu \cdot \omega}} \qquad \text{(2-4) [90, p.310], with } \omega = 2\pi f$$

➔ $$\delta = \sqrt{\frac{\rho}{\pi \cdot \mu \cdot f}} \qquad \text{(2-5)}$$

Where

δ:	Penetration depth	[m]
ρ:	Resistivity	[Ωm]
μ:	Permeability	[Vs/(Am)]
f:	Frequency	[Hz]

Permeability μ is the product of the magnetic field constant μ_0 and the relative permeability μ_r of the conductor

$\mu = \mu_0 \cdot \mu_r$ (2-6) [91, p.441], with

$\mu_r = \frac{B}{B_0}$ (2-7)

Where

B: Magnetic flux density in the conductor [Vs/m^2]

B_0: Magnetic flux density in vacuum [Vs/m^2]

μ_r is less than 1 for diamagnetic materials, and slightly greater than 1 and many times greater than 1 for paramagnetic and ferromagnetic materials, respectively.

In appendix *A1 Penetration depth*, two graphs are enclosed showing penetration depth over frequency for different materials. The materials are Ni (μ_r = 600), steel (μ_r = 1000), Ni above Curie temperature (T_C = 360°C, μ_r = 1), steel above Curie temperature (T_C = 770°C, μ_r = 1), Cu (μ_r = 0.9999936), and Al (μ_r = 1.0000222).

2.2.3 Coil Design

The design of the coil is one of the most important aspects of induction heating. It defines how the magnetic flux is coupled into the work piece, where the hotspots are (if any), which areas are affected by induction heating, etc. Every design has a different inductivity. The coil and capacitors in the tank circuit form a resonant circuit in which an alternating current is driven at the resonant frequency by the power supply. The voltage output from the power supply is varied to attain a desired output power with a given coil/capacitors combination.

According to S. Zinn and S.L. Semiatin, coil design is generally based on experience and empirical data rather than simulations [92]. This view was confirmed by engineers at Hüttinger Elektronik during the work described in

Section *4.2 Experiments at Hüttinger Elektronik*. Some of the manifold varieties of coil designs used are shown in Figure 2-66.

Figure 2-66. Different coil designs [92]

The coils can be designed with single or multi turns, for single and multi places. In addition to these “standard” coils there are endless variations designed for special purposes as shown in Figure 2-67.

Figure 2-67. Coil modifications for localised heating [92]

Zinn and Semiatin determined some basic design considerations that should be followed to reach best efficiency. The distance between the windings should be kept as small as possible and the work piece should be as close as feasible to the coil to assure maximum energy transfer. As the magnetic centre of the inductor is not necessarily its geometric centre the work piece should be rotated to gain more homogeneous heat distribution. The coil must also be designed to prevent cancellation of the magnetic field. If two windings running in opposite

directions are too close to each other, each magnetic field can be cancelled by the other.

2.3 Implications for the Current Work

As shown in previous sections there are many different techniques used to seal microfluidic systems. Not all of them are applicable for polymer based systems and if they are, they are either slow or expensive, are often lab-based, or a complex assembly is needed. As these assembly processes form a bottleneck of mass production an alternative challenging the drawbacks of current techniques is needed. With an easy setup, a reproducibility of results, high selectivity and high throughput capability low frequency induction heating (LFIH) was found to possibly be such an alternative.

There are many parameters affecting the heating rate during induction heating. Application of high current in the work coil (high magnetic field strength) results in a high current in the work piece which leads to a higher power loss by heat generation. The design of the coil and its coupling to the load must be considered for achieving best results as well.

Very important factors are the material characteristics of the load. The load conductivity will have an effect on heating rate. Resistivity and permeability also affect the penetration depth. High permeability and conductivity lower the depth of penetration. The other factor controlling the skin-effect is the frequency of the alternating magnetic field. The higher the frequency the higher the current density on the outside of the load. To gain a more homogenous heat dissipation the penetration depth should be in the order of the workpiece’s thickness.

The following conditions can be identified for high heating rates in micro work pieces:

- High magnetic field strength should be used
- Distance between windings of the inductor coil should be as small as possible
- Distance between inductor and load should be as small as possible
- Penetration depth should be of the order of the workpiece's thickness

An analytical model describing the heating parameters and their interdependencies was missing in the literature about induction heating. As it is essential for understanding and optimising the heating rate of the susceptor, such a model had to be derived.

3 Methodology & Experimental Details

In order to identify whether thin susceptor films can be heated adequately at low frequencies and which equipment should be ordered for further experiments some initial trials had to be carried out. During these trials thin nickel foils, supported in air, were heated and temperatures were measured using a pyrometer. Also thin layers of nickel evaporated and electroplated or aluminium sputtered onto PMMA were tested to investigate the capabilities and limitations of induction heating equipment.

During the project it was essential to gain an understanding of how different parameters like heating time, working distance and output current affect the amount of generated heat. First the basic physical equations were identified and, depending on those equations, the functional dependence of heating rate on the parameters was hypothesised. Numeric models, simulating the current density generated in the workpiece by a single coil, and the resulting temperature change in the workpiece, were used to validate the hypotheses. Similarly validation experiments were undertaken. Steel and nickel foils supported in air were heated inductively and the temperature was measured using a thermal imager. It was found that the functional dependencies were mostly confirmed. However, there were some interdependencies between parameters, which meant variation of heating rate with some single parameters could not be determined (e.g. susceptor area, cross sectional area). Therefore it was considered necessary to derive an analytical model to take account of these interdependencies. This model was derived using the same basic equations and its predictions compared with the experimental data already obtained.

Then the effects of susceptor design were investigated. First the susceptor area was varied in a numeric model while keeping all other parameters constant and the corresponding temperature was simulated. A similar numerical model was used to determine the importance of permeability for heating of thin film susceptors.

In order to draw conclusions of how the susceptor shape affects the heating rate, different shapes with different sizes were etched out of thin nickel foil and mounted onto glass substrates. The nickel features were heated inductively and again the temperature was measured using a thermal imager.

Finally it was investigated which parameters might support or hinder the forming of bonds. Firstly, substrates are never perfectly flat so the effect of thermal barriers, i.e. small air gaps, between heat source and substrate was identified using numeric modelling. Secondly, to draw conclusions of how heating time and the amount of pressure applied during the bonding process affect the bond quality stacks of PMMA substrates with intermediate nickel susceptor were bonded. Pressure during heating was applied using non-conductive weights. The bond strength of the bonded stacks was measured using tensile strength tests. Size of bond area, melt zone and heat affected zone (HAZ) were measured on the broken specimens using light microscopy. Thirdly, pulsed heating was considered as alternative to continuous heating to reduce melt area while maintaining good bond strength. A similar setup as for the bond pressure experiments was used and again bond strength, bond area, melt zone and HAZ were measured for the bonded samples.

Finally the functional capability of the technique for bonding microfluidic devices was trialled with two test cases.

3.1 Experimental Techniques

The different physical resources and experimental techniques applied are described in the following sections.

3.1.1 Evaporation

In the evaporation coating method a carrier or basket containing the target material is heated up conductively. As temperature reaches the boiling point of the target material, the material melts and evaporates, coating every surface in the evaporation chamber.

3.1.2 Electroplating

Electroplating is used to deposit metals or alloys onto a wafer surface. The wafer surface must be conductive and is connected to the cathode. A Platinum anode is connected to the material that has to be deposited. Both are put into an electrolyte bath (Figure 3-1). On application of a current to the cathode the metallic cations are deposited. Depending on the current density and the formulation of the electrolyte bath the characteristics of the deposited layer (growth rate, hardness, stress, uniformity) may vary.

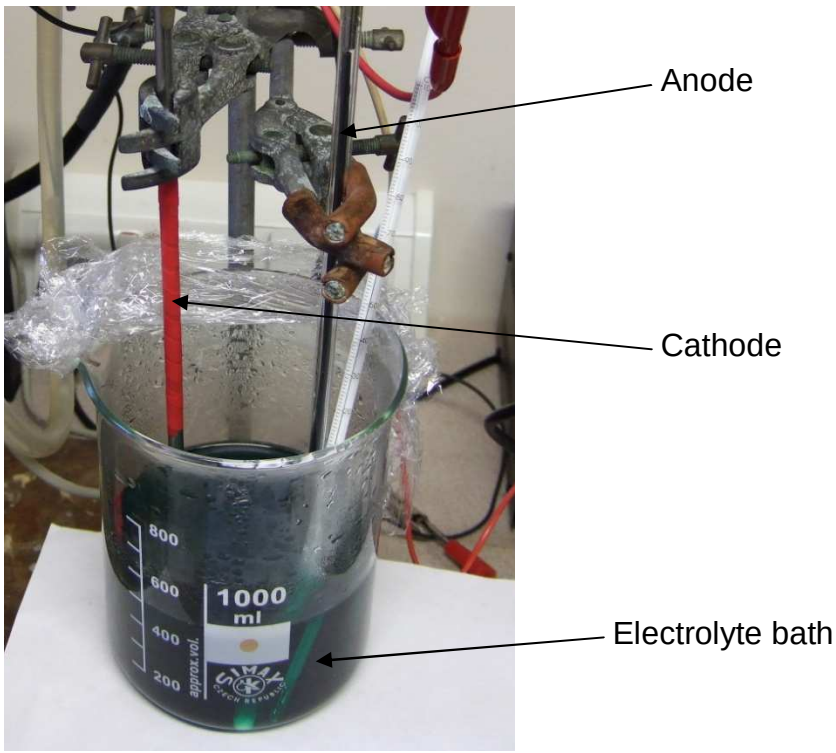

Figure 3-1. Electroplating setup

3.1.3 Sputtering

"During sputtering, the target (a disc of material to be deposited), at a high negative potential, is bombarded with positive argon ions […] created in a plasma […]. The target material is sputtered away mainly as neutral atoms by momentum transfer and ejected surface atoms are deposited (condensed) onto the substrate placed on the anode." [93, p.138]

The adhesion of sputtered layers is generally good because the target material hits the substrate with high energy, which causes a close connection between substrate and coated layer. Due to high temperatures generated during the process not every substrate can be coated.

3.1.4 Laser Machining

Short pulses of coherent light are focused on the surface of a workpiece. The workpiece absorbs the energy and heats up and the material around the laser spots evaporates. This technique can be used to create small channels in polymer substrates and to cut these substrates.

3.1.5 Shear Strength Test

To identify the strength of a bond each substrate is fixed in a clamp and pulled apart as shown in Figure 3-2:

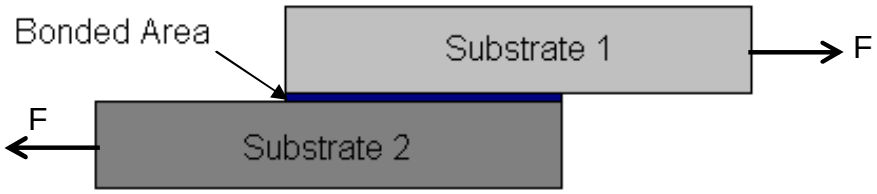

Figure 3-2. Tear strength test

The pulling force is measured during the process and the bond strength (or shearing resistance) can be calculated with

$$P = \frac{F}{S} \qquad (3\text{-}1)$$

Where

P:	Bond strength	[Pa]
F:	Maximum pulling force	[N]
S:	Bonding area	[m^2]

3.1.6 Micrographic Cross Sections

A cross section view helps to investigate the microstructure of bonded substrates. A cut is made through the area of interest and the workpiece is moulded in epoxy to increase stability and manageability. After curing the epoxy the cutting marks are polished away and the cross section can be investigated under a microscope.

3.1.7 Dry Film Lamination / Lithography

To be able to structure thin metal foils a combination of dry film lamination and lithography/etching can be used. First the foils are laminated with a dry photo resist film from both sides. Then the film is exposed through a mask and developed. Unexposed film and adjacent foil are etched and finally the structured foil can be released in an acetone bath.

3.2 Materials

To get the best results the materials used as susceptor and microfluidic platform have to be chosen carefully. The susceptor material should perform well when using low frequency induction heating while the substrate material should be commonly used in the field of microsystems / microfluidics.

3.2.1 Susceptor

Susceptor materials must be conductive to absorb the electromagnetic energy. The higher the conductivity the higher the eddy currents. As shown later in Section *5.3 Change of Resistivity*, susceptors with low resistivity and high relative permeability perform best. Another demand is how easy and at which

temperatures the material can be applied to the polymer platform. Table 3-1 shows resistivity and relative permeability of some materials:

Table 3-1. Susceptor properties

	Resistivity ρ [Ω·m]	Relative permeability μ_r unitless
Aluminium	26.4e-9	1.0000222
Nickel	69.9e-9	100-600
Copper	17.8e-9	0.9999936
Steel	1e-9 to 2e-9	1000

Aluminium is slightly paramagnetic and copper slightly diamagnetic. Their relative permeability is close to one and their resistivity is fair so these materials could be heated inductively at low power. As aluminium and copper can be coated onto plastic at low temperatures, and both materials are quite common in microsystems, they form a possible choice as susceptor.

Steel has low resistivity and very high relative permeability. It can be used to test the limitations of the induction heating technique but it is too complex to create thin layers of steel to work as susceptor for bonding plastic substrates.

Nickel with its high relative permeability is a very good susceptor although the conductivity is not best. As it is widely used in microsystems and can be coated and structured easily it will be the material used as susceptor mostly in this project. Nickel is harmful, so when designing a microfluidic chip not only the polymer layers must be sealed but the nickel should be sealed from the fluid as well.

3.2.1.1 Susceptor design

There are two main considerations for the susceptor design. A complete layer can be used as shown in Figure 3-3a or the susceptor can be structured forming thin metal tracks that follow the microfluidic channel on both sides (Figure 3-3b).

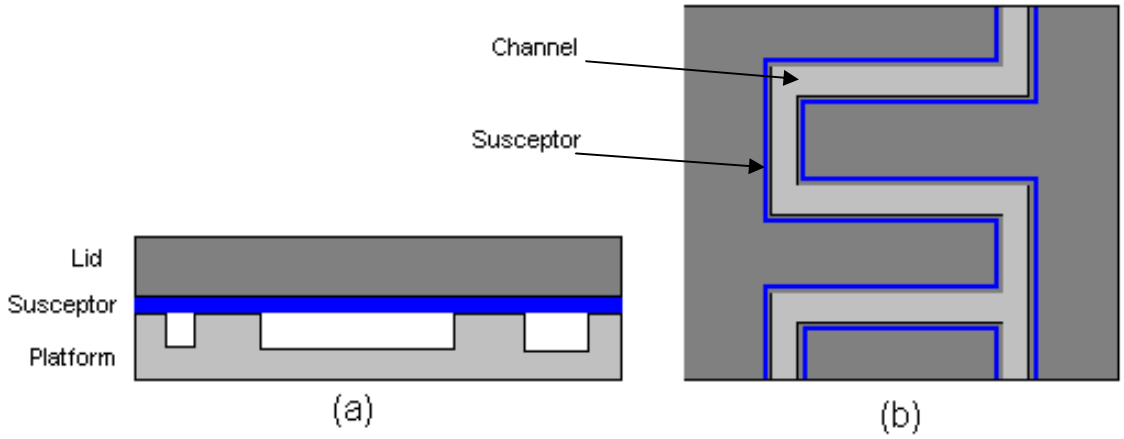

Figure 3-3. (a) Cross section view of whole layer and (b) Top view of structured susceptor

The whole layer approach is easy to realise. The susceptor material can be coated onto the lid or onto the platform before manufacturing the channels to provide transparency. Electroplating, electroless plating, sputtering, etc. are common techniques and are capable of plating nickel, aluminium and copper.
A major drawback of this approach is the generally poor bond adhesion between metals and plastics and the missing separation of susceptor and tested liquids/gases.

To create a structured susceptor there are different solutions. A mask can be used during plating or the whole layer can be structured afterwards using laser machining or etching techniques. Ink jet or screen-printing could be feasible techniques, as well as machining channels into the polymer and filling them with conductive ink or metal powder. During this project the susceptor was etched out of nickel foil and placed manually.

The advantages of structured susceptors are clear: Less material is introduced into the system and heat is only generated where it is needed. The bond will be created directly between the plastic substrates and the susceptor can be design in a way that it is enclosed during bonding.

For both approaches it has to be kept in mind that the susceptor design also affects the heat dissipation (see Section *6.1 Susceptor Design* for further information).

3.2.2 Microfluidic Platform

The material options for plastic microfluidic systems are manifold. Many different polymers like PMMA, PDMS, PA, PEEK, and so on are widely used. Some of them are transparent, others opaque; some have a high melting temperature, others a low. A common polymer with a low melting point that is cheap and easy to obtain should be used. To facilitate monitoring of the experiment and analysing the bonds it should be transparent to white light. As medical applications were identified as a major application for polymer based microfluidic systems the material should be benign to the fluids used in these applications.

The decision was made to use Polymethyl methacrylate (PMMA), which is not only commonly used for manufacturing microfluidic systems but also in a wide range of other applications. PMMA is soluble only in a few solvents (e.g. acetone) and many companies offer custom size pieces of industrial PMMA (e.g. Perspex®, Repsol Glass®).

3.2.2.1 Pre-Treatment

During electroplating the adhesion between evaporated seed layers and the polymer substrate turned out to be poor and the electroplated nickel peeled off. A different recipe for the electrolyte bath was used to reduce stress in the electroplated layer (see appendix *A4 Recipes for Electrolyte Bath*) and the PMMA was also pre-treated to enhance adhesion.

The PMMA substrate that was to be coated was held into the flame of a Bunsen burner for a few seconds. According to the Sabreen Group [94] this should create a polarity on the polymer surface and increase adhesion between the surface and coating material. The electroplated nickel layer no longer peeled off. However, as a different electrolyte bath formulation was used for these pre-treated substrates it is not clear whether the observed improvement in adhesion was due to the flame treatment, reduced stress in the nickel layer or, most probably, both.

Other techniques to increase adhesion can include activating the surface using plasma etching or roughening the surface to provide more mechanical adhesion. As PMMA contains water, which can contaminate the surface, pre-baking the substrates could also be considered. Those techniques were not tested during this project.

3.2.3 Preparation

To coat a substrate with susceptor material a thin layer (100-500nm) had to be evaporated first. This layer was used as seed layer for electroplating. Another technique to coat substrates was sputtering. No seed layer was needed, but due to the use of plastic substrates only materials with low melting points such as aluminium could be sputtered.

To create channels in the microfluidic platform laser machining was used. The channels were used as a microfluidic network or were filled with conductive ink / metal powder working as susceptor.

3.2.3.1 Evaporation

This method was used to create nickel seed layers for electroplating. A tungsten basket was connected to two electrical contacts and heated up conductively. As shown in Figure 3-4 the evaporating equipment features connections for four different baskets to prevent contamination if different target materials are used. The tungsten basket in this picture has already been used so it is covered with nickel.

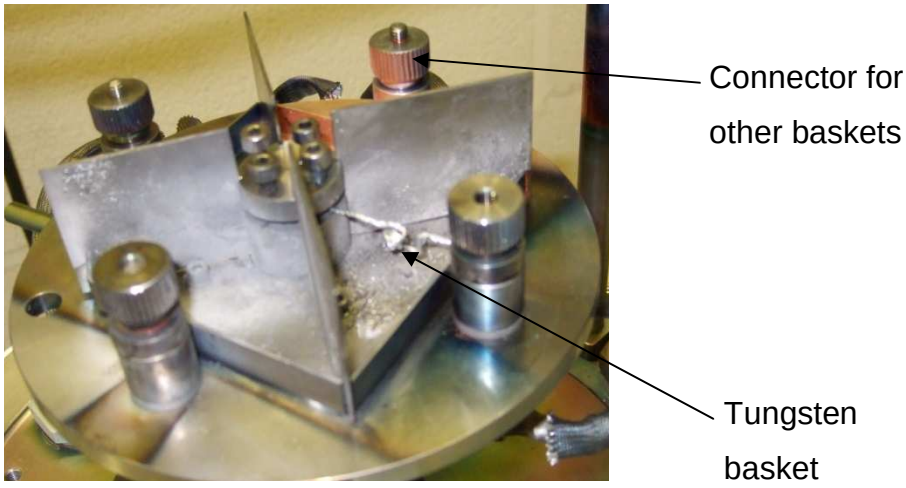

Figure 3-4. Installed Tungsten basket

Nickel wire then was put into the basket and three substrates at a time were placed above as shown in Figure 3-5.

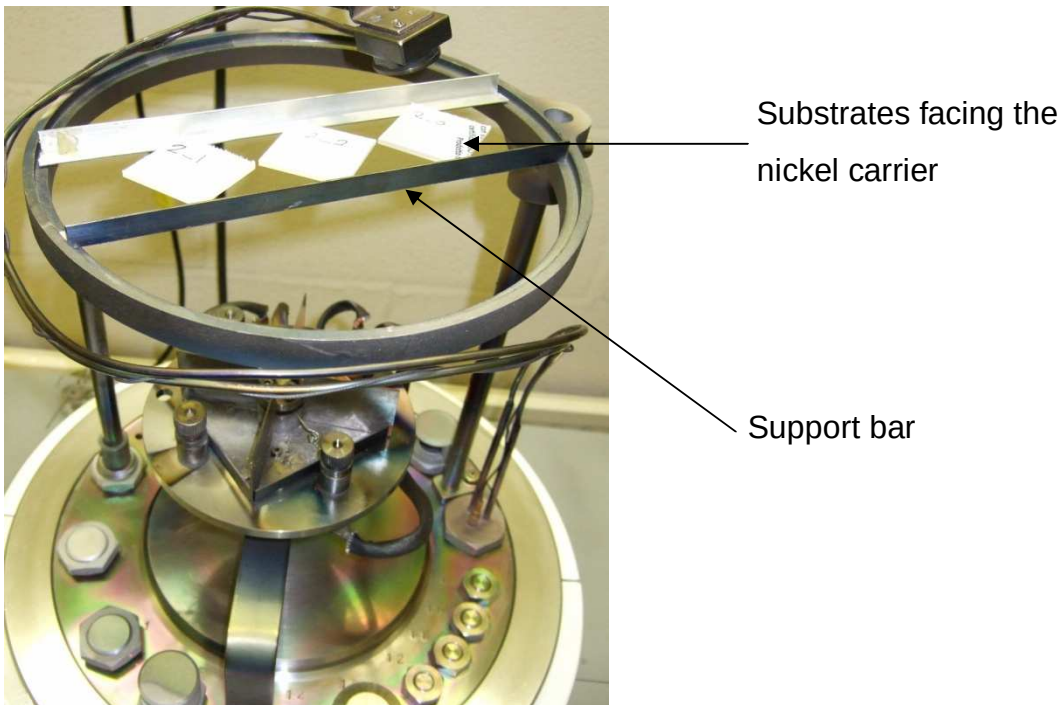

Figure 3-5. Substrates placed above Tungsten basket

A vacuum jar was put over the setup (see Figure 3-6) before a vacuum pressure of 10^{-5}mbar was applied.

Figure 3-6. Evaporation chamber with jar and protecting cylinder

At a current of 15 to 20A the basket was hot enough to evaporate the nickel wire. The evaporated layer (Figure 3-7) had a thickness of about 50 to 100nm, as estimated from previous experience. It can be seen that at the corners of the substrate that were lying on the support bar were not coated.

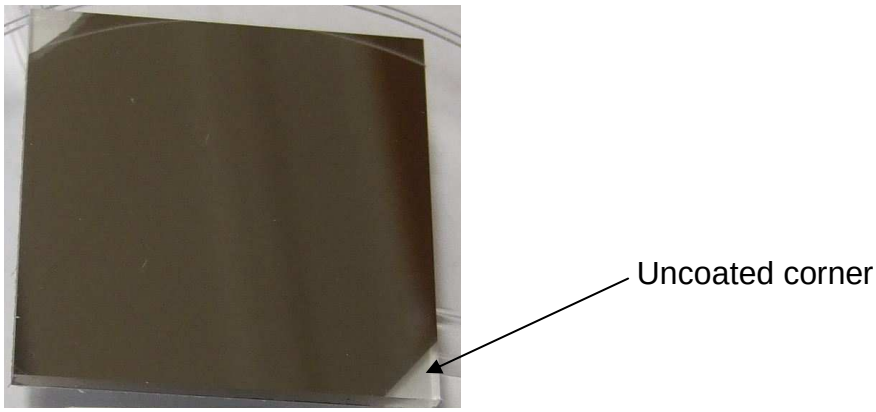

Figure 3-7. Coated PMMA substrate

3.2.3.2 Electroplating

The evaporated nickel seed layers were connected to the cathode and a 5µm thick layer was electroplated as shown in Figure 3-8.

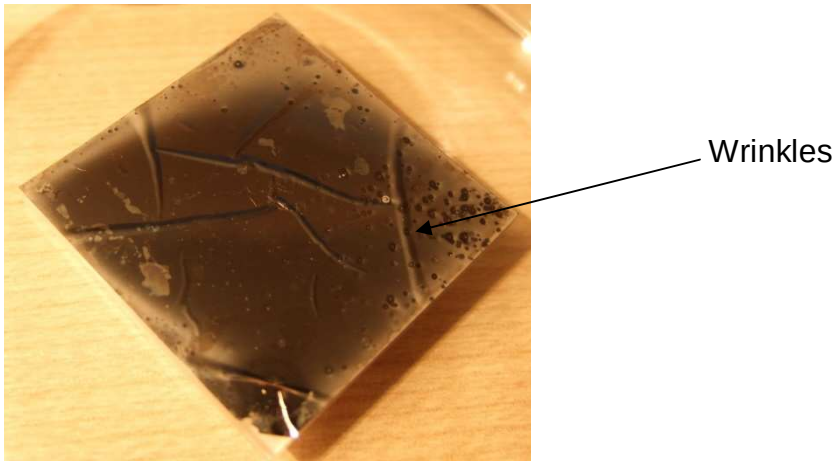

Figure 3-8. Electroplated nickel

The wrinkles are due to the different coefficient of thermal expansion (CTE) of nickel and PMMA. At 20℃ the CTE of nickel is 13 x 10^{-6}/K and 85 x 10^{-6}/K for PMMA. During electroplating the electrolyte bath had a temperature of 50℃. Assuming a constant CTE the shrinkage over 36mm of PMMA was about 92µm while the shrinkage of nickel only was 14µm.

To avoid the wrinkles the same electrolyte was used at room temperature, which led to smooth surfaces.

3.2.3.3 Sputtering

Sputtering was used to coat substrates with a 7µm thick aluminium layer. The work was carried by the Centre for Renewable Energy Systems Technology (CREST) in Loughborough.

3.2.3.4 Laser Machining

To cut the PMMA substrates or to machine channels into their surface a CO_2 Laser with 10W maximum power and a wavelength of 10.6µm was used. By varying power and velocity the size of the channels was controlled (see Figure 3-9).

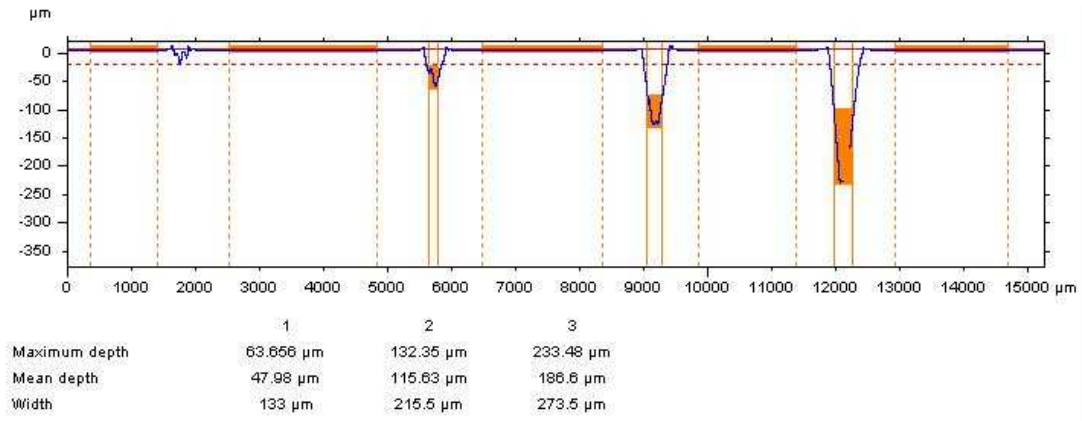

Figure 3-9. Laser machined channels with different width and depth, profiled with Talysurf CLI 2000

The quality of the channels was not an issue in this project as they were only used to prove the concept.

3.2.3.5 Lithography / Dry Film Lamination

In order to obtain structured susceptors a 7.5µm thick nickel foil was etched. The foil was first laminated at 115°C with a dry film photoresist supplied by Mega Electronics (part No 500-024). Exposure of the negative resist was done with 8s of UV light before it was developed with 1% potassium carbonate. To remove the undeveloped resist ferric chloride was used, which also etched the underlying nickel foil. To remove the remaining resist the parts were put in an acetone bath.

3.3 Equipment

To be able to carry out experiments at Loughborough University special equipment had to be organised. An induction heater was needed and a special workbench had to be designed as well. Also some equipment had to be organised for non-contact measurements of the generated heat.

3.3.1 Induction Heater

According to the requirements identified during experiments in Freiburg (see Section *4.2 Experiments at Hüttinger Elektronik*) an invitation to tender was published. The decision was made to purchase the AXIO 10/450 from Hüttinger Elektronik. Figure 3-10 shows the generator, which is controlled by software running on a laptop.

Figure 3-10. AXIO 10/450 Generator

The AXIO 10/450 has a maximum output power of 10kW and a nominal maximum frequency of 450kHz which can be increased to 900kHz if the distance between generator and tank circuit is less than 1.8m.

The tank circuit consists of a set of four capacitors connected to an inductor coil to form a resonant circuit as shown in Figure 3-11. The capacitors are arranged in a parallel circuit of two series connections, the latter consisting of two capacitors:

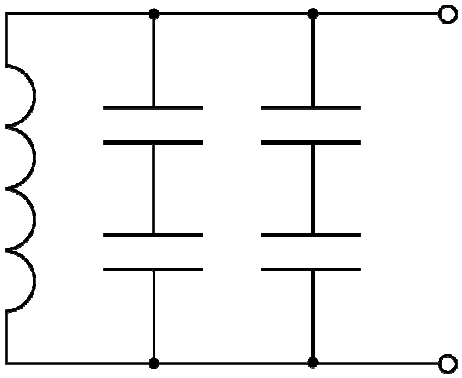

Figure 3-11. Circuit diagram of tank circuit

This way the main capacitance can be changed over a wide range with just a few different capacitors. Only one set of capacitors with a capacitance of 0.66 µF each was ordered. The inductor was a pancake shaped coil with five windings as shown in Figure 3-12.

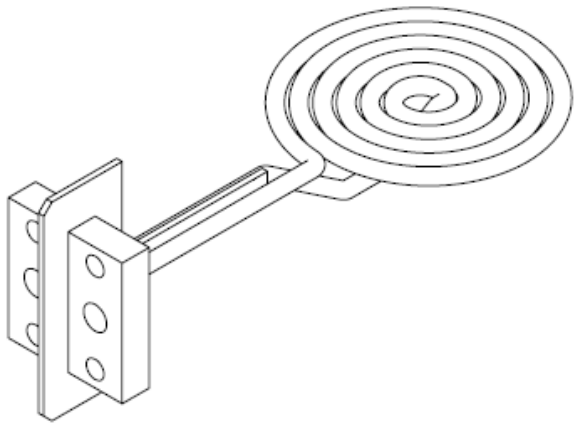

Figure 3-12. Schematic view of inductor coil, image supplied by Hüttinger Elektronik, Freiburg

With a diameter of 80mm and a wire diameter of 5mm the coil has an inductance of 3.2µH. The setup runs at a resonant frequency of 220kHz.

3.3.2 Workbench

Knowing the dimensions of the tank circuit the workbench could be designed. The workbench should consist of two parts – a height adjustable worktop with some sort of press to fix the workpiece and to apply pressure during bonding and a frame containing the tank circuit and worktop.

For the worktop a plastic board was fixed on an ordinary lab jack. At the end of the board a leaf-press construction was proposed, using transparent acrylic slides and threaded plastic rods. Weights can be put onto the bottom slide to increase pressure. A part of the worktop's bottom side was countersunk to decrease the minimum working distance. The whole design is shown in Figure 3-13:

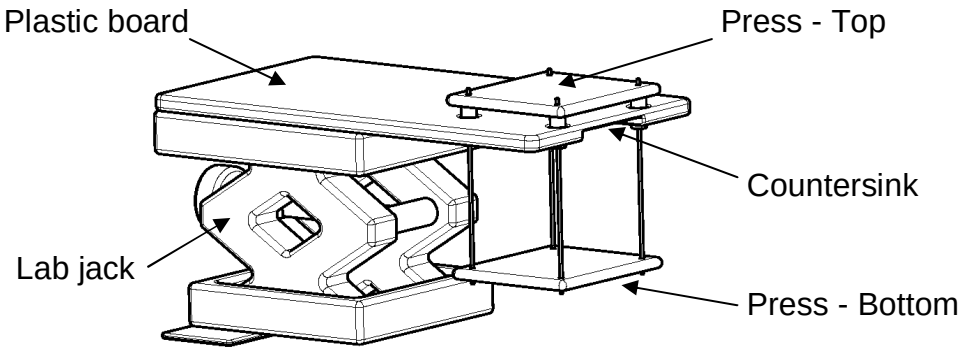

Figure 3-13. Schematic view of worktop with press designed with CATIA

The frame then was made using metal profiles and aluminium boards at two levels. The first board was to fix the tank circuit the second to fix a camera or any other instrument. Two “legs” were included to be able to fix the worktop (see Figure 3-14).

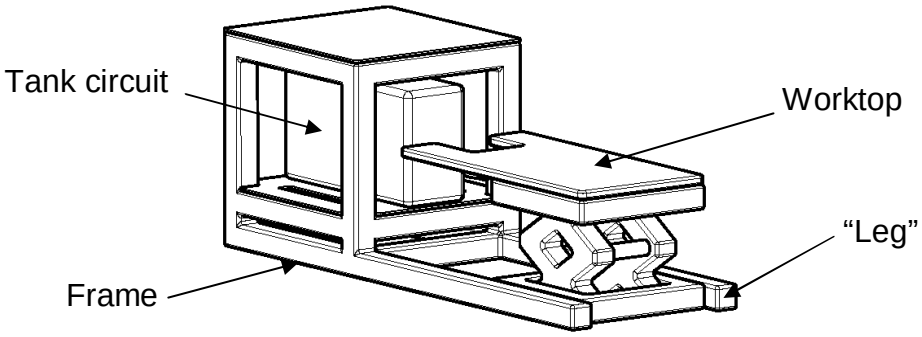

Figure 3-14. Schematic view of workbench designed with CATIA

The whole design was realised by the University’s workshop. The construction is shown in Figure 3-15.

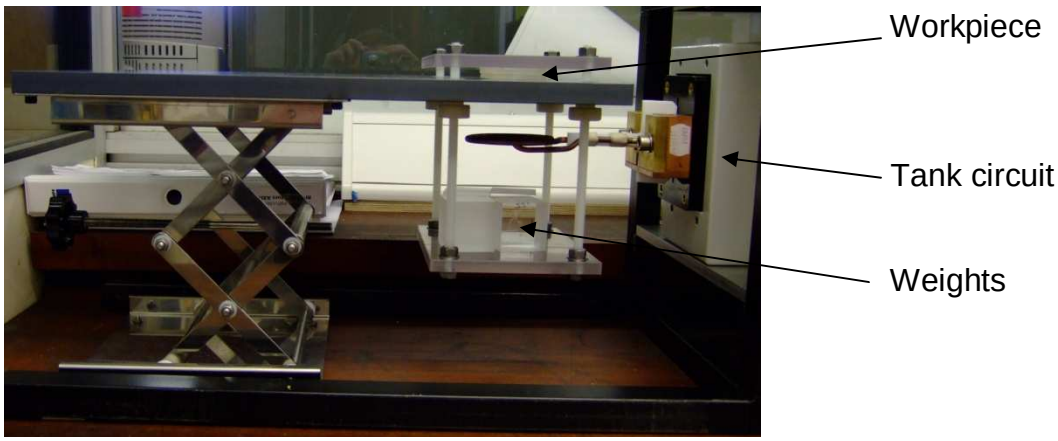

Figure 3-15. Worktop with press and inductor coil

3.3.3 Temperature Measurements

For contactless measurements of the workpiece's temperature a thermal imager was used. Three different types of thermal cameras were used dependent on availability.

A FLIR SC3000 ThermaCAM (temperature range: -20℃ – 1500℃; accuracy: ± 1℃) was used for initial trials, a FLIR ThermaCAM E45 (temperature range: -20℃ – 250℃; accuracy: ± 2℃) for planning and des igning new experiments, and a FLIR ThermaCAM PM695 (temperature range: 0℃ – 500℃; accuracy: ± 2℃) for later experiments.

Each imager was mounted on a tripod and placed above the workpiece focussing on the susceptor's surface. Depending on the camera model the emissivity was set manually to that of the susceptor material or the material in the camera software, so that the right emissivity was chosen automatically.

To verify the use of an emissivity of 0.37 for nickel, a piece of nickel foil was put on a heat plate and heated to a given temperature. A FLIR ThermaCAM E45 was used to measure the temperature. With the emissivity set to 0.37 the measured temperature was identical to the temperature set at the heat plate.

3.4 Numeric Modelling

Before ordering equipment and running experiments the effect of different parameters on the heating rate first was investigated using numeric models. Those models also proved valuable when the effect of a single parameter like the workpiece's resistivity had to be investigated without altering its other properties or when the object being investigated was hard to realise experimentally, e.g. thermal barriers of different sizes. For the modelling COMSOL Multiphysics software was used.

Three model setups were used to represent different aspects of the system under investigation, and the dimensions of the geometry modelled in each case were adjusted to suit the different tasks. All models were meshed automatically with a triangular mesh.

3.4.1 Induced Eddy Currents

The first model was designed to solve for the vector potential as a function of position. The current density in the workpiece then could be extracted from the vector potential. According to COMSOL Multiphysics the domain equation was as follows:

$$(j\omega\sigma - \omega^2\varepsilon)A_\varphi + \nabla\times(\mu^{-1}\nabla\times A_\varphi) = J_\varphi^e \qquad (3\text{-}2)$$

Where

ω: Angular frequency

σ: Electric conductivity

μ: Permeability

ε: Permittivity

J_φ^e: Current density due to an external source (i.e. inductor coil)

A_φ: Vector potential

The model required boundary conditions for the exterior boundaries as shown in Figure 3-16.

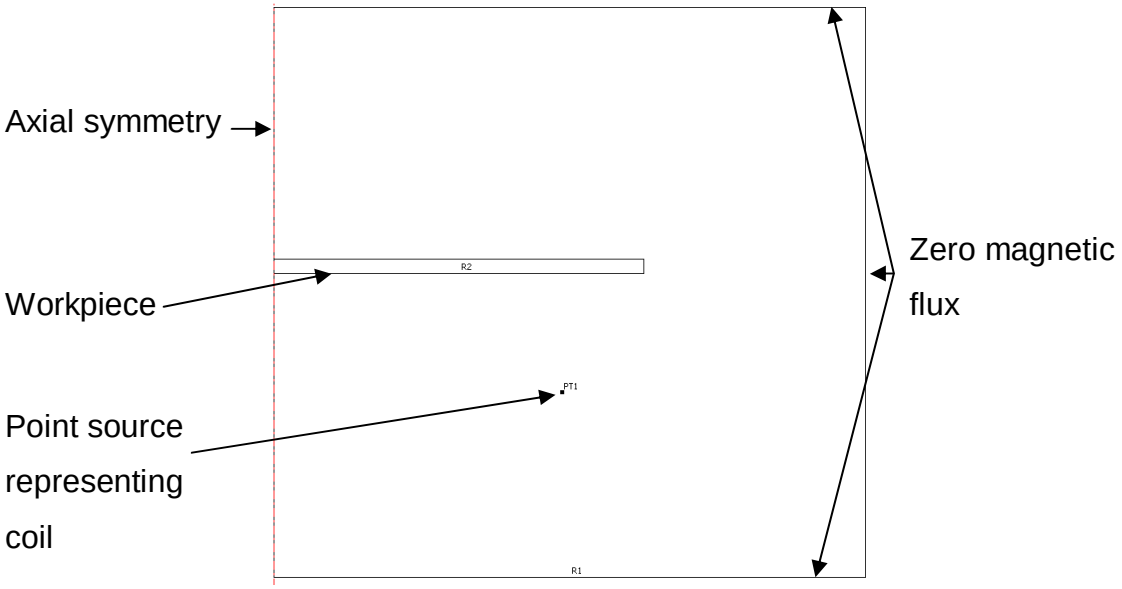

Figure 3-16. COMSOL model for simulating eddy currents with boundary conditions

The left border was set to be the symmetry axis while for the other three a condition corresponding to zero magnetic flux was set. The schematic in Figure 3-16 is only to illustrate the boundary conditions and is not to scale.

3.4.2 Coupled Model of Induced Currents, Workpiece Heating & Conductivity Change

In a second model the temperature field in the workpiece due to joule heating by eddy currents was solved for. The model was run with and without temperature dependence of conductivity.

Two domain equations were used to simulate inductive heating:

$$j\omega\sigma(T)A + \nabla \times (\mu^{-1}\nabla \times A) = 0 \qquad (3\text{-}3)$$

$$\rho C_p \frac{\partial T}{\partial t} - \nabla \cdot k \nabla T = Q(T, A) \qquad (3\text{-}4)$$

Where

σ: Electrical conductivity

ρ: Density

C_p: Specific heat capacity

k: Thermal conductivity

Q: Power of inductive heating

A: Vector potential

The electrical conductivity of the workpiece was given by the expression

$$\sigma = \frac{1}{[\rho_0 (1 + \alpha (T - T_0))]} \qquad (3\text{-}5)$$

Where

ρ_0: Density at reference temperature T_0 = 293 K

α: Temperature coefficient of the resistivity

T: Actual temperature in the domain

And the heating power is given by

$$Q = \frac{1}{2} \cdot \sigma \cdot |E|^2 \qquad (3\text{-}6)$$

Where

E: Electric field obtained from the vector potential

In addition to the zero magnetic flux condition the exterior boundaries were set to be thermal insulators. To simplify the model the air surrounding the workpiece was assumed to be not moving. Hence the heat transfer from workpiece to air was simulated as heat conduction, not convection. Heat

radiation from the workpiece was ignored. In the simulations the temperature at exterior boundaries was not seen to increase, so the simulation domain was judged to be large enough.

3.4.3 Effect of Thermal Barrier (Air Gap)

The third model was designed to examine the temperature profile in the sample, where there is an air gap between the sample and the heat source. This time a simple two dimensional model without symmetries was used. The domain equation for the heat conduction model was

$$\nabla \cdot (-k\nabla T) = 0 \qquad (3\text{-}7)$$

Where

k: Thermal conductivity

The model consisted of two layers, one with the effective thermal conductivity of air and the other with the thermal conductivity of PMMA at room temperature (see Figure 3-17).

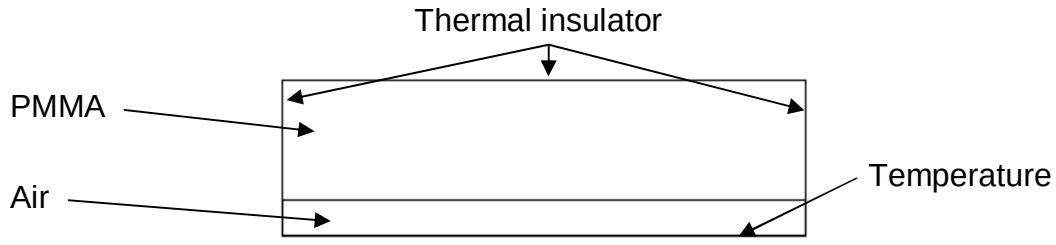

Figure 3-17. COMSOL model for simulating heat conduction with boundary conditions

The bottom border of the model was set to a chosen temperature representing a heater while the other three borders were set to be thermal insulators. The air gap could be varied and the temperature profile through the model extracted.

4 Initial Trials & Heating Investigation

At the beginning of the study it was not clear that low frequency magnetic fields would heat thin susceptor materials sufficiently to seal and interconnect microfluidic devices. Initial trials were therefore conducted to determine the suitability of the process. The trials had the additional aims of qualifying equipment for purchase, identifying suitable susceptor materials and carrying out an outline investigation of how different process parameters such as heating time, working distance, etc. would affect the heating rates achieved.

4.1 Initial Trials

In order to confirm that induction heating is capable of sufficiently heating thin susceptors, metal foils were purchased to be tested by suppliers of induction heating equipment. To design a test setup it was critical to know the temperature needed to melt/bond polymers. Table 4-1 shows the melting temperature and glass transition point (the softening temperature) of selected thermoplastic polymers.

Table 4-1. Properties of Selected Thermoplastic Polymers

Polymer		Melt Temperature ℃	Glass Trans. Point ℃
Polyamide	PA	220-260	50-75
Polybutylene terephthalate	PBT		60
Polycarbonate	PC	267	150
Polyethylene	PE	130-145	
Polyetheretherketone	PEEK	350	130-150 / 260-290
Polyethylene terephthalate	PET	260	75
Polymethyl methacrylate	PMMA	130-140	105
Polypropylene	PP	165	
Polystyrene	PS	240	95
Polytetrafluoroethylene	PTFE	327	
Polyvinyl chloride	PVC	212	87

250℃ was decided to be an appropriate target tempe rature to be attained in the first trials as it is in the higher range of the melting temperatures listed and higher than all the glass transition points.

To establish an operating window for the process two different materials with two different thicknesses were used. Nickel and steel were chosen as materials to be tested as they are good susceptors and widely used. For the application it is desirable to use very thin susceptors so the thickness of the metal foils had to be between 5 and 10µm. Foils with at least three times the thickness were obtained as well, to gain some knowledge about the heating capabilities in case the thin foils were impossible to heat to target temperature. With price being another factor the decision was made to order nickel foils with thicknesses of 25µm and 7.5µm and steel foils with thicknesses of 100µm and 10µm.

The sample foils were sent to Cheltenham Induction Heating (CIH) to test the capability of their Easy Heat System. The system has a frequency range of 150 to 400kHz and depending on the generator, an output power of 1.2 to 10kW. The nickel steel foils had to be heated to 250℃ in ductively with a pancake

shaped coil. It was not possible to use a thermocouple for measuring the temperature as the thermocouple would be heated by the alternating magnetic field itself. Thus to indicate the temperature reached CIH used Tempilaq®, a heat sensitive paint changing its colour when a trigger temperature is reached. There are many different paints for different temperatures.

In Figure 4-1 steel of 100µm thickness covered with a paint that changes its colour from white to black at 250℃ is shown.

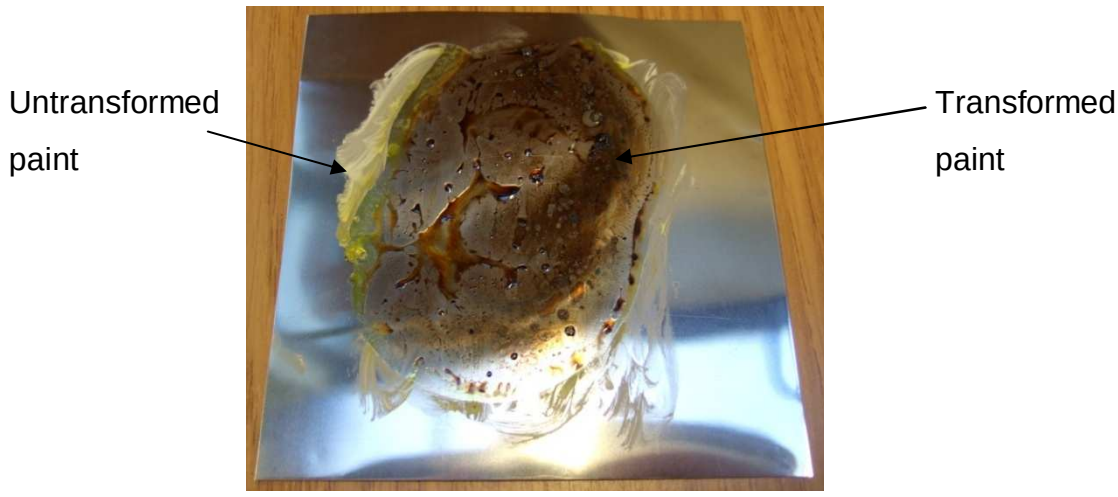

Figure 4-1. Tempilaq® on steel foil

It can be seen that there are some areas with untransformed Tempilaq®. According to CIH this was due to the inductor being smaller than the foil and hence heating only the centre area.

A second batch of 7.5µm thick nickel foils were sent to Giltron Inc. Washington D.C., USA, who heated them with a 13.5MHz unit, and to Hüttinger Elektronik in Freiburg, Germany, who tested them with their AXIO induction heater (50 – 800kHz, 5 - 10kW).

A test protocol (see appendix *A2 Test Setup*) was sent to the companies along with the foils to ensure comparable results. All companies reported being able to heat the foils in milliseconds to the demanded temperature.

4.2 Experiments at Hüttinger Elektronik

Following the initial experiments a more detailed evaluation was carried out in the testing facilities of Hüttinger in Freiburg, Germany from 29.01. to 31.01.2008. The aim was to evaluate the potential and limitations of induction heating systems and to get an idea of how the equipment works and what kind of equipment best fits the project's purposes.

4.2.1 Design of Experiment

From the thermoplastic polymers mentioned in Table 4-1, polymethyl methacrylate (PMMA) was chosen to be used during this project because it is commonly used for manufacturing microfluidic devices. It is benign to most of the fluids used in medical applications, it is soluble only in a few solvents (e.g. acetone), and monitoring the experiments and analysing the bonds is made easier by PMMA being transparent.

Repsol Glass® PMMA slides with a size of 36mm x 36mm and a thickness of 4mm were used as substrates for all samples. Before preparation the substrates were analysed by Differential Scanning Calorimetry (DSC). The result shown in appendix *A3 Differential Scanning Calorimetry (DSC)* displayed a glass transition point at about 113℃ and a melti ng point at 170℃.

Some initial tests had to be carried out to get an idea of the appropriate range of power and frequency. A nickel foil with a thickness of 7.5µm and an edge length of 25mm supported by a non-conductive worktop was used for this initial part. Again nickel was chosen because of its good performance as a susceptor.

For the second experiment a nickel foil with the same dimensions as the foil used in the initial tests was placed between two substrates. The foil was heated inductively, thus melting the surrounding polymer and creating a bond directly between the polymer slides.

To create a bond between nickel and polymer, substrates were coated with 5µm thick nickel layers (see Section *3.2.3 Preparation*) and bonded to PMMA slides.

A fourth experiment was prepared to test the limitations of the induction heating units. A 50-100nm thick nickel layer was coated onto a PMMA substrate (see Section *3.2.3.1 Evaporation*) and was heated using different coils and frequencies.

To be able to test how the area of the susceptor effects the heat dissipation, a small piece of the 7.5µm thick nickel foil was placed between to PMMA substrates. This setup was heated using low frequency induction heating and the maximum temperature was specified.

Two samples were prepared to allow leak tests after bonding. The samples were made of a nickel foil with a punched hole put between a substrate and a lid with a hole. Through the hole in the lid the system could be pressurised after bonding.

Samples in which there was expected to be no hysteresis heating were prepared by choosing the susceptor to be aluminium. Aluminium is diamagnetic so hysteresis heating is impossible. Substrates with 5µm thick layers were prepared (see Section *3.2.3.3 Sputtering*) to investigate the relative magnitude of hysteresis and eddy currents in heating the susceptor.

To be able to provide a comparison of bond strengths between PMMA to nickel and PMMA to aluminium, one of the aluminium coated samples was bonded to another PMMA substrate.

To apply pressure between the two pieces of PMMA to be joined an ordinary plastic G-clamp was used for all experiments.

4.2.2 Execution of the Experiments

Apart from two experiments with a IG 2MHz unit, all tests were carried out with an AXIO 10-450 with a maximum power of 10kW and frequencies of up to 800kHz. A pyrometer was used to measure the temperature on top of the upper substrate (not at the susceptor directly) and its signal was used in a feedback control loop to control the output power. Figure 4-2 shows the basic setup:

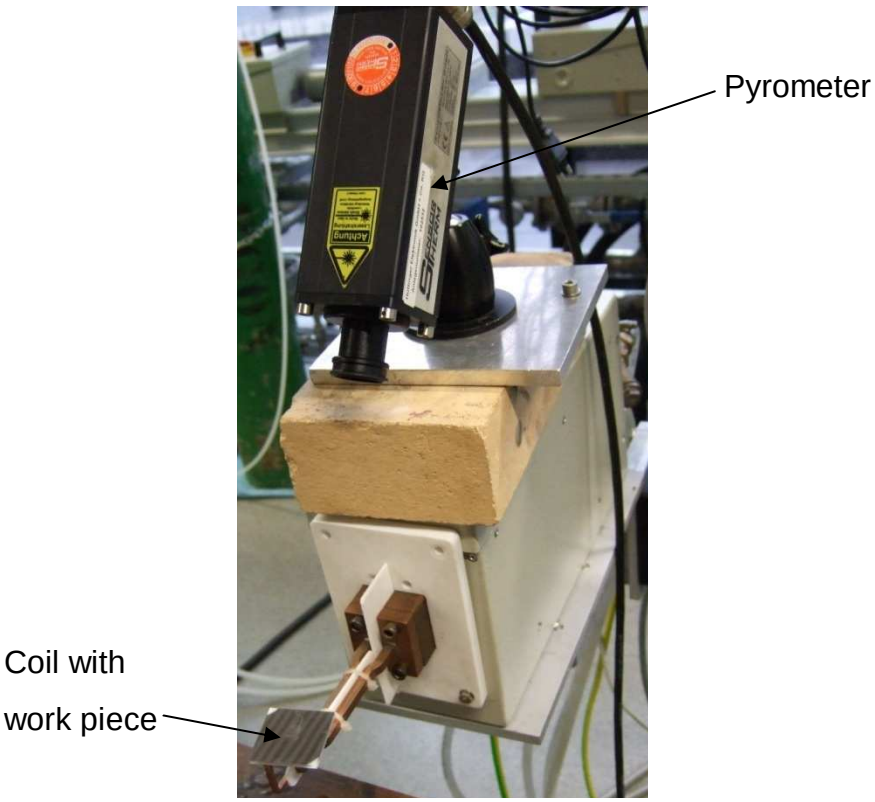

Figure 4-2. Test setup without G-clamp

During the experiment different coil designs inducing different kinds of current flow patterns were adopted. First a pancake shaped coil as shown in Figure 4-3 was used.

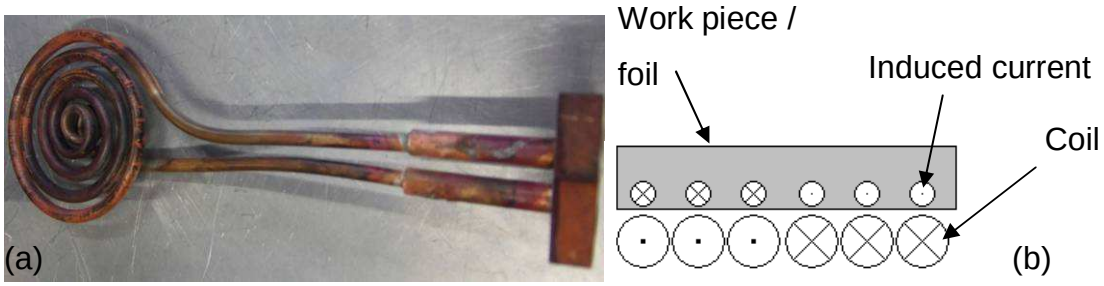

Figure 4-3. (a) Multi turn pancake shaped coil and (b) Flow pattern of induced current

The current induced by a pancake shaped coil flows in opposite direction of the current in the coil.

The second design was an “s-shaped” coil as shown in Figure 4-4. The specific characteristic of this coil is the current flow in its middle. The windings are arranged in a way that the middle set have a current flow in the same direction.

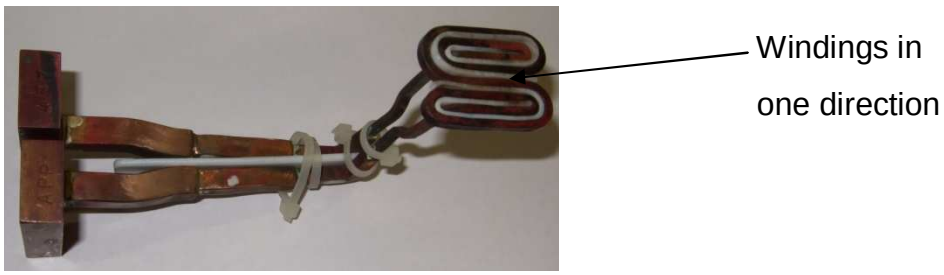

Figure 4-4. "s-shaped" coil

The advantage of this arrangement is that the induced currents all flow in the same direction, providing a more homogeneous heat dissipation. The induced current pattern is as shown in Figure 4-5:

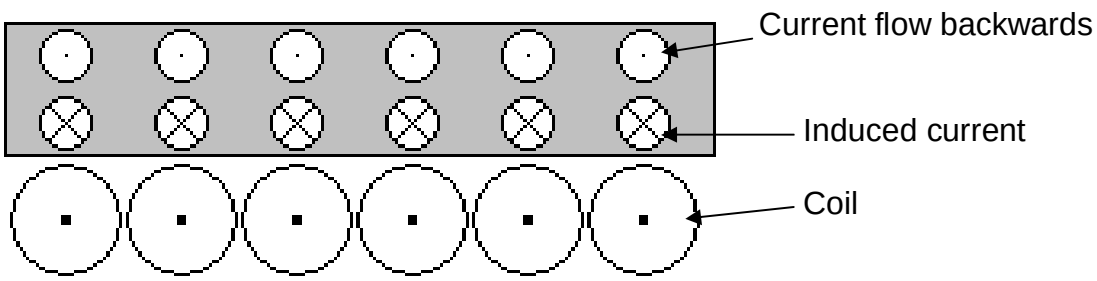

Figure 4-5. Current flow pattern with an "s-shaped" coil

For high penetration depth relative to the workpiece thickness this pattern of flow causes a drop in coupling efficiency.

A very common coil is the tunnel coil.

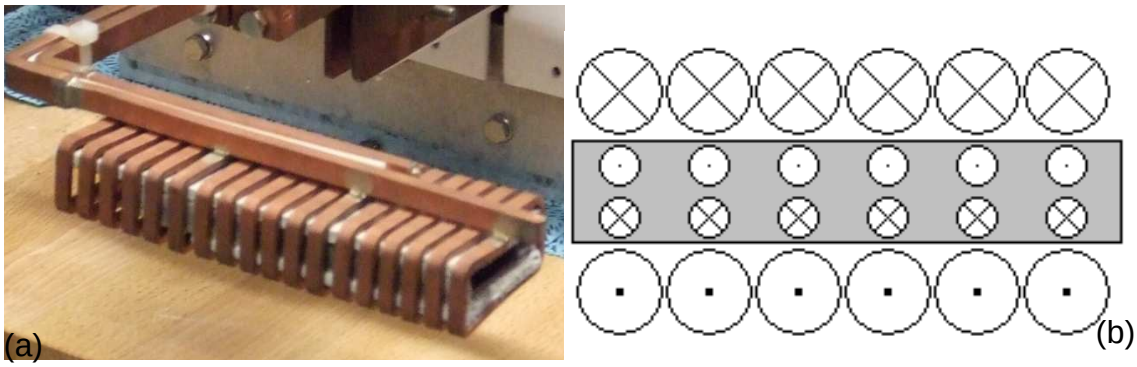

Figure 4-6. (a) Tunnel coil and (b) Flow pattern of induced current

As shown in Figure 4-6 the current flowing backwards is also induced. A tunnel coil doesn't have to have a rectangular shape. For heating pipes a cylindrical coil has a good coupling efficiency.

The last coil that was used was a linear coil (Figure 4-7). This design is used to selectively heat a part of a work piece. As the resistance of this coil is low a higher induction current can be applied.

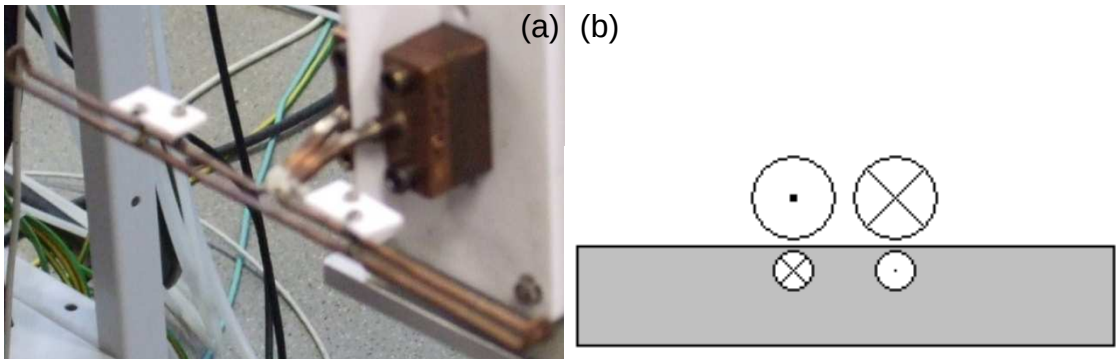

Figure 4-7. (a) Linear coil and (b) Flow pattern of induced current

The flow patterns shown in Figure 4-3 to Figure 4-7 are a simplification of the real current flow, which is difficult to predict. The width of the coil conductor,

distance between each winding and size of the workpiece affect the flow path. Also the skin effect has to be considered. The induced currents generate a magnetic field themselves, counteracting the field of the induction coil. Thus the area in which currents can be induced is limited (penetration depth). The magnetic fields of induced currents, which are flowing in opposite directions (see Figure 4-7b), can also force them to the outside of the workpiece.

4.2.3 Results

Full details of the tests described below are given in appendix *A5 Test Series at Hüttinger Elektronik*.

4.2.3.1 Initial Test

For the initial tests a multi turn pancake shaped coil driven by the Axio system as shown in Figure 4-3 was used first. The frequency, which was varied between around 180 and 350kHz by changing the capacitors in the tank circuit, did not seem to influence the heating rate greatly, but coupling distance and output power did. As shown in Figure 4-8 there were hot spots at the corners of the foil.

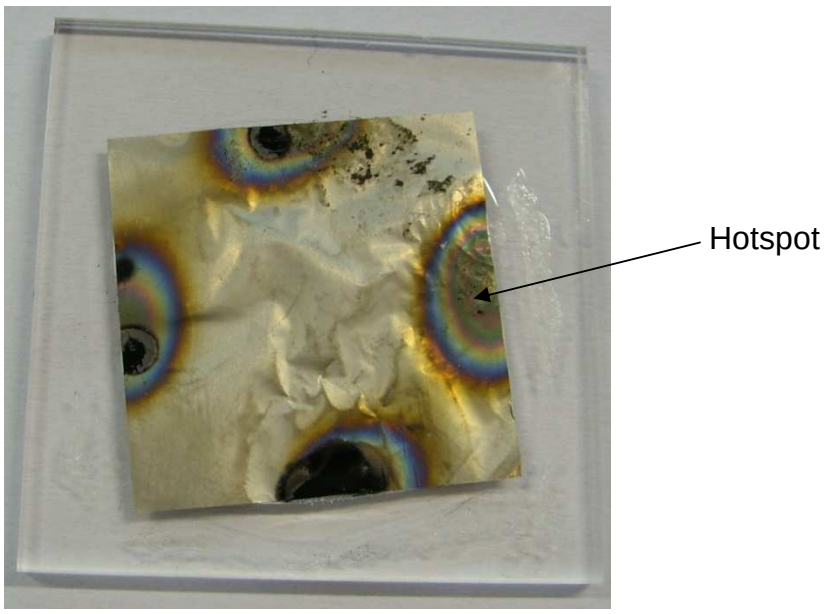

Figure 4-8. Foil with hotspots

To avoid the hotspots with providing a more homogeneous heat distribution the “s-shaped” coil shown in Figure 4-4 was then used. No hotspots were seen. To exclude the possibility that this was due to the coil being smaller than the work piece a larger coil with about 15 windings in the same direction was used as shown in Figure 4-9:

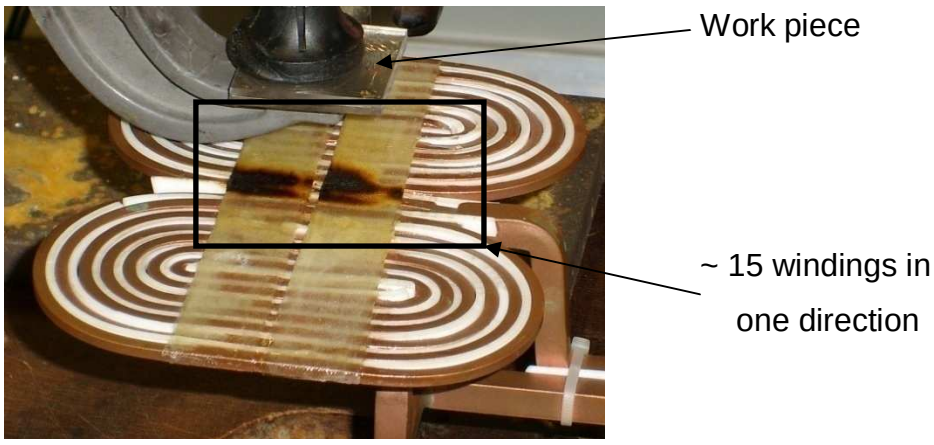

Figure 4-9. "s-shaped” coil

There were some hotspots but the difference between the heating rate at the corners and at the rest of the foil was decreased.

4.2.3.2 Bonding Trials

After the initial process characterisation tests it was decided to use a frequency of about 250kHz and 80% output power, using the larger s-shaped coil shown in Figure 4-9, to create the bonds between two PMMA substrates sandwiching a nickel foil. The nickel foil melted the surrounding polymer in a few seconds and created a bonding area as shown in Figure 4-10.

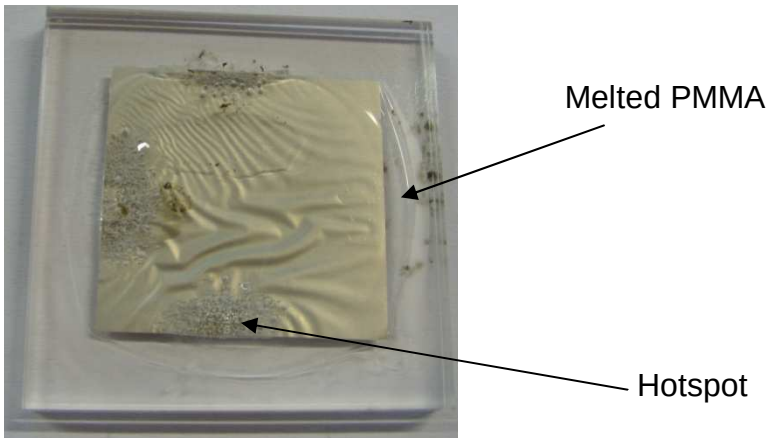

Figure 4-10. Bonded PMMA slides

To create bonds between PMMA and nickel the same experimental setup was used but instead of using a foil as intermediate layer a PMMA substrate coated with 5µm nickel (see Section *3.2.3.2 Electroplating*) was bonded to a blank one. As the electroplated nickel layer was thinner than the foil used before, the output power was increased (to 100%). A bond was seen to be created, but as one corner of the stack was too close to one centre of the coil (where the induced current distribution pattern would be similar to that of a spiral coil) the nickel in this area started to glow and burned the PMMA (see Figure 4-11).

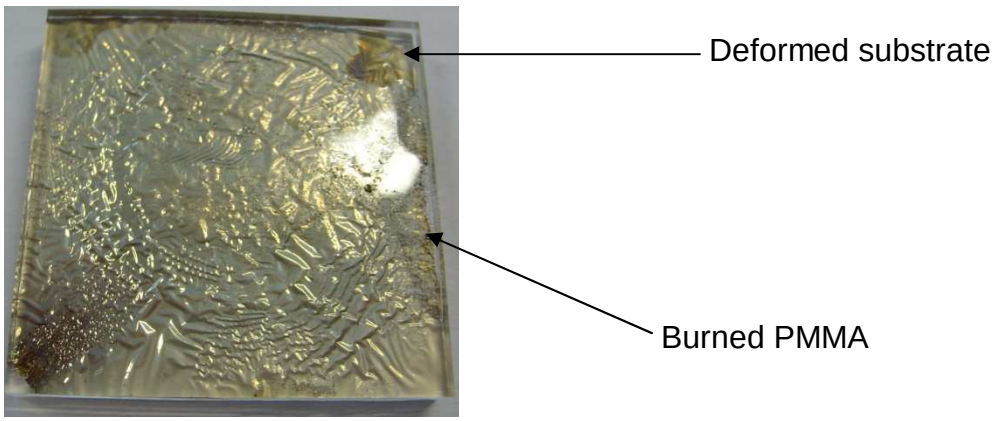

Figure 4-11. PMMA bonded to nickel

During the test the substrates were found to heat substantially with the temperature of the top layer reaching 103℃, implyi ng a much higher temperature at the middle of the stack. As the feet of the clamp were smaller than the PMMA slides, the slide edges bent downwards, indicating that the stack temperature had reached the forming temperature of PMMA.

Another test with a similar setup was processed but instead of using the previous control method (constant power until temperature on top of the upper substrate reached the setpoint) a slow heating curve was implemented. After slowly heating up the complete system to about 50℃ , small pulses of full power were applied to make the polymer in contact with the susceptor melt without heating up the whole substrate. Using this method a bond could be created without deforming the substrates.

For all experiments so far temperature was measured on the top of the upper substrate. It was thus not possible to measure the temperature in the nickel layer. To be able to focus the pyrometer directly on the susceptor material one edge of a PMMA lid was cut off. The nickel exposed was coloured black with a permanent marker as the pyrometer was optimised for non-reflecting surfaces (Figure 4-12).

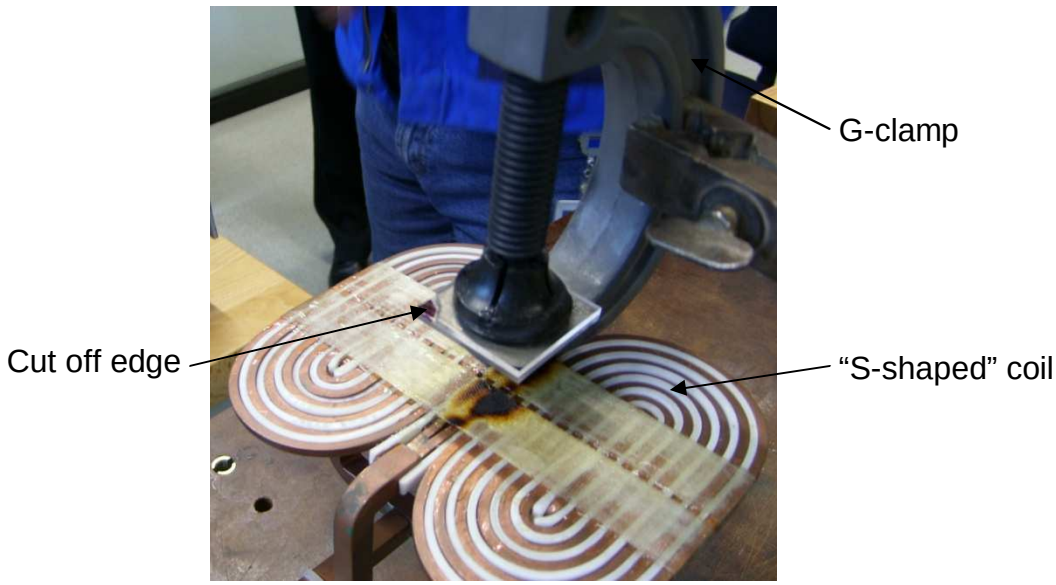

Figure 4-12. Setup to identify generated heat

With full output power and a frequency of 250kHz the nickel layer was observed to heat up to more than 260℃ in 25 seconds when the sample was located over the parallel section of the coil. It would be expected that the heating rate would be much larger if the sample were to be located over either of the spiral sections.

This effect could be observed during the next test. The substrate with the 50-100nm thick nickel layer was heated with different coils at different frequencies. To avoid destruction of the thin coating the temperature was measured on the backside of the substrate with a thermo-couple after switching off the power generator. When positioned in the middle of the s-shaped coil it was found not possible to heat the substrate, but heating was seen when placed on one of the spiral sections. To allow higher frequencies a smaller pancake shaped coil with a lower inductivity was used next:

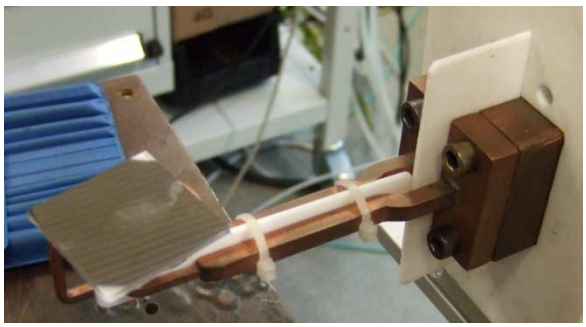

Figure 4-13. Test setup with small pancake shaped coil

As shown in Figure 4-13 the work piece was put directly onto the coil to further increase coupling strength. In addition to these coils two other designs were used at frequencies between 150 and 700kHz (AXIO) and at 2.2MHz (IG). These other coils were the tunnel coil (Figure 4-6) and a linear coil (Figure 4-7) described in Section *4.2.2 Execution of the Experiments*. The temperature on the back of the substrate reached temperatures between 50 and 60℃ every time, independent from the coils or frequencies used. This result is surprising as it indicates that frequencies and penetration depths accessed don't affect the heating rate substantially.

To test the limits of the AXIO system a small piece of nickel foil was put between two substrates and placed over the centre of the spiral section of the 15 turn s-coil. The longest corner of the piece was about 6mm.

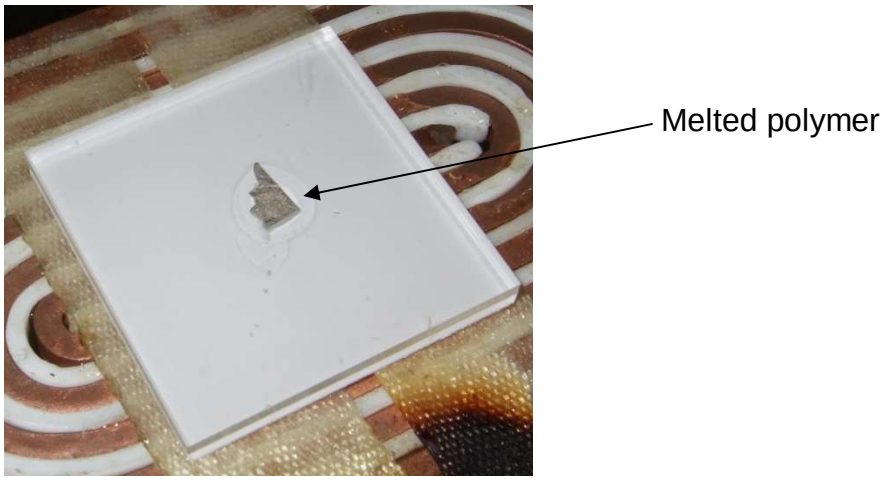

Figure 4-14. Small nickel piece creates bond

The PMMA was observed to melt rapidly over a large area around the foil. In Figure 4-14 the melted area can clearly be seen. The experiment was stopped when the temperature measured on back of the lower substrate reached more than 220℃. During cooling a bond was created betwe en the two substrates which was too strong to be broken manually. This test proved that it is possible to heat up small structures very efficiently and melt the surrounding material, creating a bond.

After these experiments the two samples for testing the bond strength with pressure were prepared (see Figure 4-15). The setup was fixed with a G-clamp and heating the foil created the bond.

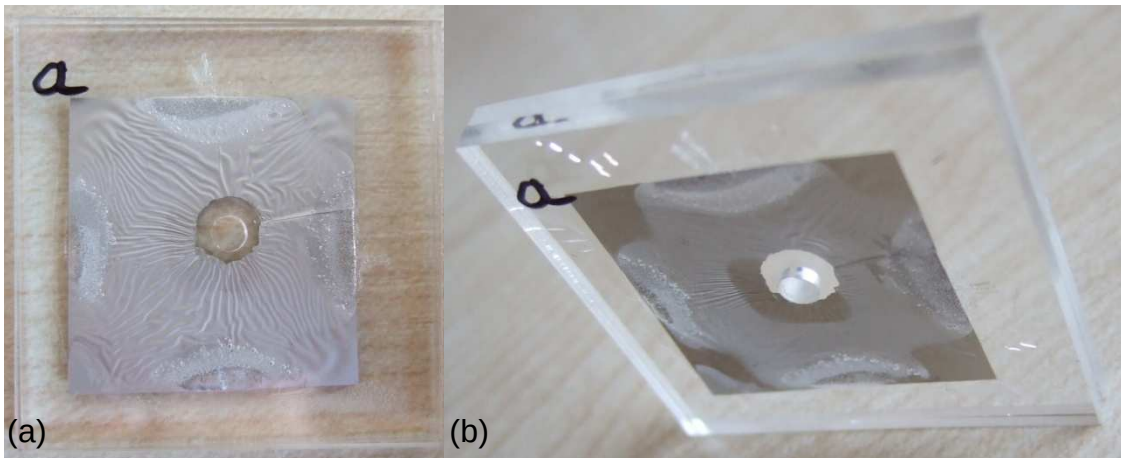

Figure 4-15. Sample for pressure test: (a) Top view and (b) General view

For the two samples two different parameters were used during bonding. For one sample 80% of the output power was used for 6.6s and for the other 60% of the power was applied for 27.75s. Both profiles produced an apparent seal by visual inspection.

Finally the aluminium coated substrates were tested. A linear and a pancake shaped spiral coil were used with the AXIO generator and good heating rates were observed with both. For instance using minimum coupling distance (sample lying on coil) and the pancake shaped coil at a frequency of 250kHz

with 50% of the output power the aluminium layer was heated to a temperature, as measured on the pyrometer, of 175℃ in 5s, altho ugh this temperature is inaccurate because aluminium is bright while the pyrometer is optimised for dark surfaces. While the coupling efficiency appears to be not as good as with a nickel susceptor, the test is an indication thin layers of diamagnetic metals can also be heated.

A blank substrate then was bonded onto a 7µm thick sputtered aluminium layer to provide a comparison of bond strengths between PMMA to nickel and PMMA to aluminium. The bond was created in 5.6s using 60% output power. The sample is shown in Figure 4-16.

Figure 4-16. PMMA bonded to aluminium

The irregularities in the aluminium layer visible in the figure originate from the coating. It appears sputtering of such thick layers onto plastic substrates produces a poor quality coating and it was observed that the coating was peeling even before bonding.

4.2.4 Testing the Samples

A cross section view of the sample bonded with a 7.5µm thick nickel foil as susceptor (see Figure 4-10) was made. As shown in Figure 4-17 a bond area of about 400µm width was observed at the edge of the foil.

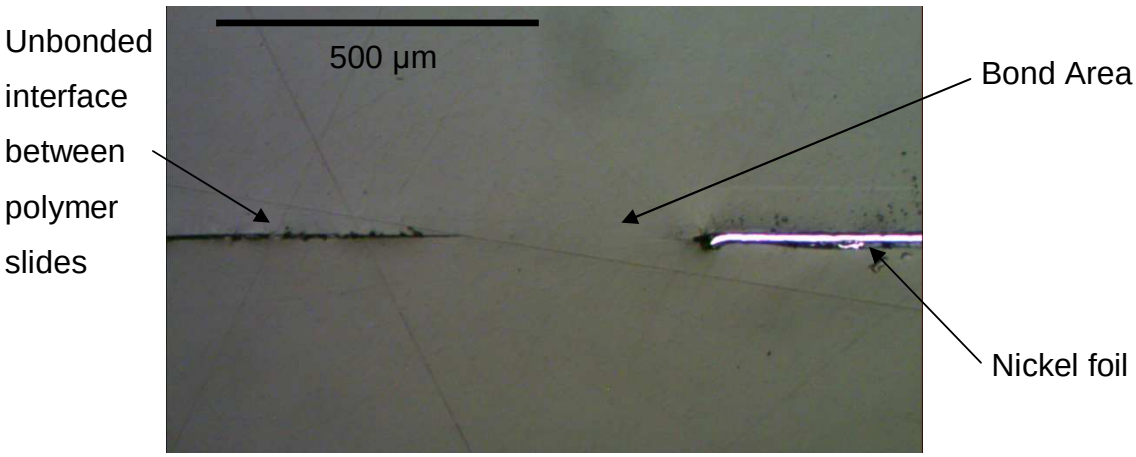

Figure 4-17. Bond Area

For the pressurising tests a tube was connected to the hole in the sample lid and fixed with epoxy. The tube then was connected to a pressurised air line via a valve and a pressure gauge and the samples were put into a water bath to identify any leaks.

Sample *b* withstood an air pressure of 70kPa for more than 60s but showed leakage at 140kPa. As shown in Figure 4-18 the leak was at the interface area of the two substrates:

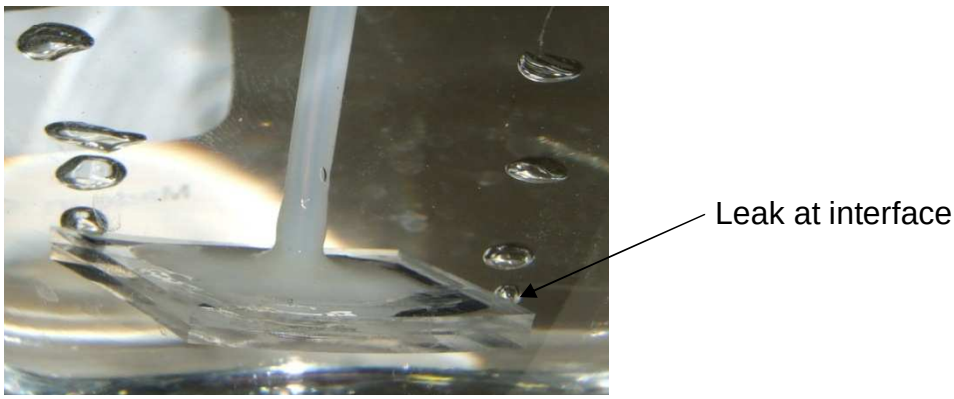

Figure 4-18. Sample b leaking

Sample *a* withstood a pressure of up to 590kPa, at which point the adhesive joint to the connector tube failed (Figure 4-19).

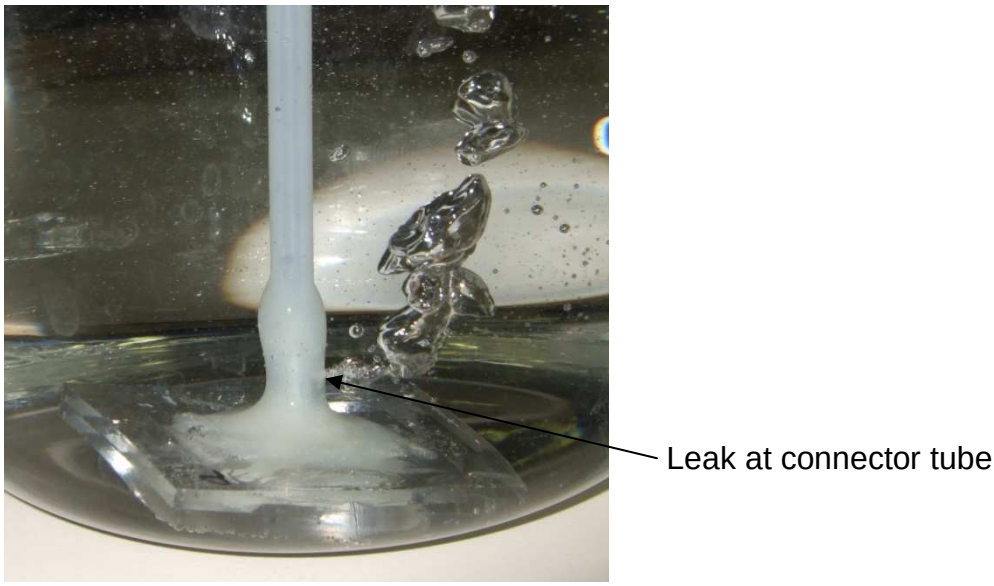

Figure 4-19. Sample a leaking

590kPa was the maximum pressure that could be applied so the sample could not be tested at higher pressure.

4.3 Conclusions

The work at Hüttinger in Freiburg demonstrated that it is possible to create bonds in polymer stacks containing thin metal layers – both ferromagnetic and paramagnetic using low frequency (< 1MHz) induction heating. Although it was found possible to create a bond directly between polymer and metal these bonds were not very strong. Bonds formed polymer to polymer in the regions close to the edge of susceptor layers proved to be more robust. Bond areas with a width of 400µm could be identified and one polymer to polymer bonded sample withstood an air pressure of up to 590kPa.

For the process development trials it was identified that an improved method of applying pressure should be devised. With the g-clamp the working distance of the coil to susceptor was more than 4 cm, which decreases the heating rate substantially.

During the experiments a system with 10kW output power was used. Most of the time more than 50% of this power was applied to get good results. This is a lot of energy for heating small metal features, a way to improve efficiency has to be found.

On the basis of the capability demonstrated the Axio equipment was selected for further process development trials and was purchased. The specification purchased and the reasons for this are as follows:

- Variation in frequency up to 2MHz did not produce any significant influence on the heating rates observed so a cheaper power generator with frequencies below 1MHz is adequate.
- The power generator should be capable of at least 10kW.
- The pancake shaped coil showed a very good heating rate for thin susceptor layers and is easy to access.
- A computer control interface to the power generator simplifies experimental setup and handling.

5 Process & Effect of Process Parameters

For a workable process, control of the heat dissipation in the workpiece is a key issue. Processing parameters that can be varied include frequency, the heating time, output current, coil to work piece separation and the coil design. The effects of these variables are explored in this chapter. Other parameters relating to the workpiece and susceptor that can have an effect, such as thickness, shape, permeability and thermal material properties are explored in Chapter *6 Effects of Susceptor Design*.

As only one set of capacitors was available for the equipment, the frequency of the system was fixed. This left three main parameters to control the heat dissipation: output current, working distance, and heating time.

An initial approach to studying these process parameters was made by estimating their effect on the heating rate on the basis of basic physical equations such as the Biot-Savart Law. Those estimations were compared to and validated by simulation and experiment.

An analytical model was then derived from the equations to gain more detailed knowledge about cross-interactions between parameters and how they can be used to control the heating process. The magnitude of effects like cooling, which are not taken account of in the analytical model, were estimated and it was also tested if the model provides good estimates of the magnitude of heating rates.

5.1 Basic Physical Equations

The effects of these parameters on heating rate were first estimated using basic equations and the estimations were compared to the results of numeric models and experiments. The purpose of this study was to gain some knowledge of the principal relationship between heating parameters and heating rate and to create a base for a more detailed analytical model.

In the approach a conductor loop as a simplified model of the coil was assumed as shown in Figure 5-1.

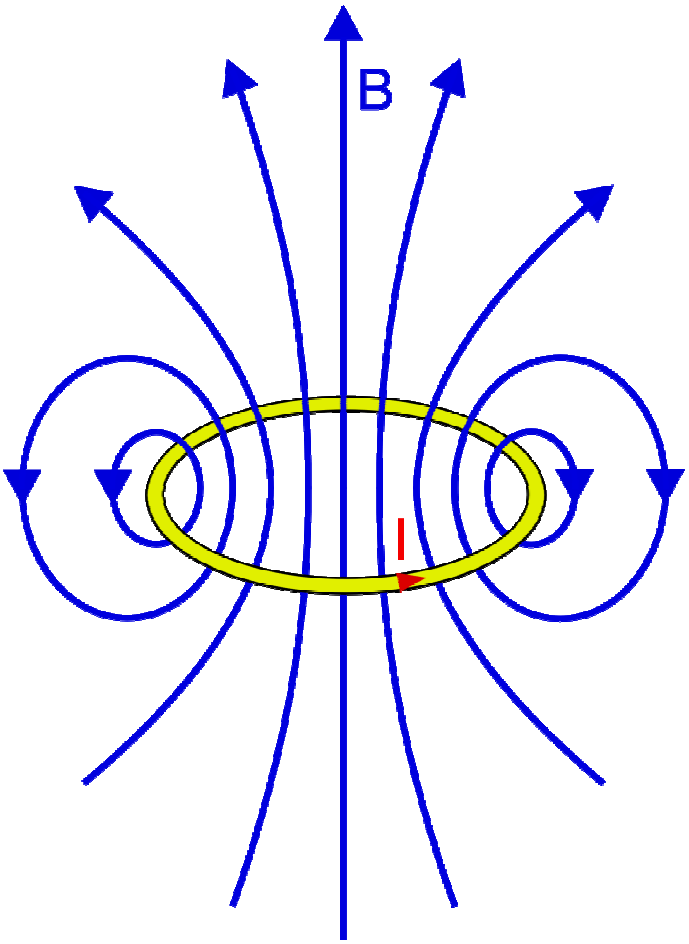

Figure 5-1. Magnetic field (shown by blue lines) due to a current I in a conductor loop (in yellow), re-drawn from [95]

The magnetic flux density B at any point on the loop's axis with a distance x from the conductor's plane can be calculated using the Biot-Savart Law:

$$B_{(x)} = \frac{I\mu_0}{2} \frac{r_Q^2}{\left(r_Q^2 + x^2\right)^{\frac{3}{2}}} \qquad (5\text{-}1)$$

Where

B:	Magnetic flux density	[Vs/m]
I:	Output current	[A]
μ_0:	Magnetic field constant	[Vs/(Am)]
r_Q:	Radius of conductor loop	[m]
x:	Distance from conductor plane	[m]

According to equation 5-1 the magnetic flux density varies linearly with output current. The equation predicts a cubic decrease with distance at larger distances. As the induced current in the workpiece is directly proportional to the rate of change of magnetic flux (see equation 2-1), its dependencies are also determined by equation 5-1.

Thus knowing how the induced current density depends on those three basic parameters it can be assumed how the temperature varies over the parameters as well. The power dissipated in the workpiece can be calculated from $P = R \cdot I^2$ (equation 2-3). As the induced temperature is a function of the dissipated power it would be expected to increase quadratically with output current, and to reduce with distance at larger working distances.

The third parameter to control the heat dissipation is the heating time. The amount of heat generated by a current in the workpiece can be calculated from

$$Q = R \cdot I^2 \cdot t = P \cdot t \qquad (5\text{-}2)$$

Where

Q:	Heat quantity	[J]
P:	Power	[W]
t:	Time	[s]

Thus according to equation 5-2 the generated heat increases linearly with time.

5.1.1 Simulation Results

To validate whether the equations above represent sufficiently accurately the behaviour of a conductive workpiece in the magnetic field of a conductor loop at short distance between conductor loop and workpiece, modelling was carried out using COMSOL Multiphysics. First the model calculating current density as function of position without heating (see Section 3.4.1 *Induced Eddy Currents*) was used. In the model dimensions and heating parameters were chosen to be comparable to those used for the experiments described later in this work. These were a solid disc with a radius of 100mm and a thickness of 100µm placed 60mm above a circular line current representing a coil. The coil had a radius of 40mm. A summary of the model details can be found in Appendix A6.1 *Eddy Current Model*.

First the working distance was held constant and the output current was varied between 1A and 500A. The maximum current density in the workpiece showed a linear variation with the loop current, as shown in Figure 5-2:

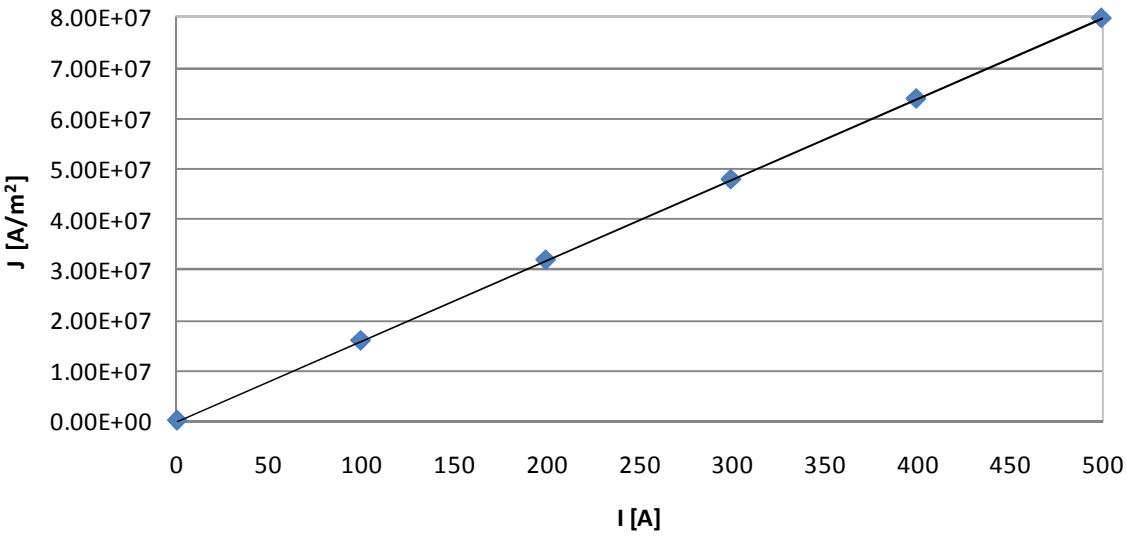

Figure 5-2. Maximum current density in the workpiece plotted against coil current in COMSOL simulation

The output current was then held constant at 140 A while the working distance was varied from 25mm to 50mm. The maximum current density showed a behaviour not incompatible with the inverse cubic decrease with increasing working distance predicted by the basic equations (Figure 5-3):

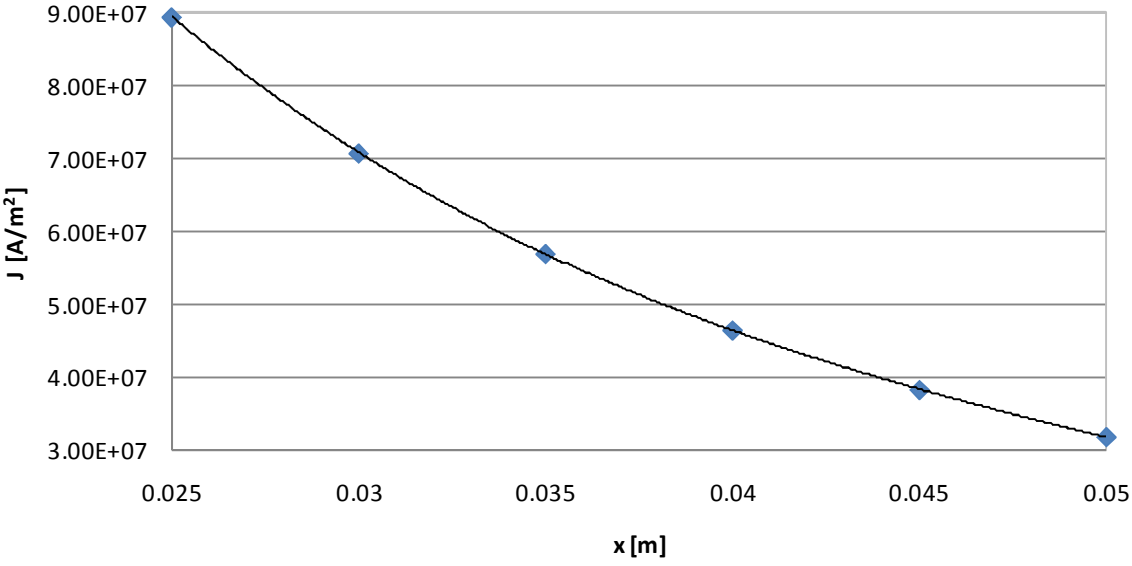

Figure 5-3. Maximum current density plotted against working distance in COMSOL simulation

The generated heat was then simulated as a function of the current density, as described for the second model in Section 3.4.2 *Coupled Model of Induced*

Currents, Workpiece Heating & Conductivity Change. Heating time was set to be 5s. The electrical conductivity of the workpiece was set to a constant value ignoring its temperature dependency. The effect of including this dependency is described in Section *5.3 Change of Resistivity*. A summary of the model details can be found in Appendix A6.2 *Induction Heating Model*.

The result was a behaviour not incompatible with a quadratic relationship between the maximum temperature in the workpiece and the current in the coil as predicted by the basic equations (see Figure 5-4):

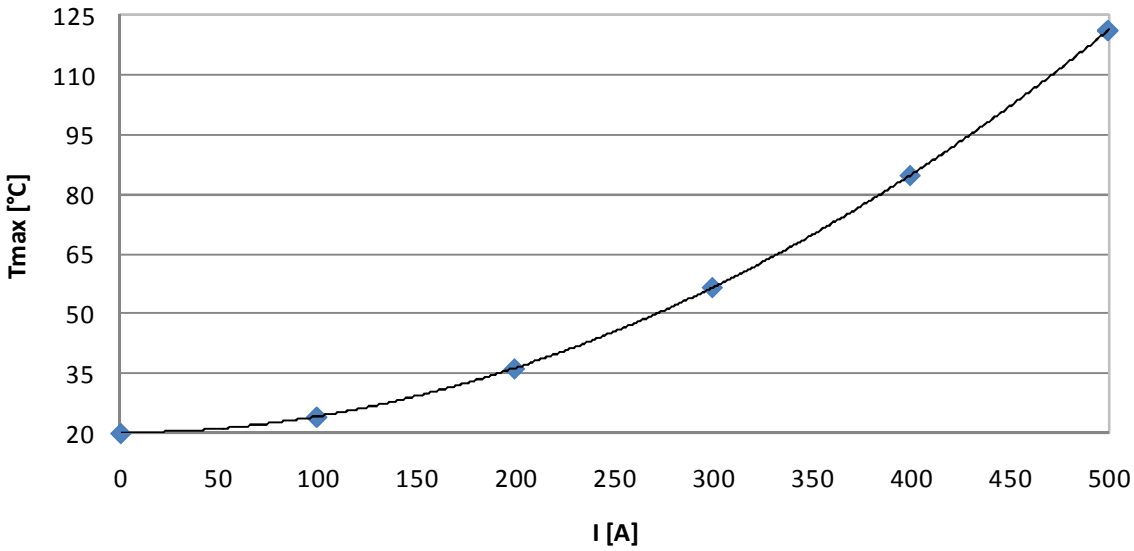

Figure 5-4. Temperature change plotted against coil current in COMSOL simulation

For maintaining the coil current constant and increasing the working distance the relationship observed showed a behaviour not incompatible with the inverse cubic decrease predicted by the basic equations (Figure 5-5):

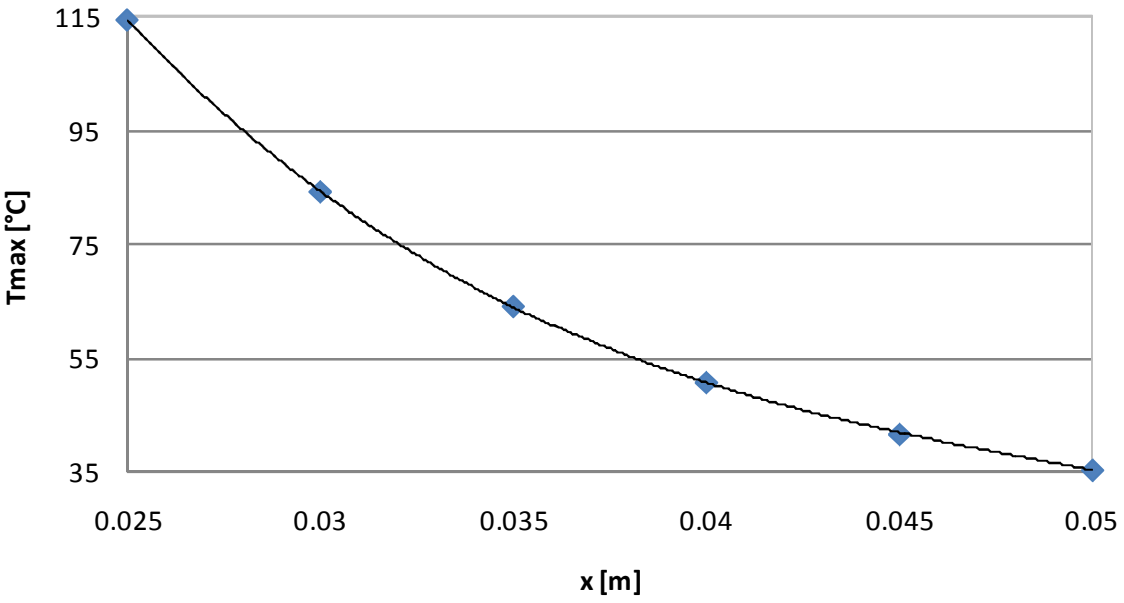

Figure 5-5. Temperature change plotted against working distance in COMSOL simulation

For varying the heating time a linear relationship to the change of temperature was expected and the simulations supported this behaviour (Figure 5-6):

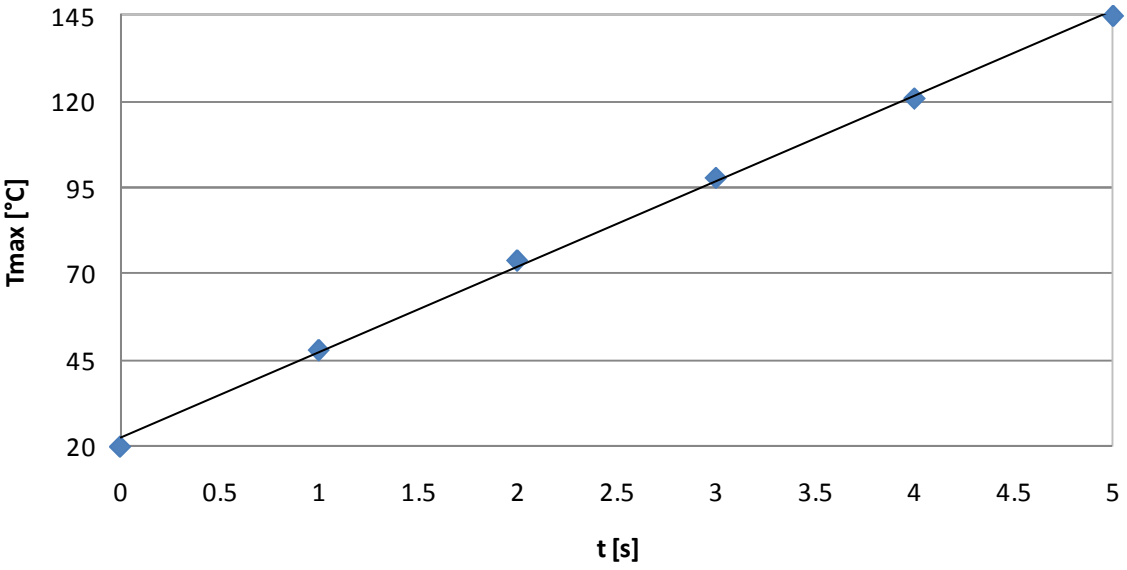

Figure 5-6. Temperature change plotted against time in COMSOL simulation

In the models used in this work for simulating induction heating, the inductor was assumed to be a two dimensional line instead of a three dimensional coil. In the axis symmetric geometry specifications the coil is in fact represented by a

dot. This simplification was needed due to the greatly increased processor times and large number of elements that would be required to model a space filling coil in a geometry with a thin susceptor.

To investigate how the simulated temperatures are affected by this measure a model identical to the one used for the induction heating simulations above was designed. The point source was replaced by a circle with a radius of 2.5mm (which is the size of the experimental equipment used) and a surface current density was applied to it, calculated from the geometry and the set output current. As the heating rate thus produced was lower, the heating time was doubled to 10s. Varying the output current the graph shown in Figure 5-7 may be compared to the results shown in Figure 5-4.

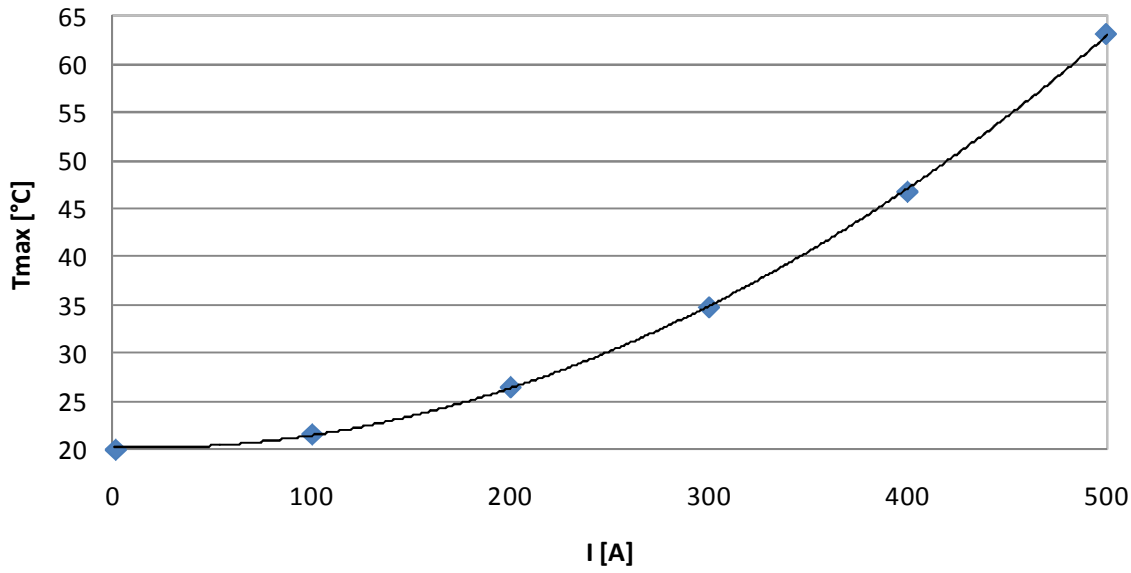

Figure 5-7. Temperature plotted against output current in COMSOL simulation with area inductor

Even with a doubled heating time, temperatures reach only around half the values of the results from the point source simulations. Apparently the current concentration in a single spot leads to higher induced currents. However, the graph in Figure 5-7 shows the same qualitative functional dependency as in Figure 5-4.

5.1.2 Experimental Validation

Experimental validation was carried out with thin susceptor foils of steel and nickel. A Flir ThermaCAM was used to measure the heat generated in the foils by the induction field.

First a 100mm x 100mm steel foil with a thickness of 100µm was tested. A current with a frequency of 220kHz was applied for 5 seconds and the maximum temperature was measured as a function of coil current for working distances of 80mm and 60mm. The temperature showed superlinear variation with the current (Figure 5-8). Also the measured temperatures are close to those simulated in Figure 5-4, bearing in mind that the coils are different, i.e. experimentally a flat multi-turn helix coil was used whereas the inductor in the simulation was a single loop.

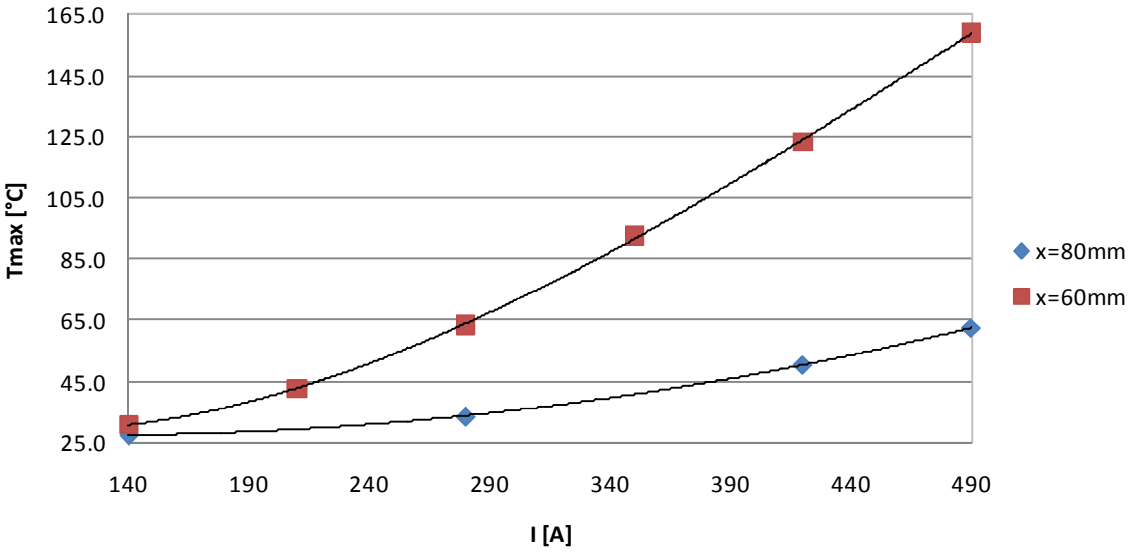

Figure 5-8. Measured maximum temperature of inductively heated steel foil variation with coil current

Then the current was set at 140A and the working distance was varied. The measured temperature is shown in Figure 5-9:

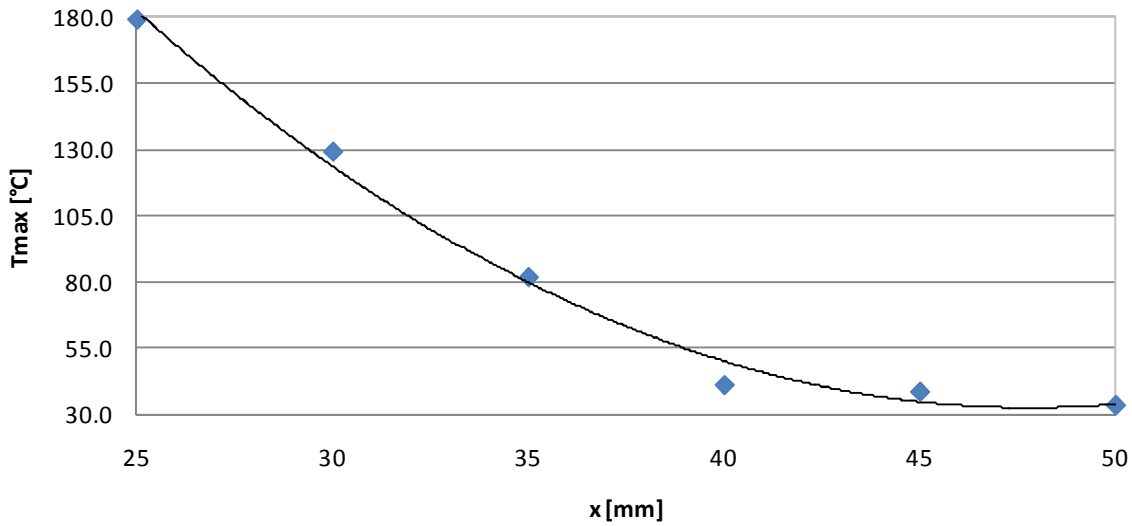

Figure 5-9. Measured maximum temperature of inductively heated steel foil variation with distance to coil

Again a similar behaviour could be observed as in the simulations shown in Figure 5-5.

With the current set at 280A and a working distance of 40mm the maximum temperature was measured against the heating time. As shown in Figure 5-10, a linear behaviour could be observed.

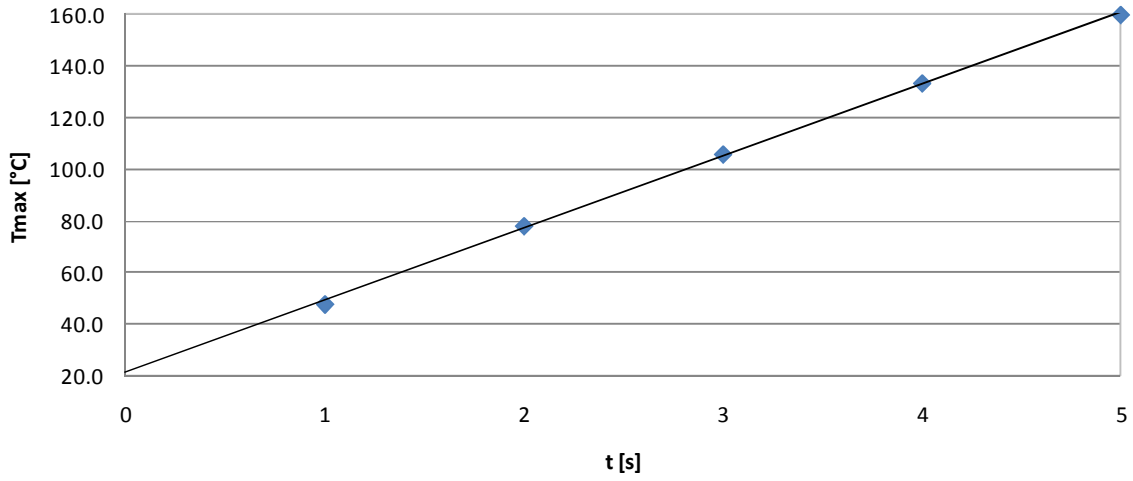

Figure 5-10. Variation of temperature with heating time (steel)

The graph has a slope of 28℃ per second which is c lose to the slope of 25℃ per second from simulation (Figure 5-6).

The experiments were repeated with a nickel foil of dimensions 25mm x 25mm x 7.5µm. While varying the coil current the maximum temperature was measured at working distances of 40, 30 and 20mm. The temperatures measured are a guide only, as the emissivity of steel was accidentally used for the nickel measurements. The results are shown in Figure 5-11:

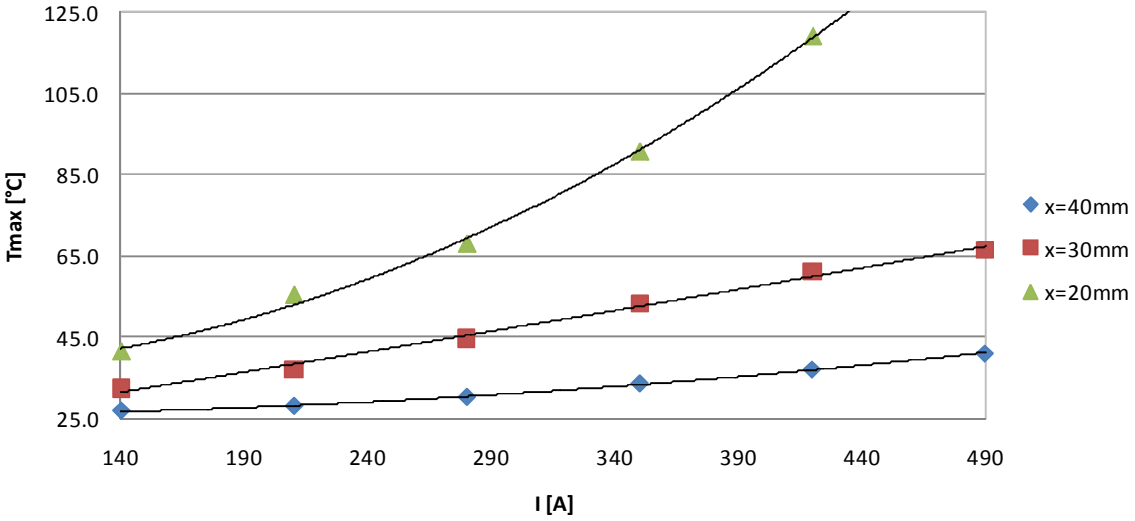

Figure 5-11. Variation of temperature with output current (nickel)

For the distance variation experiment the current was set at 420A. The maximum temperatures measured are shown in Figure 5-12:

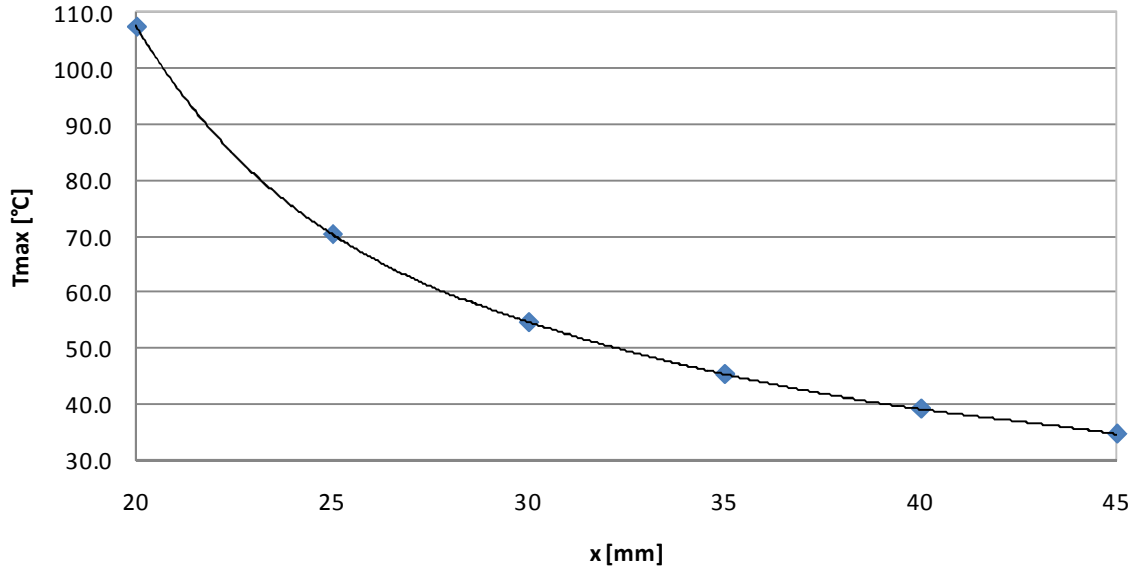

Figure 5-12. Variation of temperature with working distance (nickel)

To investigate the dependency of the heat dissipation in the nickel foil on the heating time an output current of 420A and a working distance of 20mm were used. As expected, a linear dependency with time could be observed (Figure 5-13):

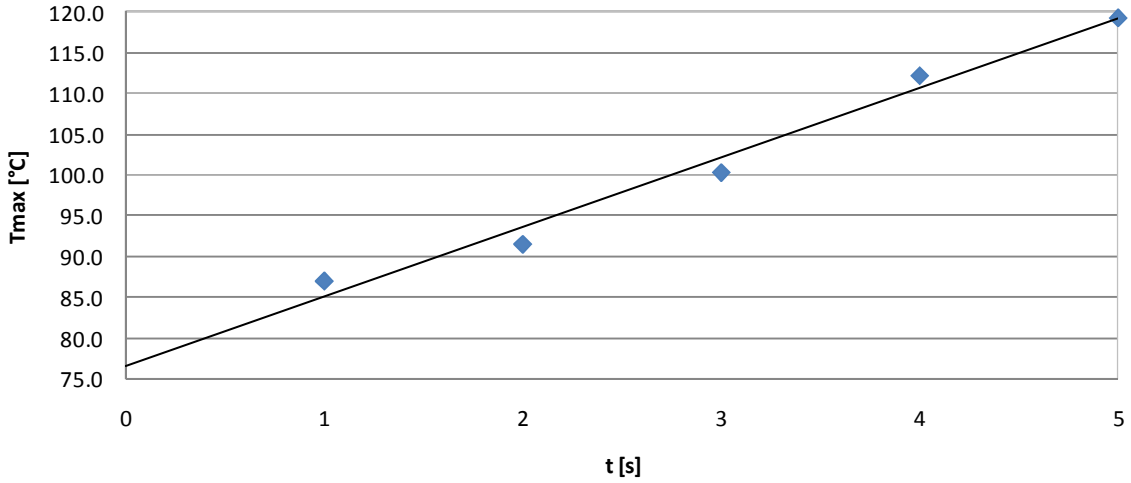

Figure 5-13. Variation of temperature with heating time (nickel)

For the temperature measurements with nickel susceptors the thermal imager was set to the parameters of steel. The emissivity was therefore wrong for nickel and as such so were the measured temperatures. The thermal imager actually measures the radiated power and calculates the temperature by using the Stefan-Boltzmann law. We can say

$$T_m = \left(\frac{P_m}{\varepsilon \cdot \sigma} \right)^{\frac{1}{4}} \qquad (5\text{-}3)$$

Where

T_m:	Calculated temperature of radiator	[K]
P_m:	Measured power of radiated heat	[W]
ε:	Emissivity	unitless
σ :	Stefan-Boltzmann constant	[W/(m^{2}K^4)]

To get the corrected temperatures T_C the measured temperatures T_m shown in Figure 5-11 to Figure 5-13 were multiplied by the fourth root of the emissivity of steel and divided by the fourth root of the emissivity of nickel:

$$T_C = T_M \frac{\varepsilon_{steel}^{\frac{1}{4}}}{\varepsilon_{nickel}^{\frac{1}{4}}} \qquad (5\text{-}4)$$

It has to be considered that the unit of the temperature in the Stefan-Boltzmann law is Kelvin. The emissivity of steel used during measurements was 0.28, the emissivity of nickel varies from 0.045 for commercially pure polished nickel to 0.37 for oxidized nickel. The corrected temperatures calculated as outlined above are shown in Figure 5-14:

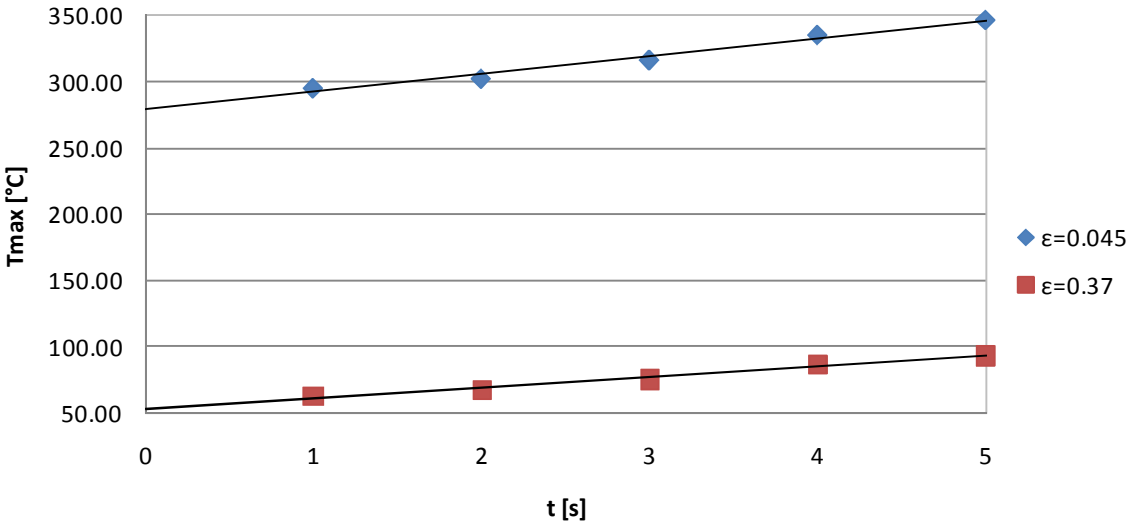

Figure 5-14. Variation of temperature with heating time (nickel) with corrected emissivities

A linear dependency of heating rate on time was observed in Figure 5-14. However, the trendlines should intersect the y-axis at room temperature but the intersections are at around 476℃ (for ε = 0.045) and 58℃ (for ε = 0.37). The numeric models ignored the temperature dependency of the susceptor's resistivity but, as shown later in Section *5.3 Change of Resistivity*, this effect damps the heating rate significantly. As the temperature measurements started

after one second of heating the relationship between heating time and generated temperature only appears to be linear.

It was concluded that the same qualitative behaviour is shown in the experiments with foil susceptors as in the simulations. A further analysis of the functional form of the experimentally observed dependencies is presented in Section *5.2.3 Validation of the Analytical Model*.

5.2 Derivation of Analytical Model

In the literature concerning induction heating the relationships between heating rate and different process parameters are mentioned [41; 76; 78; 81; 84; 87; 89], but a derivation of an analytical model covering all the relationships is missing. To be able to understand cross-parameters dependencies such a model is necessary. An analytical equation is easier to understand and needs less time for calculations than a numeric model. Hence it is potentially a useful approach for process optimisation when using induction heating for polymer bonding.

The work reported in the previous section confirmed that the basic physics describing how different parameters affect the heat dissipation have been identified. A more detailed model could therefore be derived by combining the equations in Section *5.1 Basic Physical Equations*. However, electromagnetic heating is a very complex process and the amount of heat generated in the workpiece depends on more parameters than have been explored in the previous section. The resistivity of the susceptor changes with temperature and its relative permeability with the strength of the magnetic field. The strength of the magnetic field outside the coil is not homogenous and is also affected by many parameters, such as susceptor design, position of the workpiece in the field, and other susceptors (e.g. the workbench) within its range. Shape, design and purity of the susceptor affect the flow of eddy currents and different cooling effects such as heat conduction and radiation apply as well. These factors are

not taken into account in the derivation and hence the model can only be an approximation to predict the applicability and the behaviour of a susceptor.

5.2.1 Model Construction

For analytical modelling of the induction heating process certain design parameters had to be assumed. The workpiece was chosen to be a ring placed in the magnetic field of a single loop inductor, coaxial with the inductor as shown in Figure 5-15:

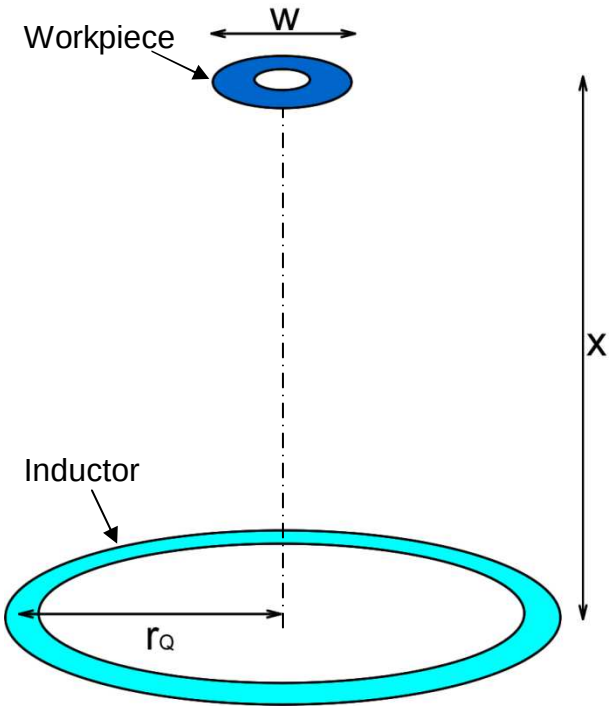

Figure 5-15. Assumptions for analytical approach

The Biot-Savart Law describes the magnetic flux density generated by a coil on any point on the coil's main axis with a distance x to the coil's plane. On either side of the axis the distribution of magnetic flux density increases, having a maximum around the conductor [91]. The workpiece in the model was not a point, but a body with finite size, therefore the flux density varied over the width of the body.

To reduce error the following assumptions were required:

- The width w of the workpiece had to be much smaller than the radius r_Q of the inductor;
- The radius r_Q of the inductor had to be smaller than the distance x between inductor and workpiece;
- The thickness of the workpiece had to be smaller than the penetration depth.

Also, it was assumed that all parameters, except for the resistivity of the workpiece, were not dependent on temperature and magnetic field strength. This assumption is justified by the comparison with experiments reported below. However the percentage change in resistivity would probably have the largest effect of the temperature dependant parameters (~117% over a range of 300℃). By contrast the change of the workpiece's width is likely to be only a few percent over the same temperature range.

5.2.2 Derivation of the Analytical Model

The power dissipated in a conductor is described with Joule's law (see equation 2-3). The equation for the quantity of heat delivered into the susceptor is

$$Q = P \cdot t \qquad (5\text{-}5)$$

Where

Q:	Heat quantity	[J]
P:	Power	[W]
t:	Time	[s]

Thus the change of temperature can be described using the induced current and heating time as shown in equation 5-6:

$$\Delta T = \frac{Q}{Cp \cdot m} = \frac{R \cdot I_{ind}^2 \cdot t}{Cp \cdot m} = \frac{\rho \cdot \frac{l}{A} \cdot I_{ind}^2 \cdot t}{Cp \cdot m} \qquad (5\text{-}6)$$

Where

ΔT:	Change of temperature	[K]
R:	Resistance of conductor	[Ω]
Cp:	Heat capacity of conductor	[J/(kgK)]
m:	Mass of conductor	[kg]
ρ:	Resistivity	[Ωm]
l:	Length of conductor	[m]
A:	Cross-sectional area of conductor	[m^2]

For a given geometry the only unknown in equation 5-6 is I_{ind}. As the resistance of the conductor is known, I_{ind} can be replaced if the voltage generated in the coil U_{ind} is known.

The voltage induced in a coil can be calculated with

$$U_{ind} = -N \frac{d\phi}{dt} \qquad (5\text{-}7)$$

Where

U_{ind}:	Induced voltage	[V]
N:	Number of windings (secondary) coil	unitless
Φ:	magnetic flux through a single winding	[Vs]
t:	time	[s]

Using the equation for the magnetic flux Φ

$$\phi = \mu \cdot H \cdot A_a \qquad (5\text{-}8)$$ with the relationship between H and magnetic flux density B

$$B = \mu \cdot H \qquad \text{(5-9), where}$$

$$\mu = \mu_0 \cdot \mu_r \qquad \text{(5-10), and}$$

$$\mu_r = \frac{B}{B_0} \qquad \text{(5-11)}$$

Where

μ:	Permeability	[Vs/(Am)]
H:	Magnetic field intensity	[A/m]
A_a:	"Active" area (threaded by magnetic field)	[m^2]
μ_0:	Magnetic field constant	[Vs/(Am)]
μ_r:	Relative permeability	unitless
B:	Magnetic flux density in the conductor	[Vs/m^2]
B_0:	Magnetic flux density in vacuum	[Vs/m^2]

equation 5-7 yields an expression for U_{ind} as follows:

$$U_{ind} = -N \frac{dB}{dt} \cdot A_a \cdot \cos(\vec{B}, \overrightarrow{A_a}) \qquad \text{(5-12)}$$

As mentioned in Section *5.1 Basic Physical Equations* the magnetic flux density generated by a coil/loop is described in the Biot-Savart law (see Figure 5-1, equation 5-1).

From (5-10), (5-11), and (5-12) it follows that:

$$U_{ind} = -N \cdot n \cdot \frac{dI}{dt} \cdot \frac{\mu_0 \cdot \mu_r}{2} \cdot \frac{r_Q^2}{\left(r_Q^2 + x^2\right)^{\frac{3}{2}}} \cdot A_a \cdot \cos(\vec{B}, \overrightarrow{A_a}) \qquad \text{(5-13)}$$

Using this relationship in equation 5-6 the change of temperature can be expressed in terms of known parameters:

$$\Delta T = \frac{U_{ind}^2 \cdot t}{\rho \cdot \frac{l}{A} \cdot Cp \cdot m} = \frac{\left\{ N \cdot n \cdot \frac{dI}{dt} \cdot \frac{\mu_0 \cdot \mu_r}{2} \cdot \frac{r_Q^2}{\left(r_Q^2 + x^2\right)^{\frac{3}{2}}} \cdot A_a \cdot \cos(\vec{B}, \overrightarrow{A_a}) \right\}^2 \cdot t}{\rho \cdot \frac{l}{A} \cdot Cp \cdot m} \quad (5\text{-}14)$$

Assuming the number of windings of coil and workpiece is one (N = n = 1) and the vector of the magnetic flux density B is perpendicular to the active area A_a a simplified equation can be obtained:

$$\Delta T = \frac{\left\{ \frac{dI}{dt} \cdot \frac{\mu_0 \cdot \mu_r}{2} \cdot \frac{r_Q^2}{\left(r_Q^2 + x^2\right)^{\frac{3}{2}}} \cdot A_a \right\}^2 \cdot t}{\rho \cdot \frac{l}{A} \cdot Cp \cdot m} \quad (5\text{-}15)$$

There remains the problem of defining the rate of change of the induction current. The generator's output current switches from the positive value of the set current to the negative value and back in a given time, which depends on the frequency f. Using the equation for current in sinusoidal waveform

$$I = I_0 \cdot \sin(\omega t) \quad (5\text{-}16)$$

The change of current can be described as

$$\frac{dI}{dt} = I_0 \cdot \omega \cdot \cos(\omega t) \quad (5\text{-}17)$$

In equation 5-15 we can use the average

$$\left\langle \left(\frac{dI}{dt} \right)^2 \right\rangle = I_0^2 \cdot \omega^2 \cdot \left\langle \cos^2(\omega t) \right\rangle \quad (5\text{-}18)$$

Let $\theta = \omega t$:

$$\left\langle \cos^2(\omega t) \right\rangle = \frac{1}{2\pi} \int_0^{2\pi} \cos^2 \theta = \frac{1}{2} \tag{5-19}$$

it follows that:

$$\left\langle \left(\frac{dI}{dt} \right)^2 \right\rangle = \frac{1}{2} \cdot I_0^2 \cdot \omega^2 = 2 \cdot \pi^2 \cdot I_0^2 \cdot f^2 \tag{5-20}$$

Using equation 5-20 in 5-15:

$$\Delta T = \frac{\pi^2 \cdot I_0^2 \cdot f^2 \cdot \mu_0^2 \cdot \mu_r^2 \cdot A_a^2 \cdot t \cdot r_Q^4 \cdot A}{2 \cdot \rho \cdot l \cdot Cp \cdot m \cdot \left(r_Q^2 + x^2 \right)^3} \tag{5-21}$$

As mentioned above in Section *2.2.2.3 Hysteresis Heating* for ferromagnetic materials a heating effect by hysteresis loss occurs as well. This effect is only a minor producer of heat, hence it can be ignored [89].

5.2.3 Validation of the Analytical Model

To validate equation 5-21 the functional dependence of temperature rise on heating time, working distance and output current was compared with that observed for steel foils in earlier experiments (see Section *5.1.2 Experimental Validation*). The nickel foil data was not used because of the error in the emissivity setting on the thermal imager when it was measured (see Section *5.1.2 Experimental Validation*).

Assuming no other parameter is affected when heating time, working distance or output current are varied individually, simplified relations between change of temperature and the varied parameter can be derived from equation 5-21.

If heating time is varied while all other parameters are constant the following relation can be derived:

$$\Delta T = X \cdot t \qquad (5\text{-}22)$$

$$\log(\Delta T) = \log(X) + \log(t) \qquad (5\text{-}23)$$

where X replaces all the constant parameters. Thus plotting log(ΔT) of the temperature measured in preceding experiments (see Section *5.1.2 Experimental Validation*) against log(t) should yield a slope of 1. As shown in Figure 5-16 this was the case with a 95% confidence interval of 0.89 to 1.11 (see equation 5-25 below):

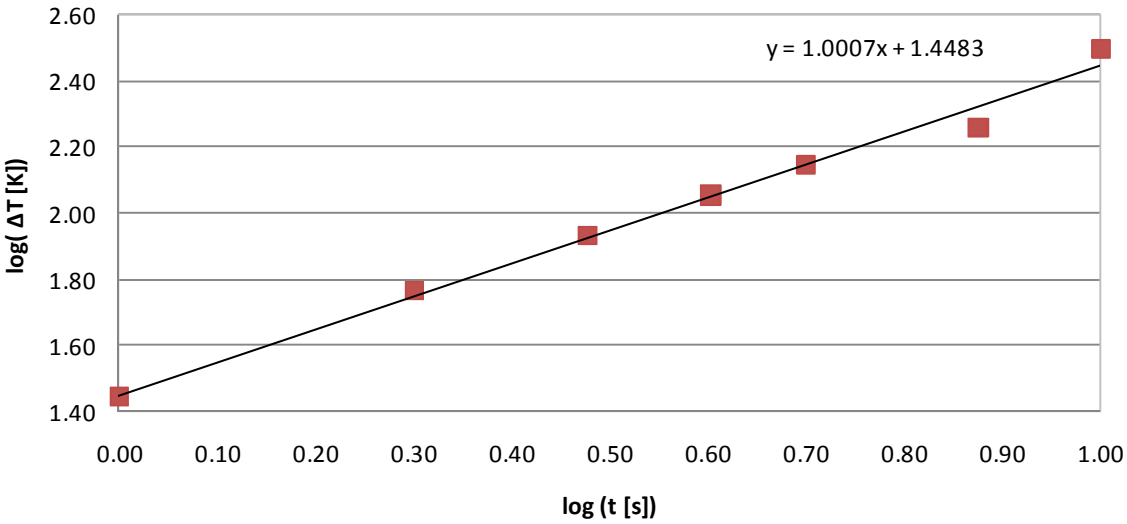

Figure 5-16. Measured change of temperature against heating time

The relation between change of temperature and working distance is more complex. According to equation 5-21 ΔT should be constant for x << r_Q and proportional to x^{-6} for x >> r_Q. Hence, the slope of the trendline should have a value between 0 and -6 when log(ΔT) is plotted against log(x) for the range of x assessed experimentally, and for the same order of the coil radius.

As shown in Figure 5-17 the trendline had a slope of about -4 (95% confidence interval of -4.99 to -2.73):

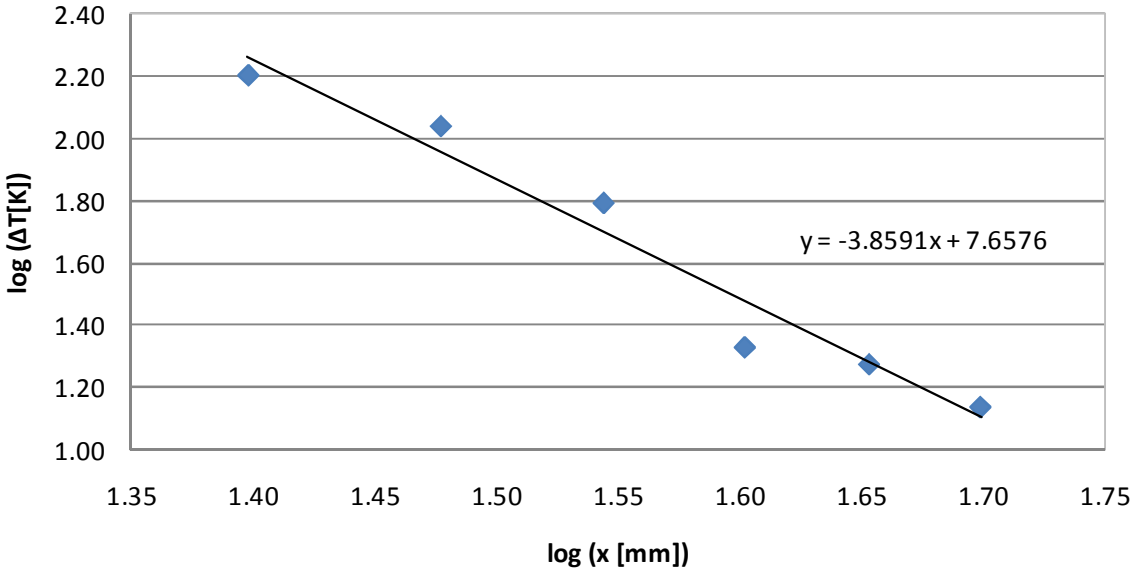

Figure 5-17. Measured change of temperature against working distance

In a final step the relation between output current and change of temperature was derived.

$$\Delta T = X \cdot I^2 \qquad (5\text{-}24)$$

$$\log(\Delta T) = \log(X) + 2 \cdot \log(I) \qquad (5\text{-}25)$$

Where again X replaces all the constant parameters. According to equation 5-25 a plot of log(ΔT) vs. log(I) should have a slope of 2. Figure 5-18 shows the plot for the data in Section *5.1.2 Experimental Validation* from two experiments at different working distances:

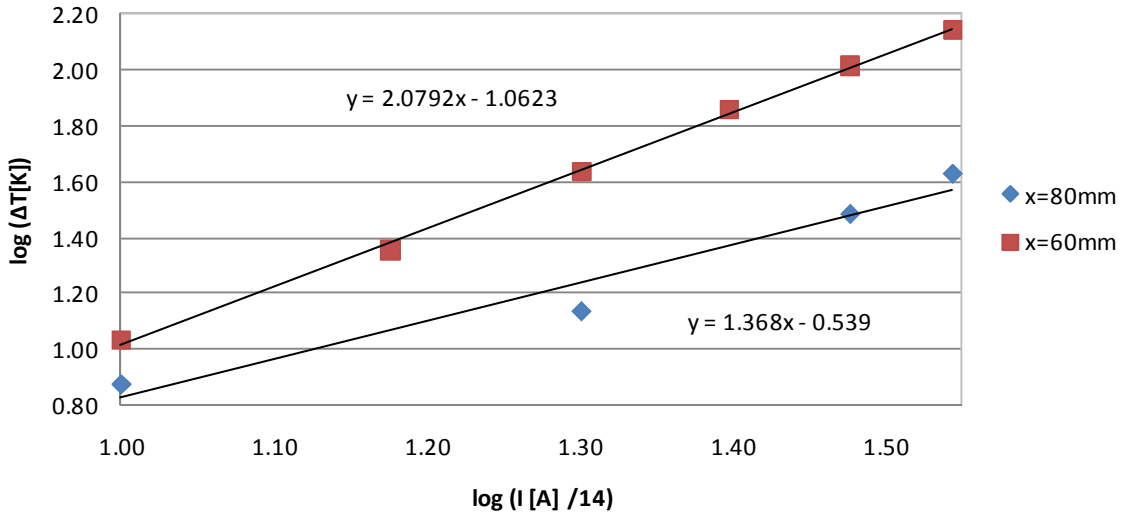

Figure 5-18. Measured change of temperature against output current

The graph for the temperatures generated at a working distance of 60mm shows the expected slope of 2 while the temperatures generated at a working distance of 80mm did not show the expected behaviour. This is likely due to the smaller number of readings made at the 80mm distance as demonstrated below.

Usually the standard deviation σ gives an idea of how accurate a calculated slope b of a trendline is. However, if the number of measurements is small a 95% confidence interval should be applied. Using the t distribution, the uncertainty in the slope can be quantified:

$$\beta = b \pm t_{95\%,\nu} \cdot \sigma_b \qquad (5\text{-}26)$$

Where

β: Confidence interval of slope b

b: Slope of trendline

$t_{95\%,\nu}$: Critical t value at 95% confidence level

σ_b: Standard deviation in b

For the experiments at 80mm working distance there were only 4 data points that led to a high critical t value of 4.303. With a standard deviation σ_b of 0.22

an error of ±0.93 was calculated. Hence, the slope could vary between 0.61 and 2.47. At a working distance of 60mm more data points where recorded. Thus, the critical t value was smaller with 2.776. The error for the slope was calculated to be 0.14 giving a 95% confidence interval of 1.94 to 2.22.

From these results the system does react as predicted by the analytical equation.

5.3 Change of Resistivity

In this section equation 5-21 is extended to examine the effects of including the temperature dependence of resistivity. To calculate the change in resistivity ρ with temperature the temperature coefficient α is used:

$$\rho_{(T)} = \rho_{ref}\,(1+\alpha(T-T_{ref})) = \rho_{ref}\,(1+\alpha\cdot\Delta T) \qquad (5\text{-}27)$$

Where

α:	Temperature coefficient	[1/K]
ρ_{ref}:	Resistivity at reference temperature	[Ωm]
T:	Temperature	[K]
T_{ref}:	Reference temperature	[K]

For the calculation equation 5-21 must be re-cast as a differential equation as follows:

$$\frac{d\Delta T}{dt} = \frac{k}{\rho_{(\Delta T)}} \qquad (5\text{-}28)$$

With $k = \dfrac{\pi^2\cdot I_0^2\cdot f^2\cdot\mu_0^2\cdot\mu_r^2\cdot A_a^2\cdot r_Q^4\cdot A}{2\cdot l\cdot Cp\cdot m\cdot\left(r_Q^2+x^2\right)^3}$ (5-29)

To solve equation 5-28 it has to be integrated over temperature and time:

$$\frac{d\Delta T}{dt} = \frac{k}{\rho_{ref}}\left(1+\alpha\cdot\Delta T\right)^{-1} \tag{5-30}$$

$$\int_0^{\Delta T}\left(1+\alpha\cdot\Delta T\right)d\Delta T = \int_o^t \frac{k}{\rho_{ref}}\,dt \tag{5-31}$$

$$\left[\Delta T + \frac{\alpha}{2}\cdot\Delta T^2\right]_0^{\Delta T} = \frac{k\cdot t}{\rho_{ref}} \tag{5-32}$$

$$\Delta T + \frac{\alpha}{2}\cdot\Delta T^2 = \frac{k\cdot t}{\rho_{ref}} \tag{5-33}$$

$$\frac{\alpha}{2}\cdot\Delta T^2 + \Delta T - \frac{k\cdot t}{\rho_{ref}} = 0 \tag{5-34}$$

$$\Delta T = \frac{-1\pm\sqrt{1-4\cdot\frac{\alpha}{2}\cdot\frac{-k\cdot t}{\rho_{ref}}}}{\alpha} = \frac{-1\pm\sqrt{1+2\cdot\alpha\cdot\frac{k\cdot t}{\rho_{ref}}}}{\alpha} \tag{5-35}$$

The physical solution to 5-35 is:

$$\Delta T = \frac{-1+\sqrt{1+\alpha\cdot\frac{\pi^2\cdot I_0^2\cdot f^2\cdot\mu_0^2\cdot\mu_r^2\cdot A_a^2\cdot r_Q^4\cdot A\cdot t}{\rho_{ref}\cdot l\cdot Cp\cdot m\cdot\left(r_Q^2+x^2\right)^3}}}{\alpha} \tag{5-36}$$

To compare the calculated heating rate with and without change of resistivity the following parameters were used, which represent the experimental setup in Section *6.1.5 Shape effects* (7.5µm thick nickel ring of 5.5mm outer diameter and 4.5mm inner diameter situated 25mm above a single turn coil of diameter 40mm):

Table 5-1. Parameters – Analytical Approach

Output current	I	[A]	210
Frequency	f	[Hz]	220000
Radius of loop (inductor coil)	r_Q	[m]	0.04
Distance conductor - loop	x	[m]	0.025
“Active” area	Aa	[m^2]	9.50e-05
Length of conductor	l	[m]	0.0314
Cross-sectional area of conductor	A	[m^2]	7.50e-09
Mass of conductor	m	[kg]	2.10e-6
Heat capacity of conductor	Cp	[J/(kg*K)]	444
Resistivity of conductor	ρ	[Ωm]	6.85e-08
Density of conductor	ρ	[kg/m^3]	8908
Magnetic field constant	μ_0	[Vs/Am]	1.26e-06
Temperature coefficient	α	[1/K]	0.0067
Relative permeability	μ_r	unitless	1

The relative permeability μ_r was identified to not having a significant influence on the heating of thin susceptors as reported later in Section *6.1.4 Permeability*. Hence its value was set to 1.

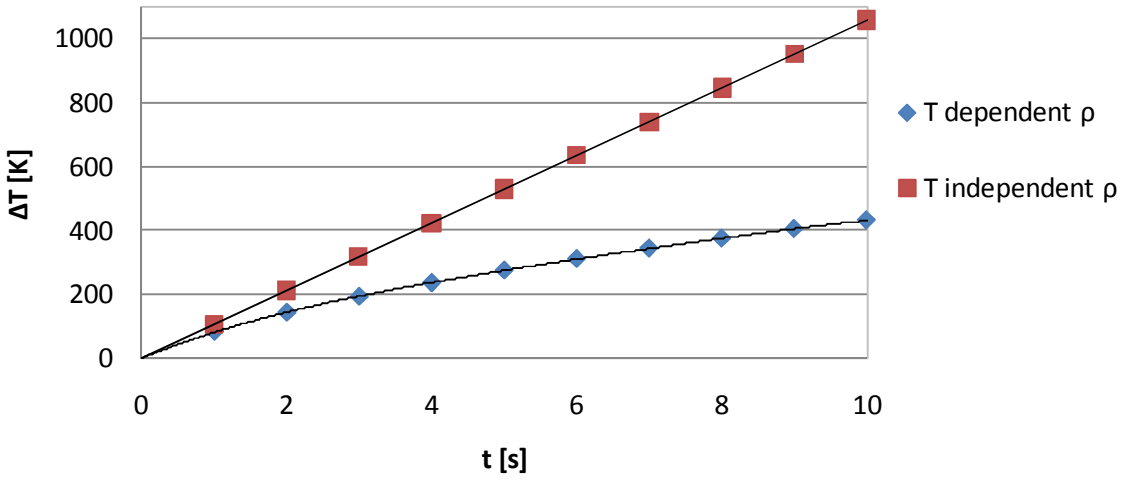

Figure 5-19. Calculated temperature change with and without change of resistivity

The calculated temperatures with and without change of resistivity were plotted over time, as shown in Figure 5-19. A significant damping effect due to inclusion of temperature dependence of resistivity may be observed. Temperature dependency of resistivity was ignored in the numeric models used in Section *5.1.1 Simulation Results*. This explains the observed linear dependency between generated heat and heating time. In Section *5.1.2 Experimental Validation* a linear dependency between these parameters was also inferred from experimental observations. As already pointed out in that section, this can be explained by a relatively small number of measurement points with temperature measurements starting after 1s.

The magnitudes of the temperatures in Figure 5-19 are much higher than those experimentally observed. A correction factor is introduced in Section *5.6 Predicting the Temperatures* to take account of this.

To summarise, equations 5-21 and 5-36 are of use in describing the dependence of temperature on the process parameters rather than predicting real temperatures. The simpler equation 5-21 seems to describe experimental observations well. It can be used to estimate the effect of most of the parameters on the heating rate but it ignores temperature dependency of resistivity. As this dependency was shown to lead to significant damping, it is recommended to use equation 5-36 where possible, especially when considering heating time as variable.

5.4 Effect of Resistivity on Heating Rate

Equation 2-3 may lead to the conclusion that higher resistivity of the susceptor material leads to higher heat generation for a given coil current. But as the current flowing in a workpiece is a result of the induced voltage, its value depends on the resistivity. Hence the amount of heat generated in the workpiece is actually inversely proportional to the resistivity, as shown in equations 5-21 and 5-36. The dependence of current on resistivity was studied using the COMSOL model from Section *5.1.1 Simulation Results* as it was easier to vary the resistivity systematically in software.

All parameters were kept constant while the resistivity of the workpiece was altered. The dimensions of the workpiece were in the range of the penetration depth to guarantee a homogeneous current distribution. Both current density and generated heat were simulated. The current density variation with resistivity is shown in Figure 5-20:

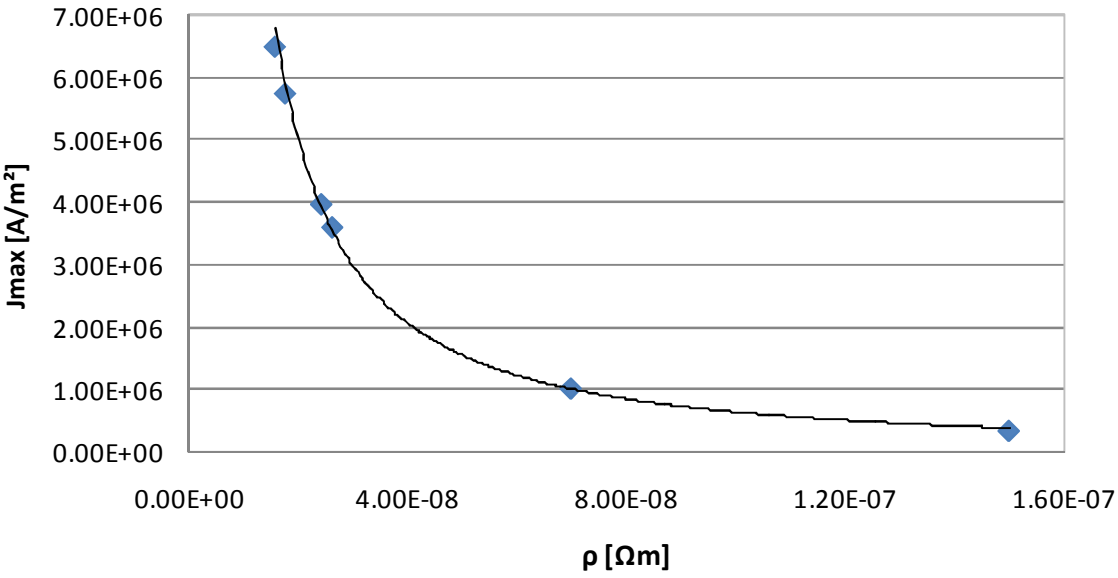

Figure 5-20. Maximum workpiece current density against resistivity from COMSOL simulation

As expected the temperature change showed similar behaviour against resistivity as shown in Figure 5-21 (the line is a guide to the eye):

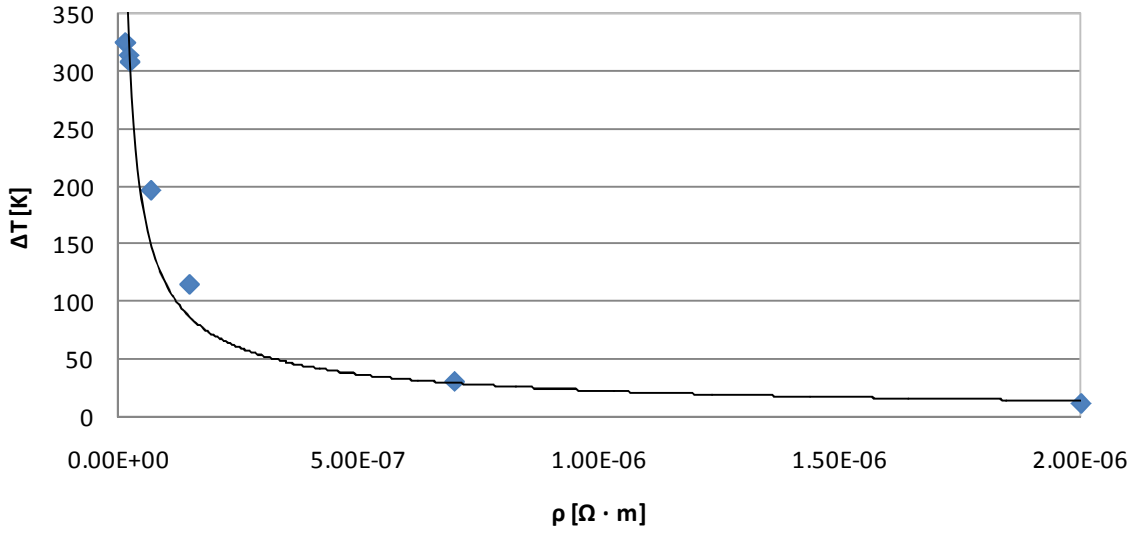

Figure 5-21. Change of temperature against resistivity from COMSOL simulation

Thus the higher the conductivity of a material the better it works as a susceptor for induction heating.

5.5 Cooling Effects

A second major effect not covered by equation 5-21 is cooling. During induction heating the workpiece is not only heated but cooling effects occur as well. Cooling will determine an equilibrium temperature at which the cooling power equals the heating power. Ignoring other effects like phase changes (e.g. when the susceptor starts to melt) the temperature at equilibrium is the expected maximum achievable for a particular setup. Three main cooling effects have to be considered.

If a solid body is surrounded by or has contact with a liquid or gaseous medium of a different temperature, heat is transferred from the warmer to the cooler element. This effect is referred to as heat convection. Equation 5-37 describes the calculation of the rate of transferred heat:

$$P_{ht} = \alpha_{ht} \cdot A_{ht} \cdot (T_S - T_M) \qquad (5\text{-}37)$$

Where

P_{ht}:	Power of transferred heat	[W]
α_{ht}:	Heat transfer coefficient	[W/(Km^2)]
A_{ht}:	Contact area	[m^2]
T_S:	Temperature solid	[K]
T_M:	Temperature medium	[K]

Another effect is heat conduction. If there are different temperatures within a solid a heat flux from the warmer to the cooler area sets in, as shown in Figure 5-22, to restore heat equilibrium.

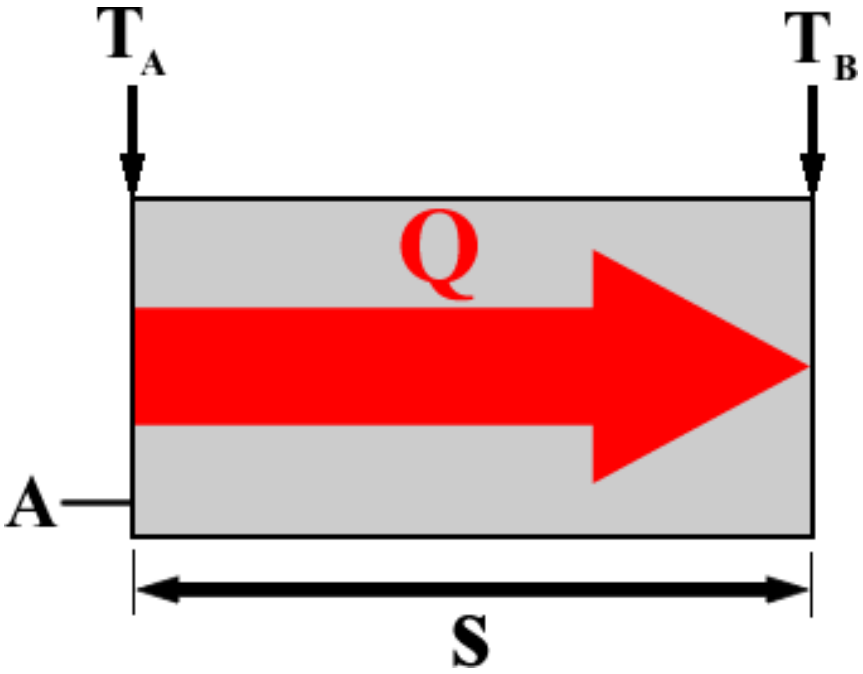

Figure 5-22. Schematic of heat conduction Q

In the joining application the plastic substrate works as a heat conductor transporting heat away from the interface between substrate and susceptor. The power of conducted heat can be calculated using equation 5-38:

$$P_{hc} = \lambda \cdot \frac{A_{hc}}{s_{hc}} \cdot (T_A - T_B) \qquad \text{, with } T_A > T_B \qquad (5\text{-}38)$$

Where

P_{hc}:	Power of conducted heat	[W]
λ:	Coefficient of thermal conductivity	[W/(Km)]
A_{hc}:	Cross-sectional area of heat conductor	[m^2]
S_{hc}:	Length of heat conductor	[m]
T_A, T_B:	Temperatures	[K]

The third effect to be considered is heat radiation. While radiating heat a body cools down. The power of radiated energy can be calculated with the Stefan-Boltzmann law for grey bodies:

$$P_{hr} = \varepsilon_{(T)} \cdot \sigma \cdot A_{hr} \cdot T_a^{\,4} \qquad (5\text{-}39)$$

Where

P_{hr}:	Power of radiated heat	[W]
$\varepsilon_{(T)}$:	Emissivity	unitless
σ :	Stefan-Boltzmann constant	[$W/(m^2K^4)$]
A_{hr}:	Surface area of radiator	[m^2]
T_a:	Absolute temperature of radiator	[K]

In the experiments and models described in this chapter the susceptor is supported in air and not attached to a substrate. Hence, the cooling by heat conduction can be assumed to be negligible.

The heating power by induction can be described as

$$P_h = \frac{\pi^2 \cdot I^2 \cdot f^2 \cdot \mu_0^2 \cdot \mu_r^2 \cdot A_a^2 \cdot r_Q^4 \cdot A}{2 \cdot \rho_{ref} \cdot (1 + \alpha \cdot \Delta T) \cdot l \cdot \left(r_Q^2 + x^2\right)^3} \qquad (5\text{-}40)$$

In Figure 5-23 the sum of equations 5-37 and 5-39 are plotted together with the heating power calculated using equation 5-40, for the parameters in Table 5-1 and assuming an emissivity of 0.37 (for oxidised nickel). It can be seen that power balance is reached at a temperature change of 410K (see Figure 5-23).

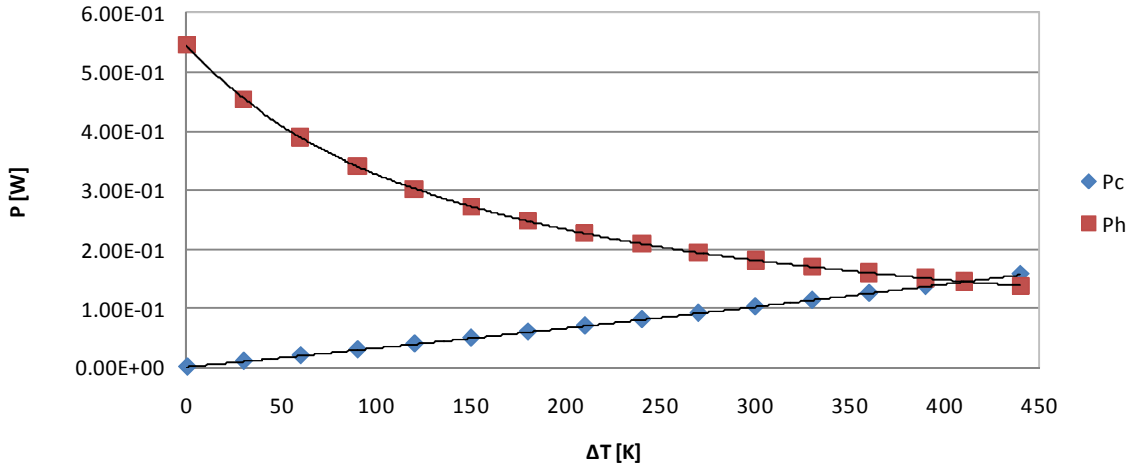

Figure 5-23. Calculated balance of heating and cooling power in air

As mentioned before this calculation ignores changes in material properties depending on temperature (except change of resistivity).

A better model of the situation during bonding, when the susceptor is surrounded by plastic so there is no air-cooling, is to consider conduction cooling. If we calculate heat flow in an ideal situation where there is no thermal barrier between susceptor and surrounding material, and where the outer surface of the plastic is kept at ambient temperature, we find the power magnitude of cooling by conduction can be less (for thick plastic sheets) or more (for thin plastic sheets) than by convection. In Figure 5-24 the calculations of heating and cooling power of a nickel ring encapsulated in 2mm and 20mm PMMA are shown.

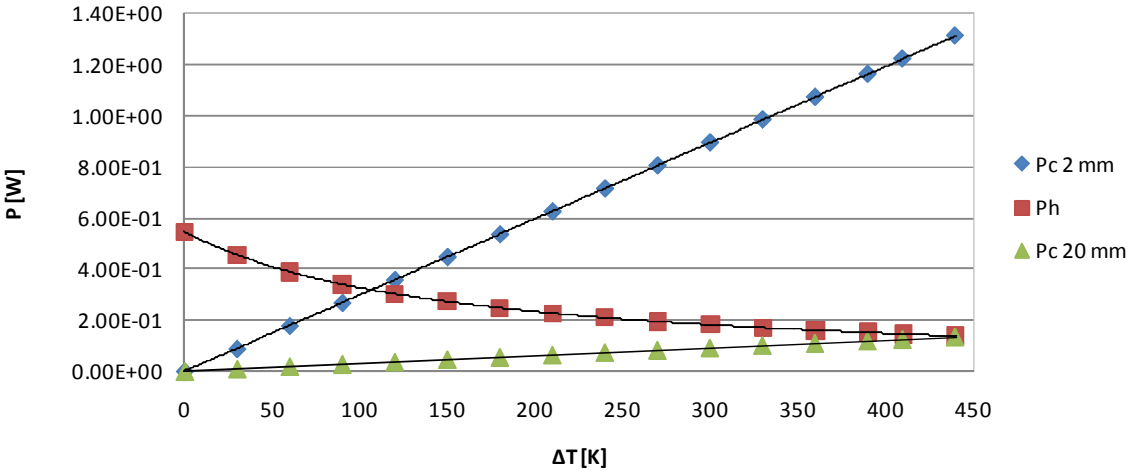

Figure 5-24. Calculated balance of heating and cooling power - susceptor encapsulated in 2mm and 20mm PMMA

As a simplification the heat flux in the PMMA was assumed to be perpendicular to the susceptor surface. With 2mm PMMA equilibrium is reached at a change of temperature of around 100K, with 20mm PMMA it is at 440K.

In the experiments there is no ideal situation. Small air gaps at the susceptor form a thermal barrier and the air surrounding the setup heats as well. Hence the cooling power can be assumed to be less than shown in Figure 5-24, but it was shown that cooling effects might influence the process by damping the heating rate. However, equation 5-36 seems to sufficiently describe the induction heating process, at least for generated temperatures around 200K, where the polymer bonding processes take place and can be useful for process design and control.

5.6 Predicting the Temperatures

As mentioned earlier, it is unlikely to be possible to calculate or simulate the exact temperature generated by induction heating. However, as the analytical equation sufficiently describes the functional dependencies it should be usable for predicting the magnitudes of the generated temperatures despite the mismatch between the predictions of the equation and experimental observations reported in Section *5.3 Change of Resistivity*.

An attempt was also made to take account of the fact that in the experiments a flat helix coil with five windings was used instead of a single loop as in the model. For a cylindrical coil the magnetic flux density is a product of the number of windings. To identify how the number of windings affects the magnetic flux a model was designed using COMSOL Multiphysics. The helix coil was modelled as a set of five different inductors with constant radii: 40mm, 30mm, 20mm, 10mm and 1mm, respectively. The current in every inductor was set to be 500A. Then five different simulations were run: first, only the outer inductor was used; in the second simulation the second inductor was added, and so on until all five windings were used. In each simulation the magnetic flux density was measured on the coil's centre line at a distance of 40mm:

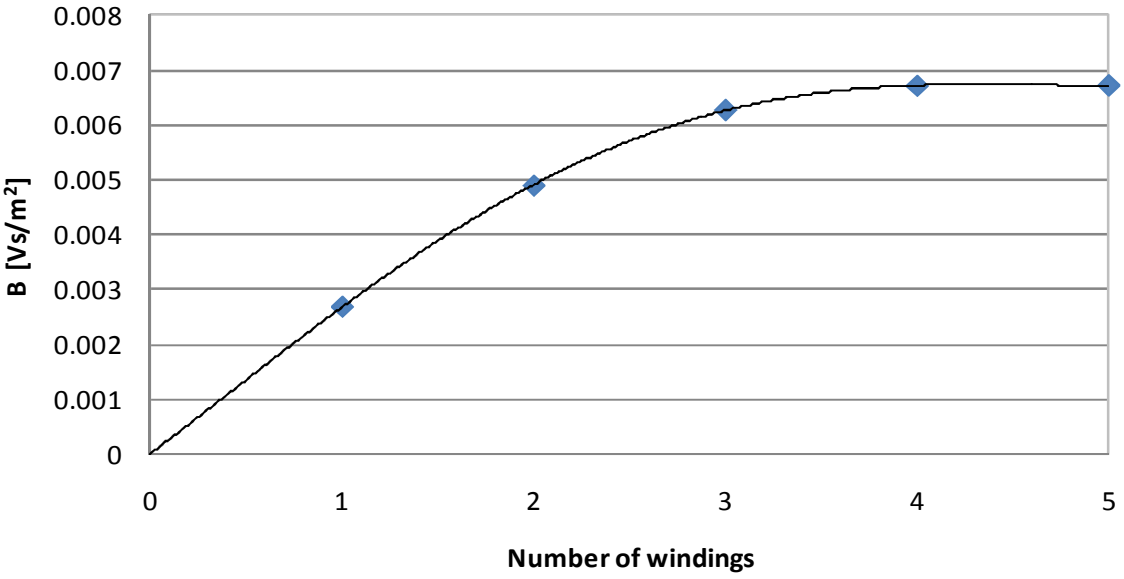

Figure 5-25. Magnetic flux density against number of windings from COMSOL simulation

According to Figure 5-25 the smaller windings hardly contribute to the magnetic flux density. The decision was made to only consider the outer winding in the analytical model. All other parameters were chosen according Table 5-1. As the permeability μ_r seems to be unimportant for thin susceptors (see Section *6.1.4 Permeability*) it was set to one.

In Figure 5-26 predicted temperatures calculated are plotted versus time, together with experimental data from Section *6.1.5 Shape effects*:

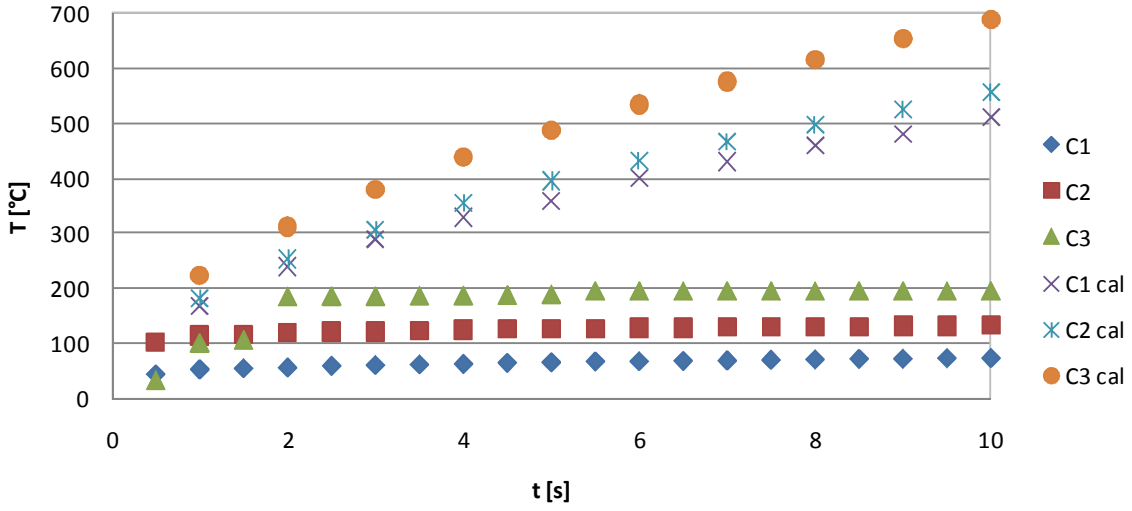

Figure 5-26. Measured and calculated temperatures of circular shaped circuits

The calculated temperatures using equation 5-36 were much higher than the measured ones. The differences between the experimental setup and the assumptions of the analytical approach leading to equation 5-36 do not fully account for the scale of the difference. In the analytical approach the assumption was made that the inductor is a thin line. As mentioned above (see Section *5.1.1 Simulation Results*) this leads to a magnetic flux density at the workpiece about two times higher than produced by a space filling coil. Also the same effect that leads to limited penetration depth was ignored in the model: the induced currents create a magnetic field counteracting their cause, thus weakening the inductor coil's field. Additionally the coil in the analytical model was taken to be a single loop instead of a multi-turn coil, which again leads to a reduced magnetic flux density with a factor of about 0.4. These factors might

explain the difference between predicted and experimentally observed heating rates.

Cooling effects were ruled out to have greater impact later in Section *6.2 Cooling Effects*, but this conclusion was based on the assumption that the analytical model was correct. But as shown in the previous section, cooling might have a damping effect on the heating rate. This may also explain the lack of fit between the shape of the predicted and experimental temperature rises seen in Figure 5-26.

Thus, although the analytical model provides an insight into the functional dependencies between heating rate and heating parameters, it has proved not possible to use it to reliably predict magnitudes of temperature rise.

6 Effects of Susceptor Design

For a workable process it is critical to manage the heat dissipation. The analytical model derived in Section *5.2 Derivation of Analytical Model* can be used to estimate the behaviour of the heating rate when process parameters are varied. However, the model ignores the effects of susceptor design. In order to understand how susceptor design can be used to optimise the heating process the effects of susceptor area and shape were investigated.

6.1 Susceptor Design

Susceptor design is a key consideration when designing an induction bonded microfluidic device. Yang et al. have already demonstrated that circular shaped susceptors perform better than squared shapes, which again perform better than susceptors with triangular shapes [41], in terms of rapidity of heating. In their work they used filled shapes, which correspond with the use of whole layer susceptors mentioned in Section *7.5.1 Continuous Layer Susceptor*. As the alternative joining concept is to use narrow metal tracks (with polymer to polymer bonds formed at the edges of the tracks) the performance of different closed loop shapes enclosing holes was investigated, as well as the effect of susceptor area.

6.1.1 Numeric Approach

To identify the effect of area changes of the susceptor, simulation software is most suitable, as a large number of susceptor areas and depths can be considered in a short time. Again COMSOL Multiphysics software was used to simulate the generated temperature as a function of the induced current density (see Section 3.4.2 *Coupled Model of Induced Currents, Workpiece Heating & Conductivity Change*).

In the model a thin copper disc was placed 20mm above an inductor. The inductor was a single line loop with a radius of 100mm as shown in Figure 6-1:

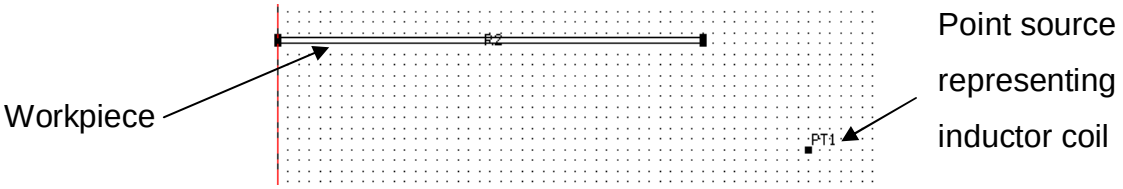

Figure 6-1. Detail of COMSOL model for simulating inductive heating

The thickness of the susceptor was kept constant at 1mm and the radius was varied between 1mm and 80mm. The thickness was much larger than in previous simulations to reduce the processor power needed for larger susceptor radii. As the maximum temperature was measured it was critical to have very homogeneous heat dissipation so the penetration depth was increased by using a very low frequency. This lead to decreased heating, hence output current and heating time had to be high to increase generated temperatures. The output current was set at 2000A with a frequency of 200Hz, heating time was 200s. A summary of the model details can be found in Appendix A6.3 *Modelling Area Effects*.

This setup did not follow the assumptions of the analytical solution in Section *5.2.1 Model* but equations 5-21 and 5-36 should still be usable for predictions of the heating rate dependencies on the susceptor geometry. As the effect of cooling was investigated as well, the decision was made to use equation 5-21 rather than equation 5-36. The latter is too complex to include the equations for cooling (Section *5.5 Cooling Effects*).

When varying the radius r of the susceptor, the active area A_a, the cross-sectional area A and the susceptor's mass m vary as well, the latter being a function of the active area and the thickness. The conductor length l is hard to define where current flow is not constrained to a particular path but the assumption is made that it is linear function of the workpiece's radius. All other

parameters are constant in this experiment. Equation 5-21 can therefore be rewritten as follows:

$$\Delta T = k \cdot \frac{A_a^2 \cdot A}{A_a \cdot l} = k_h \cdot \frac{R^4 \cdot R}{R^2 \cdot R} = k_h \cdot R^2 \qquad (6\text{-}1)$$

with $k = \frac{\pi^2 \cdot I^2 \cdot f^2 \cdot \mu_0^2 \cdot \mu_r^2 \cdot t \cdot r_Q^4}{2 \cdot \rho_{res} \cdot \rho_{dens} \cdot Cp \cdot t_w \cdot \left(r_Q^2 + x^2\right)^3}$, $k_h = \frac{\pi^2 \cdot I^2 \cdot f^2 \cdot \mu_0^2 \cdot \mu_r^2 \cdot t \cdot r_Q^4 \cdot \pi}{2 \cdot \rho_{res} \cdot \rho_{dens} \cdot Cp \cdot \left(r_Q^2 + x^2\right)^3 \cdot x}$

Where

t_w:	Thickness of susceptor	[m]
x:	Functional factor of conductor length	unitless

As mentioned before (see Section *5.5 Cooling Effects*) cooling effects might damp the heating rate when large area susceptors are used. An attempt to estimate the magnitude of the effect of cooling for smaller active area susceptors is made here. As a simplification it is assumed that for thin workpieces the cooling power is a temperature independent function of active area A_a and a cooling constant k_c. The relationship of change of temperature and workpiece radius now is

$$\Delta T = k' \cdot (k_h' \cdot R^2 - k_c) \qquad (6\text{-}2)$$

with $k' = \frac{t}{Cp \cdot \rho_{dens} \cdot t_w}$, $k_h' = \frac{\pi^2 \cdot I^2 \cdot f^2 \cdot \mu_0^2 \cdot \mu_r^2 \cdot r_Q^4 \cdot \pi \cdot t_w}{2 \cdot \rho_{res} \cdot \left(r_Q^2 + x^2\right)^3 \cdot x}$

Thus for small radii or very thin susceptors the cooling constant might have an impact. For greater radii equation 6-1 seems to be appropriate to describe the change of temperature.

A second simulation was undertaken to identify how much the susceptor's permeability affects the heating rate. Materials with a relative permeability greater than 1 concentrate the magnetic field lines leading to a higher flux density. However for very thin susceptors the majority of flux lines thread free space so it is possible that the permeability may not affect the coupling strength as strongly as implied by equation 5-21. The same model as for the investigation of area effects was used but the dimensions were changed. In the model a metal disc with an inner diameter of 3mm and an outer diameter of 4.5mm was placed 20mm above an inductor. This design followed the dimensions of the rings used for the bonding pressure experiments described later in Section *7.2 Bonding Pressure*. The inductor coil had a radius of 40mm. The output current of the induction heater was chosen to be 490A with a frequency of 220kHz, also following the experimental settings.

Heating time was set at 10s. The thickness of the disc was set to be 7.5µm (which is the thickness of the samples used in experiments) and 1mm, respectively, and the temperature was simulated for a relative permeability of 1 and 100. The purpose of modelling a thick and a thin susceptor was to identify if permeability has a greater effect on the heating rate for thicker susceptors. As all other material parameters were irrelevant the pre-set values of copper were kept. A summary of the model details can be found in Appendix A6.4 *Modelling Effect of Permeability*.

6.1.2 Experimental Approach

When using structured susceptors the aim is to reduce the introduced material as much as possible while providing good plastic to plastic bonds at the interface. The susceptor still has to be big enough to generate enough heat in a practicable time. In order to investigate how susceptor size affects the heating rate, structured susceptors with different track widths were heated. As experience tells us a 1mm track width should be adequate, track widths of 0.5, 1, 2 and 3mm which span this figure were chosen. Also investigated was the

effect of shape, with the patterns being triangular, square and circular. The photolithographic etch mask for the patterns is shown in Figure 6-2.

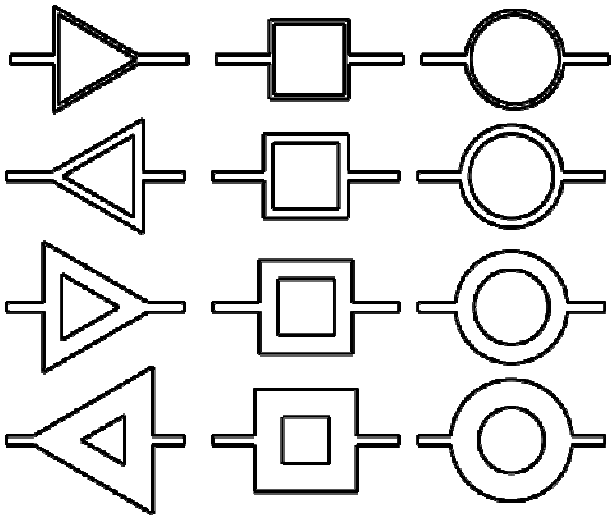

Figure 6-2. Susceptor photolithographic mask design

The mask was used in a photolithographic process to etch the susceptor circuits out of a 7.5µm thick nickel foil. Each circuit featured small ‘support beams’ which were used to hold it in place during heating, leaving the top surface of the active part of the susceptor freely exposed to air.

The circuits’ median circumference was kept constant at 31.5mm for all designs (Figure 6-3). Thus the mass m and conductor length l of different shaped circuits with same track width was approximately the same. Hence the only parameters varying between patterns of the same track width but different shape were the active area and the cross-sectional area

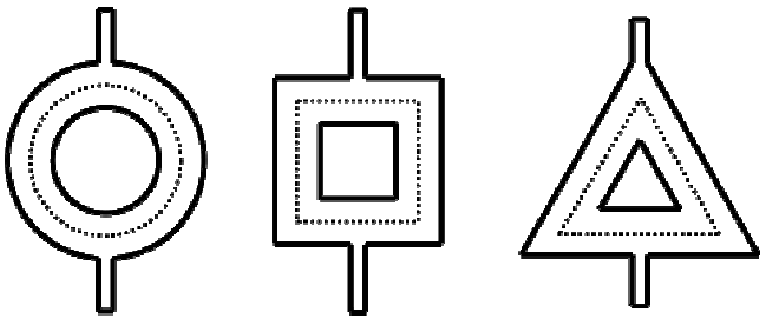

Figure 6-3. Designed circuits with median circumference

Two samples of each shape/track width combination were tested in order to improve the statistical significance of the results. A final pattern was used consisting of a straight metal track with a width of 1mm and a length of 31.5mm to allow comparison of the performance of open circuits with the performance of closed circuits. The etched nickel circuits were fixed on glass slides and placed at a distance of 25mm above the coil. The output current was set at 210A and the samples were heated for 10s. Non-contact temperature measurements were made with a Flir PM695LWB thermal imager which was placed above the setup focussing on the samples and sampling at a rate of 50Hz.

6.1.3 Area Effects

To identify how the susceptor area affects the heating rate the radius of the thin copper disc was varied while keeping its thickness constant. The maximum temperatures reached after 200s were calculated using COMSOL Multiphysics. Figure 6-4 shows some selected results:

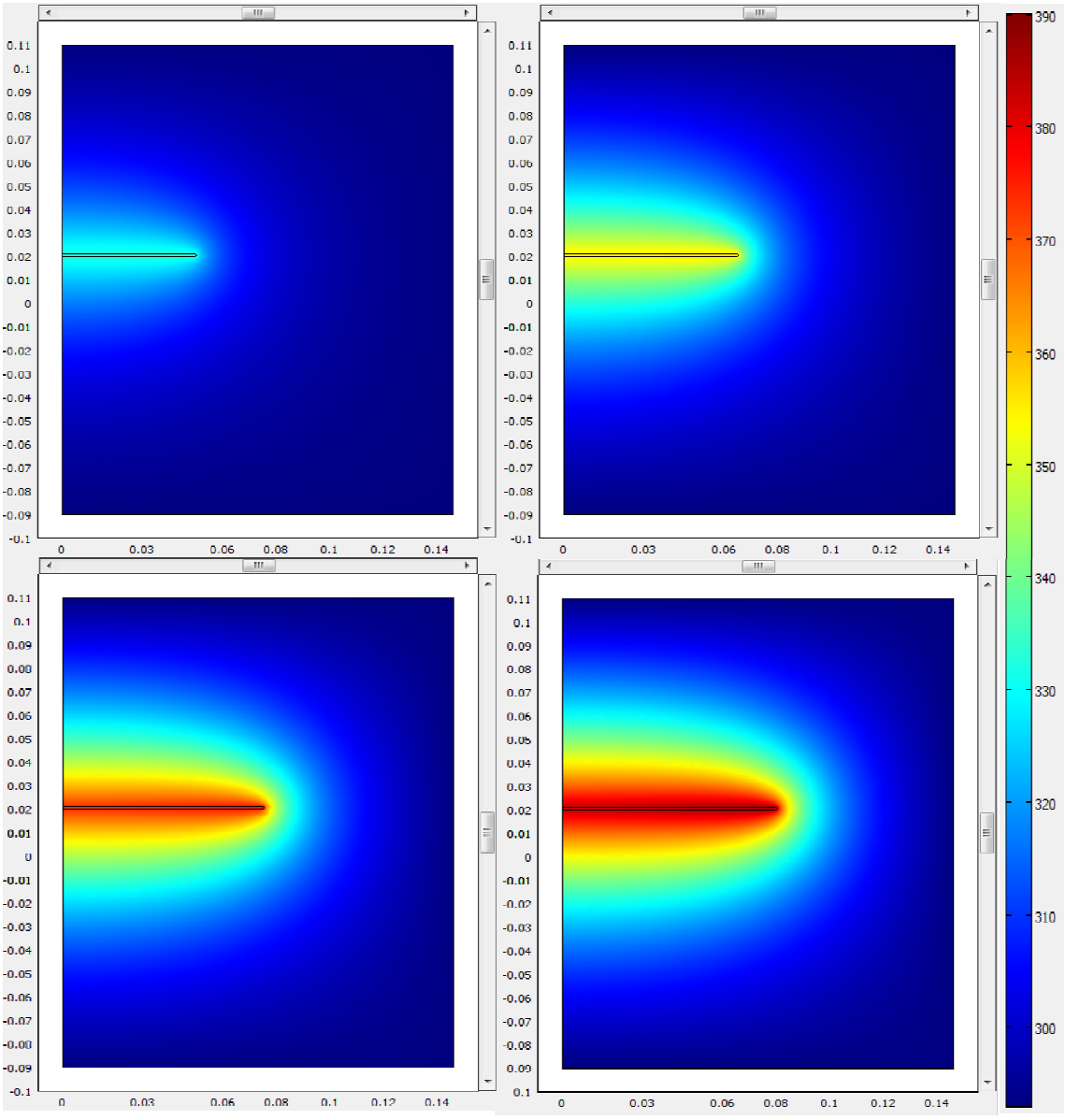

Figure 6-4. Heat distribution depending on susceptor area from COMSOL model. Radius of susceptor from left to right and from top to bottom: 50mm, 65mm, 75mm and 80mm. x- and y-axis are in m, colour scale bar in K.

The results from all simulations are plotted in Figure 6-5:

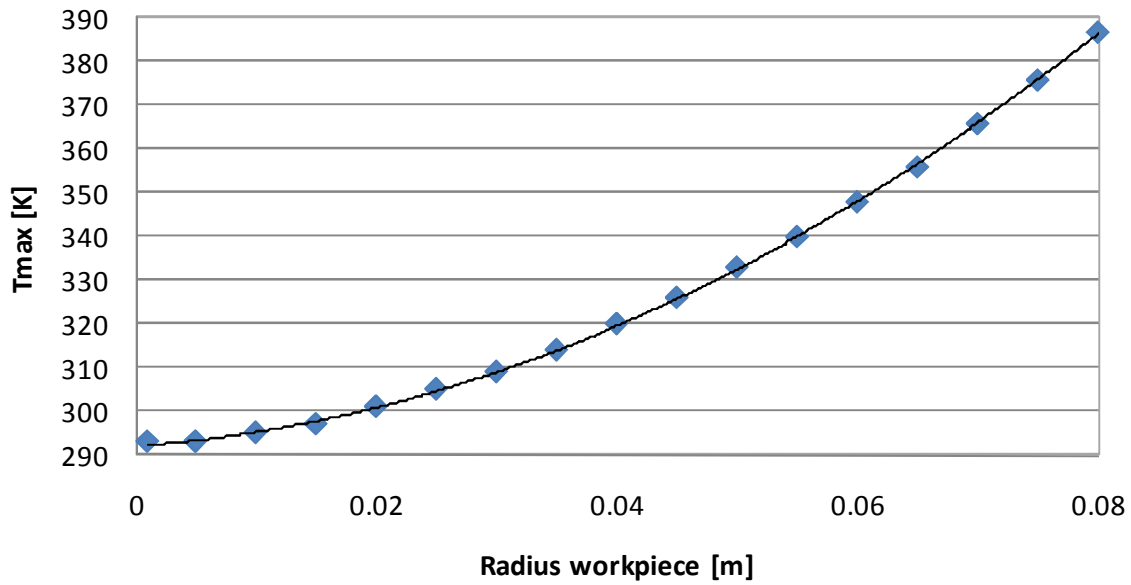

Figure 6-5. Change of temperature with varying area and constant thickness of susceptor from COMSOL simulation. The line is a guide to the eye.

As expected the curve shows a strong upward trend consistent with the quadratic relation between susceptor radius and generated heat in equation 6-1. The heating constant k_h then was calculated using a radius R of 80mm and its corresponding change of temperature from the COMSOL simulation ($k_h = \Delta T / R^2$). Using this heating constant and a reference temperature of 293K (as it was applied for the simulations) the maximum temperature was calculated for different radii and plotted together with the results of the simulations shown in Figure 6-5:

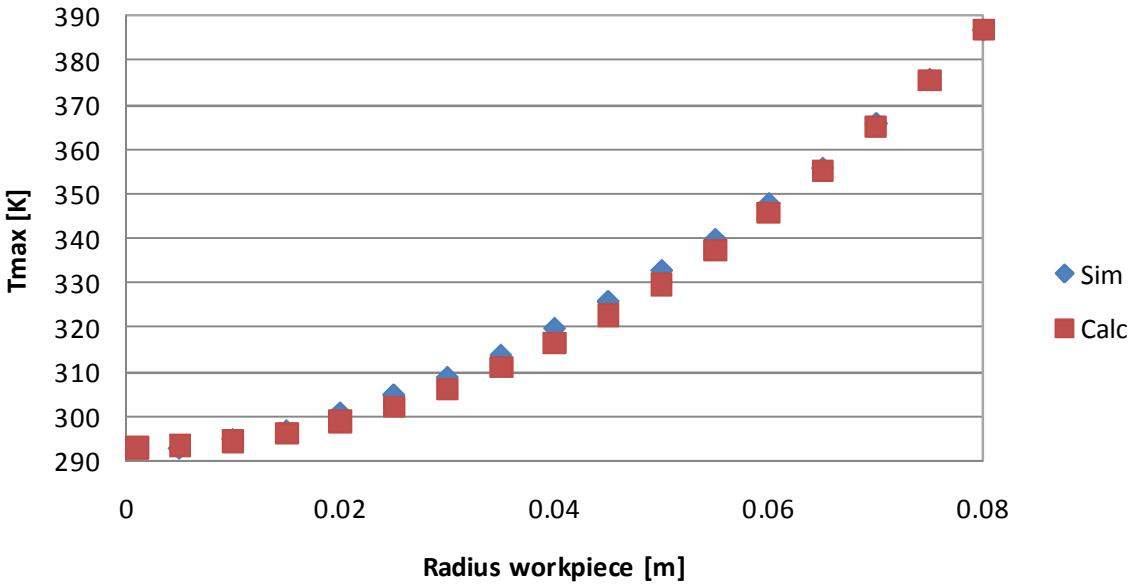

Figure 6-6. Change of temperature with varying area and constant thickness of susceptor from COMSOL simulation and calculated using equation 6-1.

As shown in Figure 6-6 the calculations from equation 6-1 show a good fit to the simulated results. The heating constant was calculated from the maximum radius used during the simulations, hence calculated and simulated temperatures are identical for that radius. But also for a radius of 0mm temperatures are the same, as no heating occurs. Hence, if cooling effects had an impact the calculated temperatures would be higher than the simulated ones for the medium sized radii (as the curve of the calculated temperatures was forced to fit the simulated temperatures for minimum and maximum radius). The results shown in Figure 6-6 illustrate that cooling does not seem to have an impact on the heating, at least for 1mm thick susceptors. This observation is in harmony with the results presented in Section *5.5 Cooling Effects*. The difference in simulated and calculated temperatures can be attributed to the temperature dependency of resistivity, which is ignored in equation 5-21.

6.1.4 Permeability

The effect of susceptor permeability on the heating rate was investigated. The heating of two metal rings with same material properties but different thickness t_w was simulated, for relative permeability set at 1 and 100. The calculated temperature after 10s heating using COMSOL Multiphysics are shown in Table 6-1:

Table 6-1. Results - effect of permeability

t_w	$\mu_r = 1$	$\mu_r = 100$
7.5µm	592K	592K
1mm	310K	339K

In this example the penetration depth for a relative permeability of 1 is 347µm, which is much greater than the thickness of the first disc, and 47µm for a relative permeability of 100, which is much smaller than the thickness of the second disc. However, the results clearly show that permeability is not an important factor for very thin susceptors. For thin materials the edge effects are significant, i.e. the magnetic flux in the region immediately above and below the susceptor, which is air.

6.1.5 Shape effects

In order to be able to compare different susceptor shapes experimentally the samples described above were heated. The sample code used in Figure 6-7 to Figure 6-9 consists of the sample shape – circular (C), square (S) and triangular (T) – and its track width (e.g. T1 is a triangular shaped susceptor with 1mm track width).

For the samples with a track width of 3mm the heating rate was so large that the nickel foil burnt and no analysable measurements could be made. The temperatures for round shaped susceptors were recorded as follows:

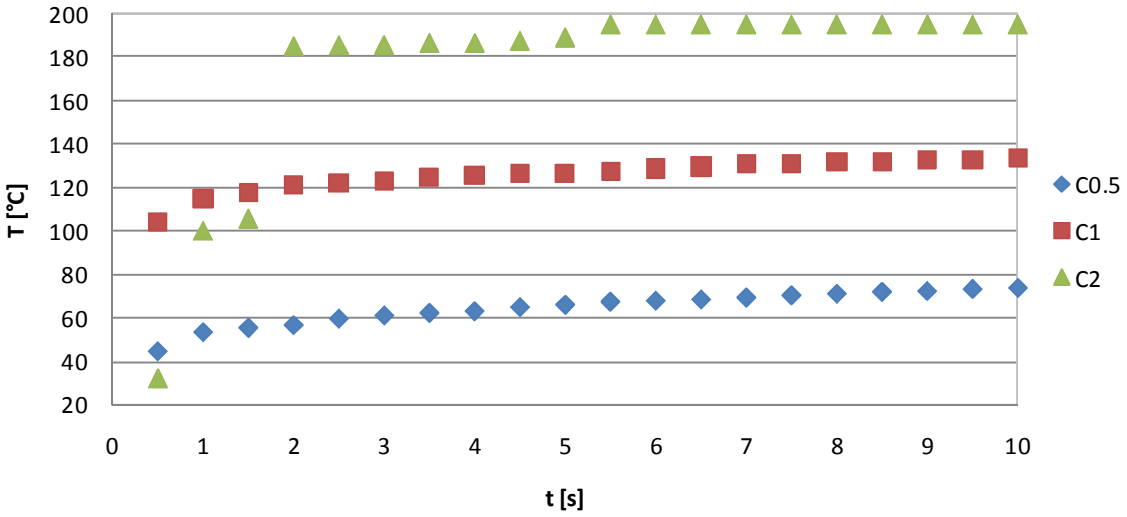

Figure 6-7. Temperature measured for circular shaped circuits with different track widths: 0.5mm (C 0.5), 1mm (C 1) and 2mm (C 2)

As shown in Figure 6-7 temperatures reach a plateau rather quickly. Response time, i.e. the time needed to reach 90% of the maximum temperature measured after 10s, is 5.5s for C 0.5 and 2s for C 1 and C 2, respectively.

For square shaped circuits temperature profiles were measured as shown in Figure 6-8:

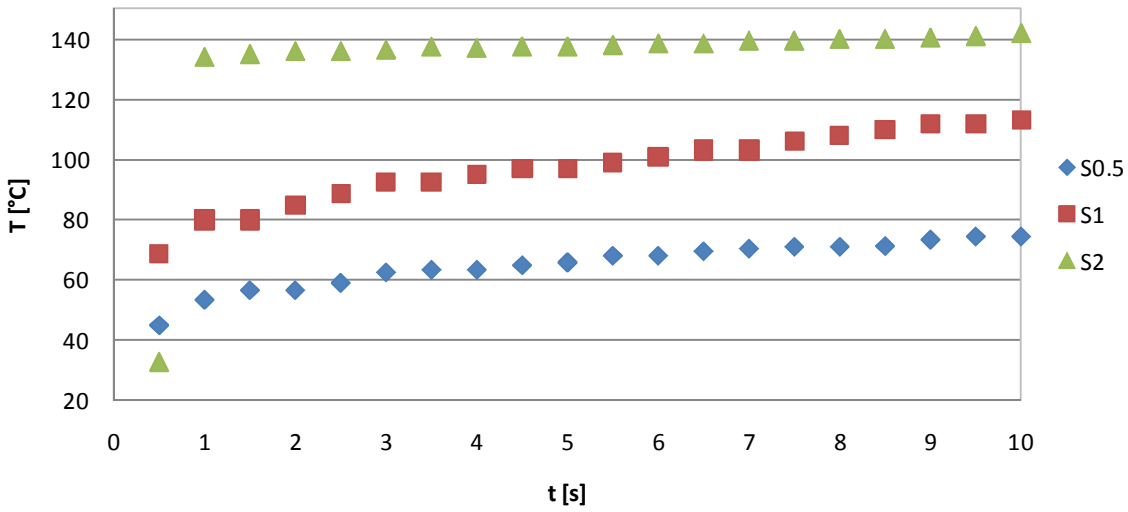

Figure 6-8. Temperature measured for square shaped circuits with different track widths: 0.5mm (S 0.5), 1mm (S 1) and 2mm (S 2)

Response time for S 0.5 is 5.5s, 6.5s for S 1 and 1s for S 2.

Finally the temperature for triangular shaped circuits was measured and plotted (see Figure 6-9).

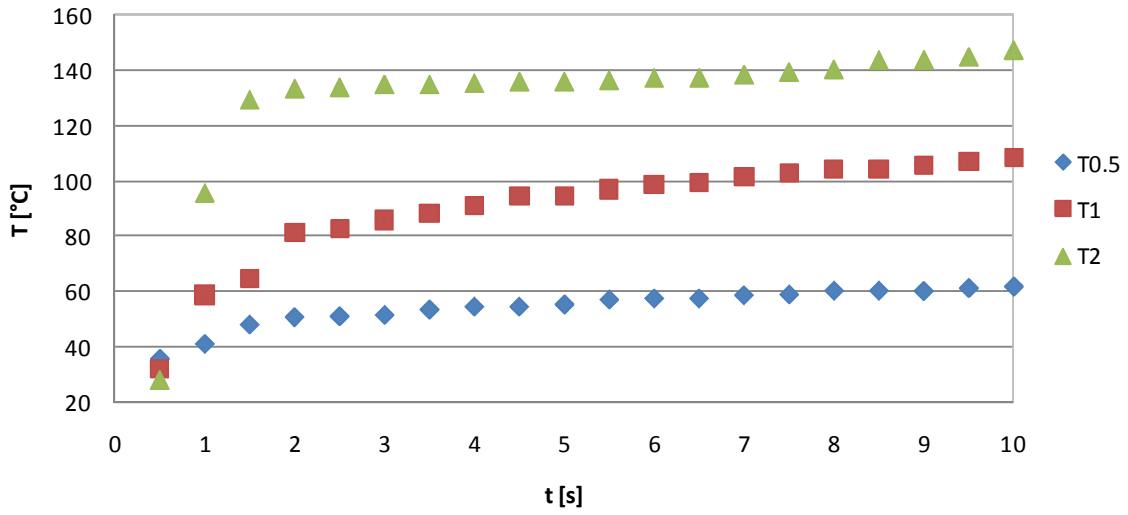

Figure 6-9. Temperature measured for triangular shaped circuits with different track widths: 0.5mm (T 0.5), 1mm (T 1) and 2mm (T 2)

Response times for the triangular shaped circuits are similar to the ones of square shaped circuits: 5.5s for T 0.5, 6s for T 1 and 2s for T 2.

To be able to compare the different measurements different parameters are needed. The designs all have the same median circumference but as they are shaped differently the active area and the 'void' area in the middle are different as well. Also the cross-sectional area of the square and triangular shaped circuits varies over their length. Table 6-2 shows the different circuits with their respective parameters:

Table 6-2. Parameters of different circuit designs

Circuit	w	w_{max}	A_{void}	A_a
C 0.5	0.0005	0.0005	7.09e-05	8.66e-05
C 1	0.001	0.001	6.36e-05	9.50e-05
C 2	0.002	0.002	5.03e-05	1.13e-04
S 0.5	0.0005	0.00071	5.48e-05	7.06e-05
S 1	0.001	0.00141	4.76e-05	7.92e-05
S 2	0.002	0.00283	3.48e-05	9.80e-05
T 0.5	0.0005	0.001	4.02e-05	5.59e-05
T 1	0.001	0.002	3.33e-05	6.48e-05
T 3	0.002	0.004	2.14e-05	8.44e-05

w is the minimum track width in meters, w_{max} the maximum track width (at corners) in meters. A_{void} represents the open area in the circuit's middle and A_a the active area, both are measured in square meters. The different values of the active area explain why S 0.5 reaches temperatures similar to C 0.5 but the temperature profiles of S 1 and S 2 are closer to T 1 and T 2, respectively.

Using the measured temperatures a constant efficiency factor connected to the susceptor shape was considered to be able to take account of the design in the analytical equation. From equation 5-21, which was used since equation 5-36 was too complex to extract an efficiency factor, the following relation is expected for circular susceptors:

$$\Delta T = k \cdot \frac{A^2 \cdot A}{m} \qquad (6\text{-}3)$$

where k represents all constant parameters. For non-circular susceptors an efficiency factor Φ was introduced:

$$\Delta T = \Phi \cdot k \cdot \frac{A^2 \cdot A}{m} \qquad (6\text{-}4)$$

t_w: Thickness of susceptor [m]

x: Functional factor of conductor length unitless

Then the temperature measured after 10s was plotted over the product of squared active area A_a and cross-sectional area A divided by the susceptor mass m. To extract the value of Φ the slope of the straight line fits (with origin passing through ΔT = 0 K) of triangular and square shaped susceptors was compared to the slope of circular patterns.

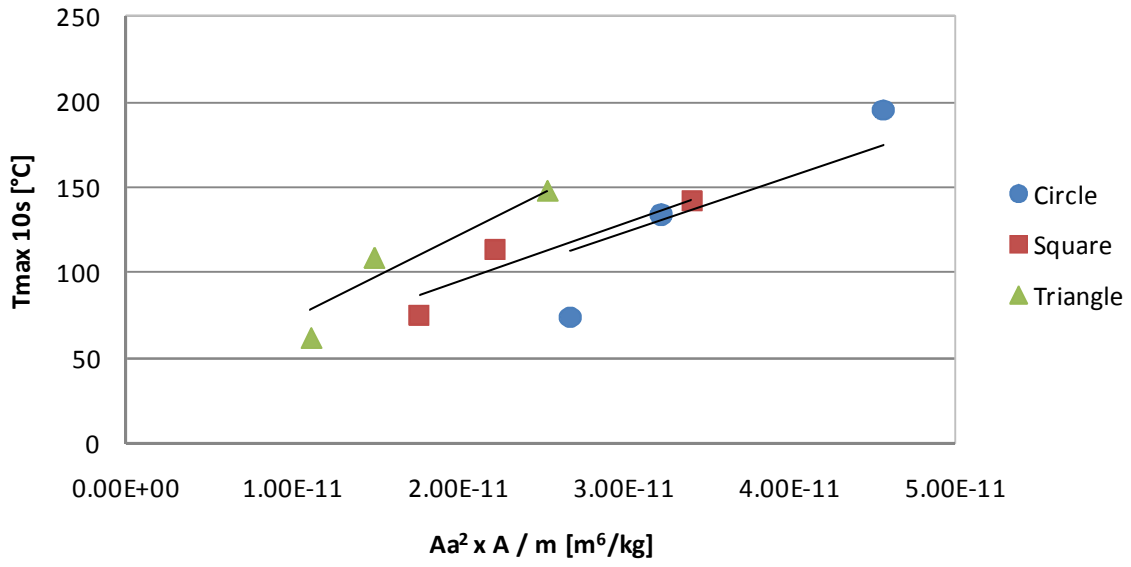

Figure 6-10. Efficiency factor of different susceptor designs

From the graph shown in Figure 6-10 it can be seen that non-circular patterns heat more than one would expect, but the straight lines do not fit the points well enough to extract a reliable efficiency factor. A damping effect can be identified for higher temperatures, which might be attributed to the change of resistivity (see Section *5.3 Change of Resistivity*), which is ignored in equation 5-21. It

was concluded that although equation 5-21 correctly describes the effect of most of the heating parameters, equation 5-36 should be used for process design and optimisation as it takes into account more of the process physics.

Finally the 1mm wide straight track was heated. But even with extended heating times the temperatures did not exceed 50℃. This de monstrates that closed circuits perform much better than open circuits, which should be considered when designing susceptors for low frequency induction bonding.

6.2 Cooling Effects

In sections *5.5 Cooling Effects* and *6.1.3 Area Effects* it was concluded that cooling effects might occur, but it seems that they do not have a significant impact on the heating rate. The temperatures measured in the previous section can be used to back up that assumption.

For large t, equation 5-36, which includes temperature dependence of resistivity, can be simplified as followed

$$\Delta T = \sqrt{\frac{2 \cdot k}{\rho_{ref} \cdot \alpha}} \cdot \sqrt{t} \qquad (6\text{-}5)$$

Plotting ΔT against the root of time should produce linear trends for large t if cooling effects have no impact. If they have an impact the graph should show some damping (sublinear trends).

As shown in Figure 6-11 to Figure 6-13 the graph shows linear or close to linear behaviour for greater t for all three susceptor shapes:

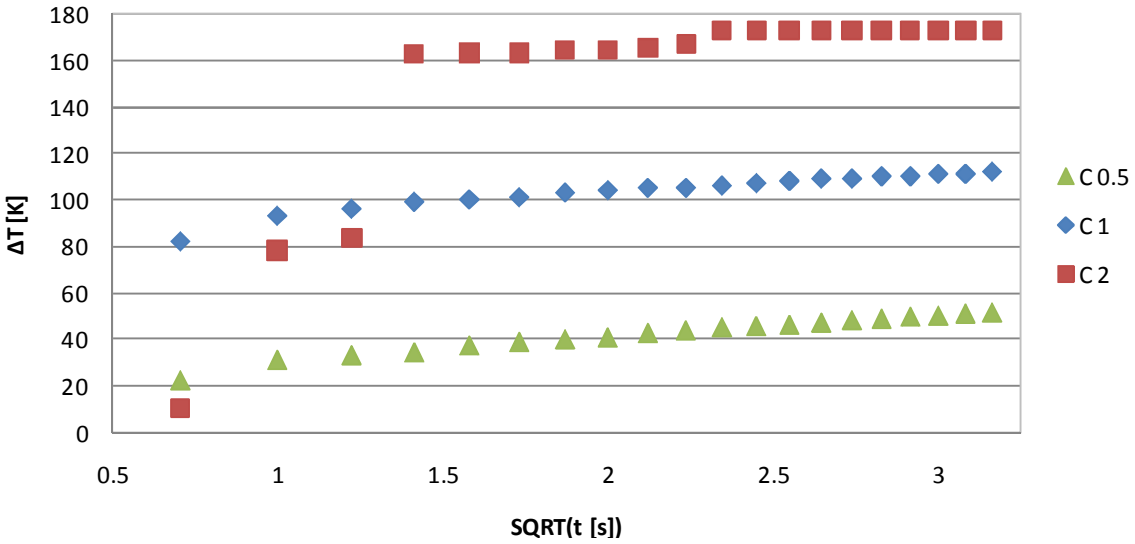

Figure 6-11. Change of temperature against root of time for circular shaped susceptors

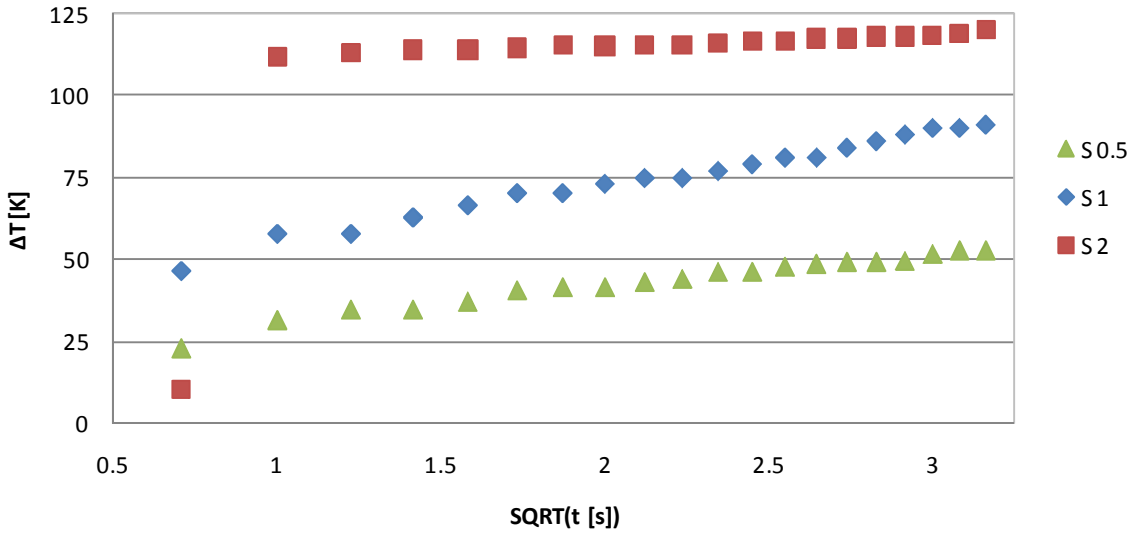

Figure 6-12. Change of temperature against root of time for square shaped susceptors

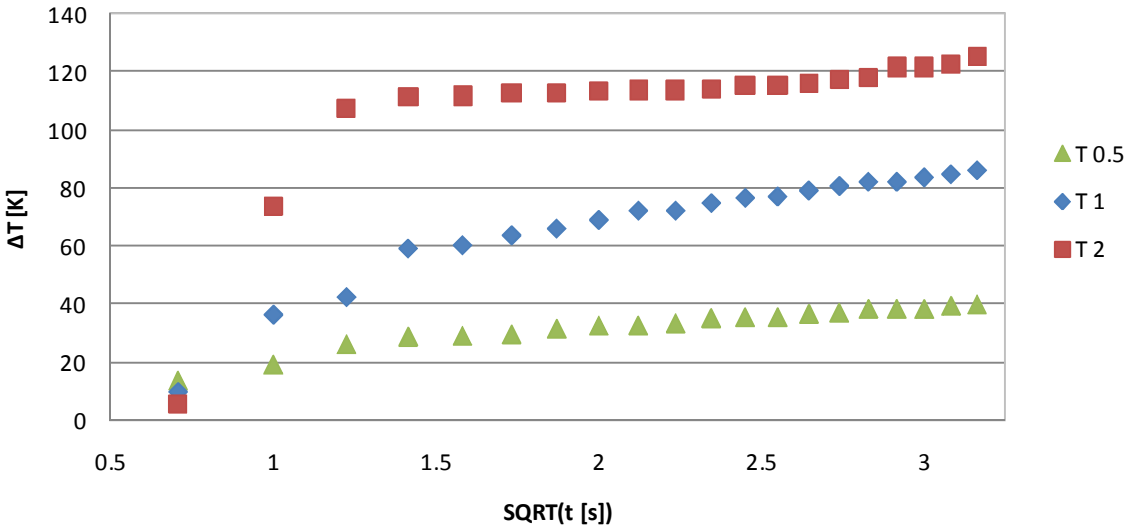

Figure 6-13. Change of temperature against root of time for triangular shaped susceptors

Provided that the analytical model takes account of all the important effects, this shows that cooling effects do not have an important impact on heating rates for the temperatures achieved during induction bonding. However, induction heating is a very complex process and as mentioned earlier in Section *5.6 Predicting the Temperatures*, the model is useful for describing the effects of different parameters on the heating rate, but it cannot be used for predicting exact temperatures.

Taking a closer look at the constant k in equation 6-5 might help to identify the limitations of the analytical model. The value of k for the measurements shown in Figure 6-11 to Figure 6-13 can be estimated by measuring the slope s of the curves for large t:

$$s = \sqrt{\frac{2 \cdot k}{\rho_{ref} \cdot \alpha}} \qquad (6\text{-}6)$$

$$\rightarrow \quad k = s^2 \cdot \frac{\rho_{ref} \cdot \alpha}{2} \qquad (6\text{-}7)$$

As k replaces most of the variables in equation 5-36 a factor k' is introduced to simplify the comparison of the different measurements. This factor excludes the 'geometrical' variables, such as conductor length l, mass m, active area A_a and cross-sectional area A. Hence it should be the same for all nine designs.

$$k' = \frac{\pi^2 \cdot I^2 \cdot f^2 \cdot \mu_0^2 \cdot \mu_r^2 \cdot r_Q^4}{2 \cdot Cp \cdot \left(r_Q^2 + x^2\right)^3} = k \cdot \frac{l \cdot m}{A_a^2 \cdot A} = \frac{s \cdot \rho_{ref} \cdot \alpha \cdot l \cdot m}{2 \cdot A_a \cdot A} \qquad (6\text{-}8)$$

Table 6-3 shows the values of k'-factor calculated for each experiment:

Table 6-3. k'-factor

Experiment	k'
C 0.5	18.61
C 1	12.43
C 2	10.39
S 0.5	25.40
S 1	72.02
S 2	3.60
T 0.5	15.55
T 1	55.80
T 2	9.77

This is not a satisfactory result. Most of the factors are of a similar order of magnitude, but the results prove that the analytical model does not take account of all the effects having an impact on the heating rate. According to the analytical model the theoretical value of k' was 7056. This is grossly different to the values shown in Table 6-3, which again demonstrates that equation 5-36 cannot be used for predicting exact temperatures. Nevertheless the analytical model has been shown to provide a good basis for estimating the effect of variation of different process parameters on the heating rate.

To summarise: based on calculations using the analytical model and the comparison of the predictions of functional dependencies of the model with those observed experimentally, it is concluded that cooling effects do not have a major impact on the temperatures reached during heating. However, discrepancies in the magnitude of quantities between the model and experimental observation appear to indicate that some parameters that do affect the temperature reached are being ignored in the model.

7 Polymer Bonding

Knowing the induction parameters affecting heat dissipation is not enough to ensure formation of bonds. It is also important to know the reaction of the polymer slides to the heat in terms of bond strength, melted material, bonded area and heat affected zone (HAZ), as well as the influence of bonding pressure.

The heat affected zone (HAZ) is an area where the material was not plasticised during heating but its microstructure was altered by the influence of heat. The molecules in this area are elongated, thus introducing a stress in the material. The size of the HAZ depends on the generated temperature and the thermal diffusivity of the base material. The higher the diffusivity the higher is the cooling rate and the smaller is the HAZ. Some applications need specific wall characteristics of the microfluidic channels so the size of the HAZ should be controlled to avoid alterations of those characteristics and the introduction of stress.

Flatness and cleanness of the substrates can also affect the bonding and also have to be investigated.

7.1 Substrate Issues

Parameters of the substrate surfaces, such as waviness and cleanliness can have great impact on the bonding process. An uneven surface or particles not only hinder the forming of a bond at the interface but also lead to thermal barriers.

7.1.1 Methodology

To examine the substrates' surfaces PMMA slides with a thickness of 4mm were profiled using a Talysurf CLI 2000. Originally the slides were purchased saw cut to a size of 40mm x 40mm but they were laser cut to a size of 20mm x 20mm prior to the measurements, as this was the size used for most of the experiments. In addition it now was possible to investigate the effect of laser machining on the surface quality.

Usually the substrates used for microfluidic systems are not so thick. Hence, saw cut PMMA slides with a size of 40mm x 40mm and a thickness of 2mm were also profiled.

To investigate the effect of thermal barriers a model designed to obtain the steady-state solution for the temperature profile in the sample was used, as described in Section 3.4.3 *Effect of Thermal Barrier (Air Gap)*. A heat source at 400K was brought into contact with a PMMA substrate (20mm x 2mm) and the heat distribution after 10s was measured. Then, an air gap of 5µm, 30µm and 100µm, respectively, was introduced between heat source and substrate and the heat distribution was compared to the ideal situation. To simplify the model the starting temperature of the whole setup was 0K. A summary of the model details can be found in Appendix A6.5 *Modelling Effect of Air Gaps*.

7.1.2 Results

Six 4mm thick PMMA substrates were profiled on both sides. All of the measured samples had a very smooth surface with a peak to valley flatness of 2-5µm. The image shown in Figure 7-1 is for illustrative purposes, a colour scale was not available.

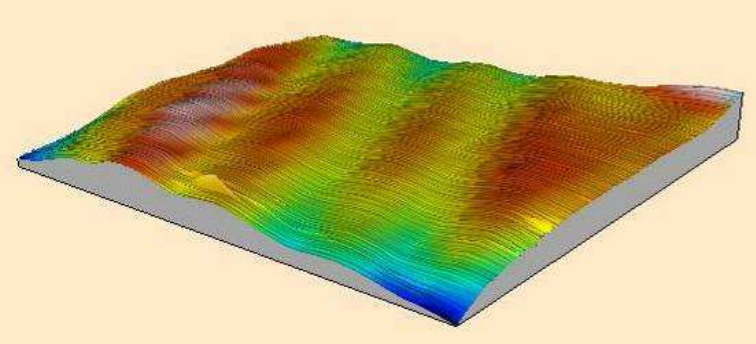

Figure 7-1. Profiled surface of 20mm x 20mm x 4mm PMMA substrate

Figure 7-2 shows the profile of the sample shown in Figure 7-1 measured on the centre line (left to right):

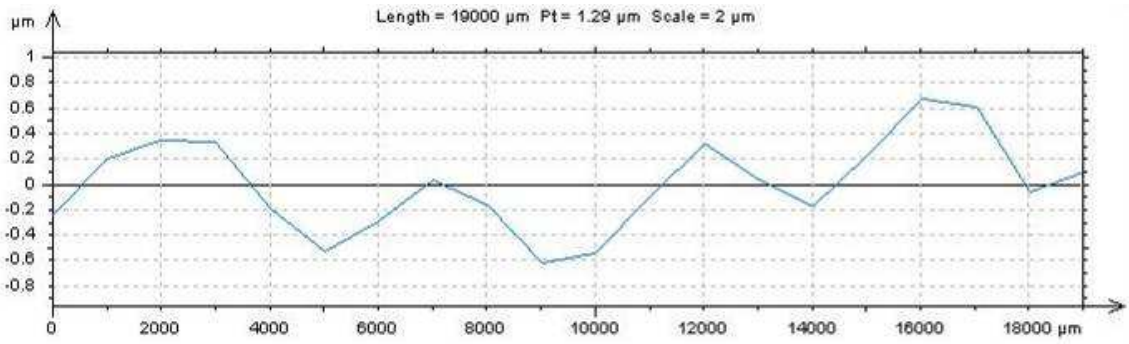

Figure 7-2. 20mm x 20mm x 4mm PMMA substrate profiled with Talysurf CLI 2000

The laser cut samples showed some debris at the cut edge which could have a thickness of several tens of µm as shown in Figure 7-3.

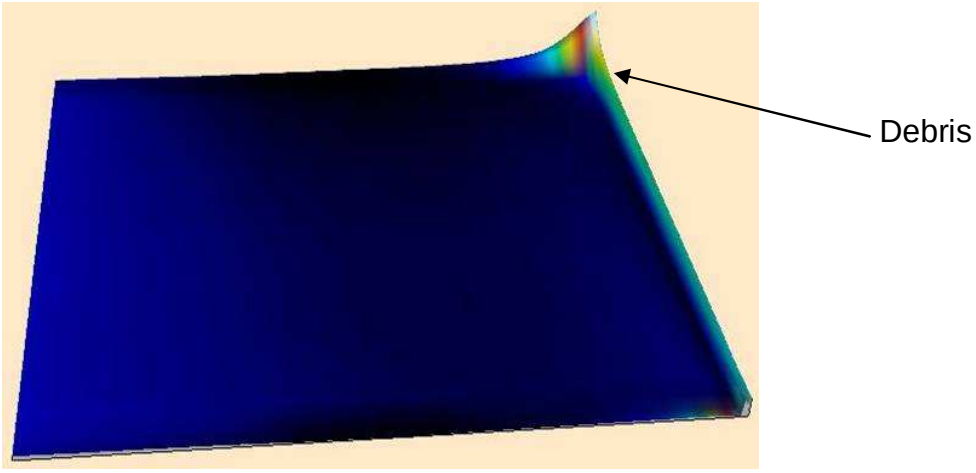

Figure 7-3. 20mm x 20mm x 4mm PMMA substrate with debris from laser cutting

Hence the side facing downwards during laser cutting was to be used as the interface during bonding.

Then three 2mm thick substrates were profiled, again on both sides. These measurements revealed a different problem. Some of the samples were concave / convex or saddle shaped. This lead to a peak to valley flatness of 30-40µm as shown in Figure 7-4:

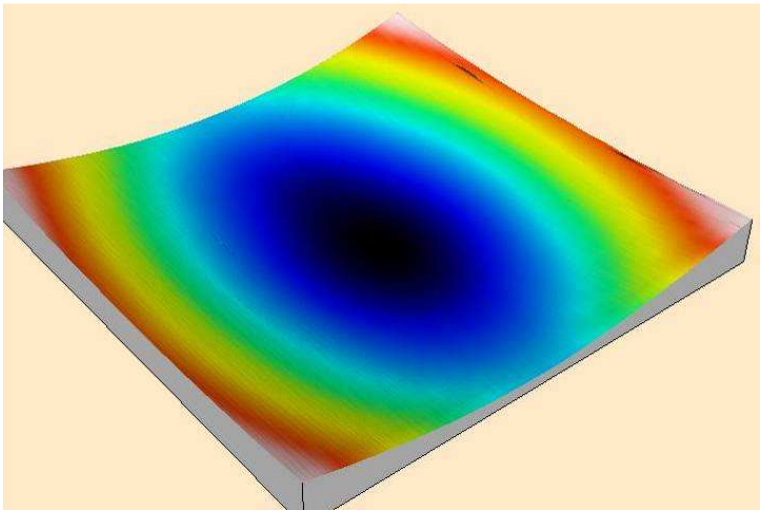

Figure 7-4. 40mm x 40mm x 2mm PMMA substrate with deformed surface

Due to that waviness it is critical to apply enough pressure during the bonding process so that the surfaces are in good contact.

Some measurements showed peaks of 50µm or more, which were attributed to dust particles. This occurred even though the surfaces were protected by a foil prior to the measurements and gloves were worn during handling. A conventional air duster was found capable of removing all particles and therefore should be used before bonding.

The effects of thin thermal barriers were investigated using COMSOL Multiphysics simulation software. The results are shown in Figure 7-5:

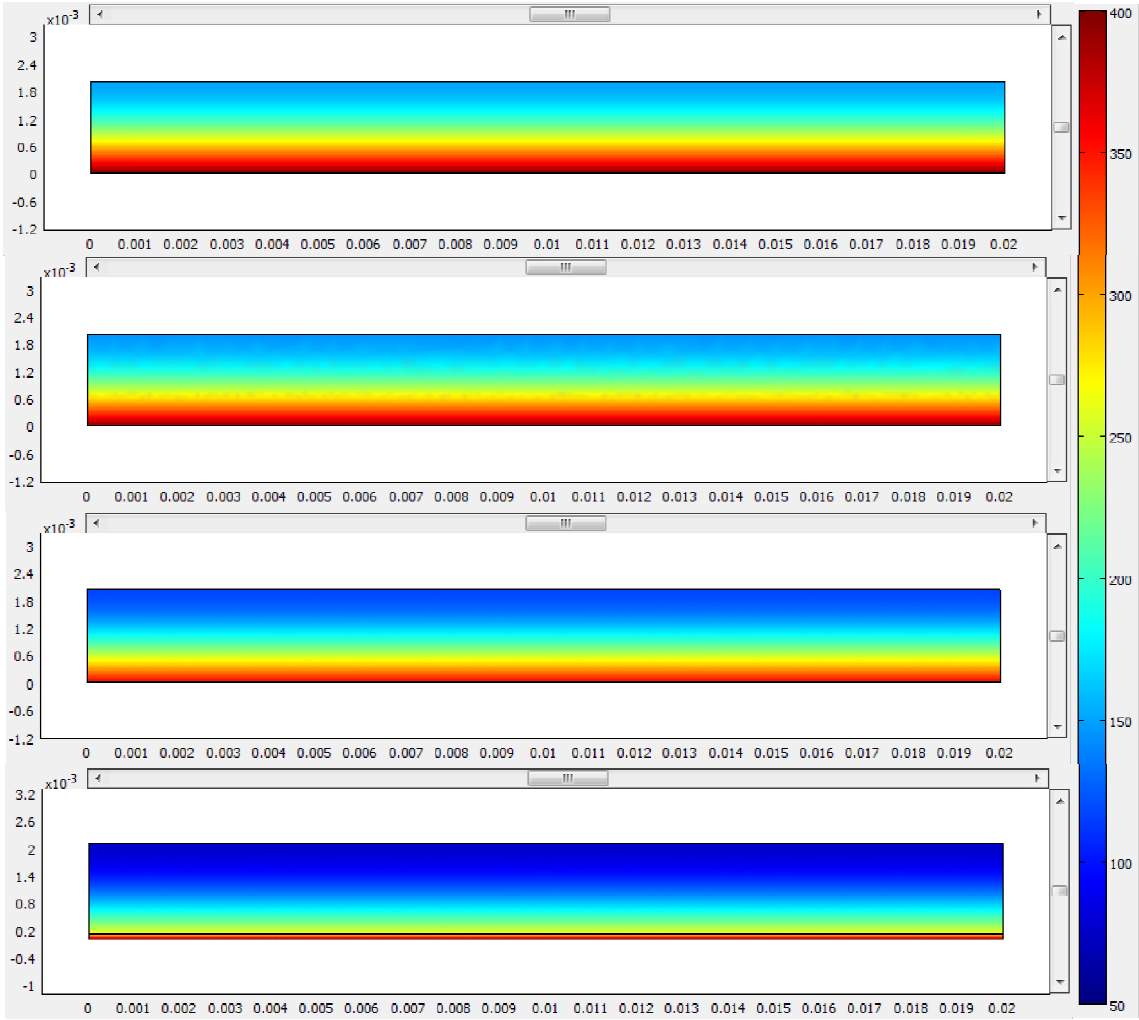

Figure 7-5. Heat distribution through 2mm PMMA with (top to bottom) no air gap, 5µm air gap, 30µm air gap and 100µm air gap. x- and y-axis are in m, colour scale bar in K.

The heat distribution obtained in the ideal situation, with no thermal barrier and the heat source in contact with the substrate is shown in Figure 7-6a:

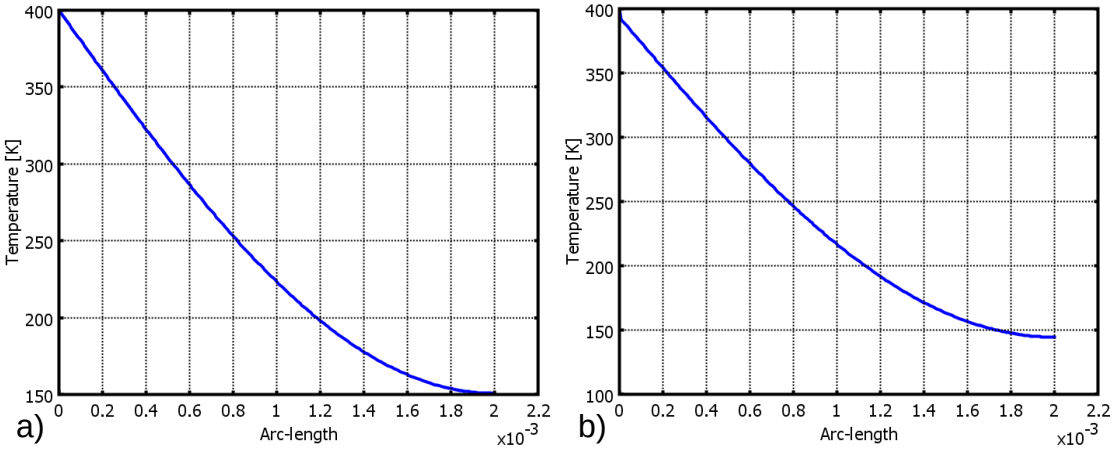

Figure 7-6. Heat distribution a) through 2mm PMMA with no air gap and b) through 5µm air and 2mm PMMA. Heat source is at the left hand side of the figures. Arc length is in m.

When a thermal barrier in form of an air gap is introduced between the heat source and substrate, the latter is seen to be heated less. As shown in Figure 7-6b the side of the substrate facing the heat source only reaches a temperature of around 390K after 10s of heating, 10K less than in an ideal situation.

For thermal barriers with a size of 30µm and 100µm, the maximum temperature of the substrate was only around 355K and 260K, respectively, as can be seen in Figure 7-7:

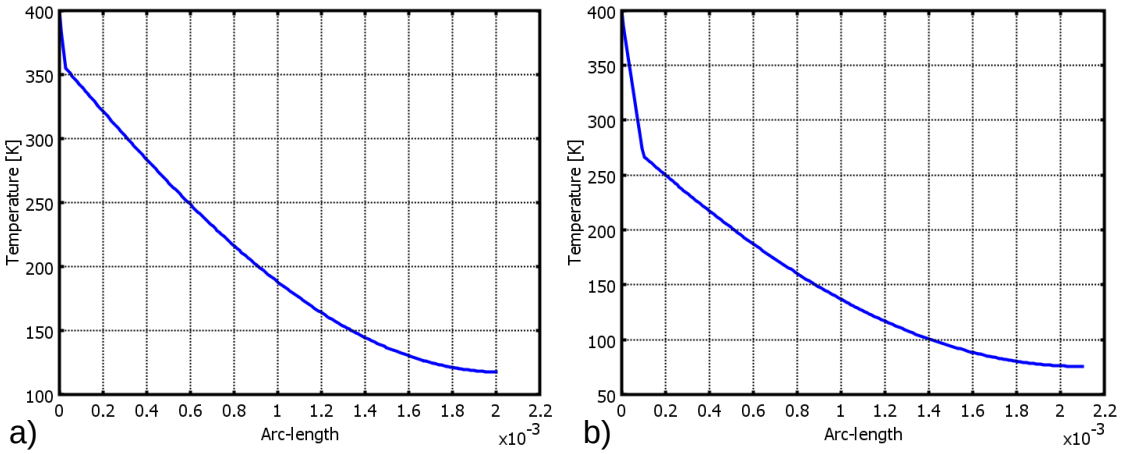

Figure 7-7. Heat distribution a) through 30µm air and 2mm PMMA and b) through 100µm air and 2mm PMMA

Thus, better contact of the substrates would be expected to not only help in creating the bond (see Section *7.4 Forming of Bonds*) but also leads to a more efficient heating of both surfaces

To summarise: while the surface usually is very smooth with a peak to valley flatness of around 5µm, the substrate can have a waviness which would lead to thermal barriers. Also, preceding manufacturing steps like laser machining can lead to debris or contamination of the surface. These artefacts should be considered when designing the bond process, e.g. by using the side without debris as the interface during bonding. To avoid the enclosure of particles the use of an air duster to clean the surface has been shown to be effective. To apply pressure during bonding is essential to support the forming of bonds and to avoid thermal barriers that can reduce the efficiency of the heating process drastically.

7.2 Bonding Pressure

PMMA contains water which might contaminate a substrate's surface when being heated, thus preventing the forming of a bond at the interface. It was observed in the work reported in previous chapters that very often the melted zone was larger than the bond area. It is desirable that the melted zone and heat affected zone (HAZ) are as small as possible, preferably not larger than the bond area, otherwise melted material could contaminate or alter the characteristics of structures and channels in the microfluidic chip. Also, the stress introduced in a HAZ might lead to distortions in those structures. As reported in the previous chapter the waviness of the polymer substrates might lead to decreased bond strength and quality. It was therefore investigated how the bonding pressure influences bond strength, melted zone and HAZ.

7.2.1 Design of Experiment

Simple stacks of two PMMA substrates with an intermediate susceptor were heated with different heating times and bond pressures. The substrates had a size of 20mm x 20mm and a thickness of 4mm. The susceptor was a ring with an inner diameter of 6mm and an outer diameter of 9mm etched out of a 7.5µm thick Ni foil in a photolithographic process. This means there was a 7.5µm gap between the substrates at the beginning of the bonding process making the application of pressure even more necessary. The susceptor ring was designed to fit the demands of a microfluidic device designed by Cranfield University (see Section *7.5.3 Multi Layer Bond*). The same photolithographic mask was used for this work.

The stack was placed as close as possible (distance coil-susceptor: 20mm) above the centre of the inductor coil. The output current of the induction heater was set at maximum (490A) with a frequency of 220kHz. Three different bonding pressures were used: 14, 29.4 and 44.8kPa, respectively. The heating time was varied between 15s and 25s, leading to a total of six different experiments:

Table 7-1. Bonding parameters - pressure variations

Experiment No.	Heating time [s]	Bonding pressure [kPa]
1	15	14
2	15	29.4
3	15	44.8
4	25	14
5	25	29.4
6	25	44.8

In each experiment at least four samples were bonded and two samples for air pressurising tests were prepared. The air pressure samples had a 4mm hole drilled in the upper substrate prior bonding. After each bonding the pressure

was applied for another 20 seconds to facilitate solidification of the melted polymer.

Apart from testing the maximum possible air pressure before leaking, the samples' bond shear strengths were determined. The bond area was then examined with a light microscope to identify the size of melted zone and bond area. To measure the size of the heat affected zone an optical microscope with polarising filter was used.

For the shear strength tests a specific jig had to be designed. It consists of two parts, each nesting one of the substrates as shown in Figure 7-8:

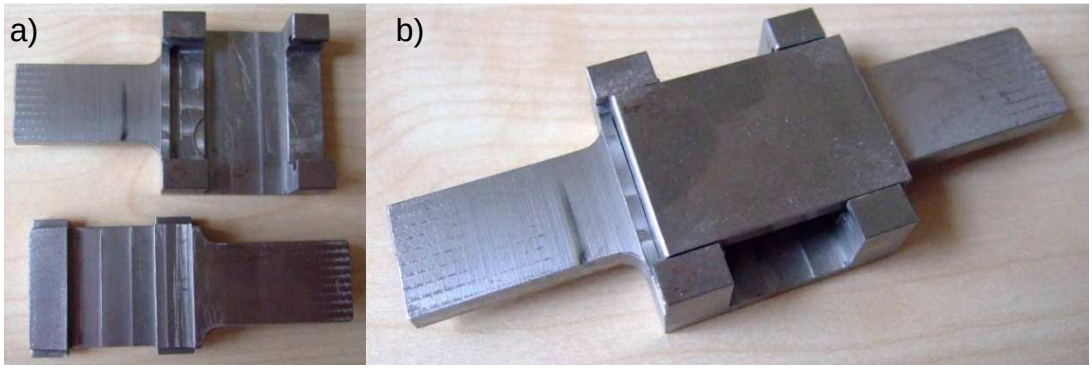

Figure 7-8. Jig for shear strength tests: a) individual parts and b) whole jig

The jig is designed to fit into the clamps of a shear strength tester run in tensile mode. The shear strength of the bonds was measured by pulling apart the test samples. For the tests the extension rate was set at 1mm per minute. Each test was stopped when the pulling force dropped by 20% in 100ms, i.e. when the bond broke.

7.2.2 Results & Discussion

First the samples from experiments 1-6 were air pressure tested. A 4mm connector tube was attached to the hole drilled into the upper substrate. Pressure was increased in steps of 35kPa and each pressure was applied for one minute. A maximum pressure of around 590kPa could be applied. Samples from experiment 1 and 4 leaked at around 400kPa and from experiment 2 withstood a pressure of 450kPa before showing leaks. Maximum pressure could be applied for the samples from experiments 3, 5 and 6. These are acceptable results as a leaking pressure between 100 and 200kPa is sufficient for most applications. Lower bonding pressure results in reduced leakage pressure and longer heating times lead to increased bond strengths. It was found that bonds with high leakage pressure could be formed at reduced heating times when high bonding pressure is applied. This also helps to reduce the width of the melt area.

The samples were then put into the jig and pulled apart to measure the shear strength of the bonds. The pulling force at which the bonds broke is plotted in Figure 7-9:

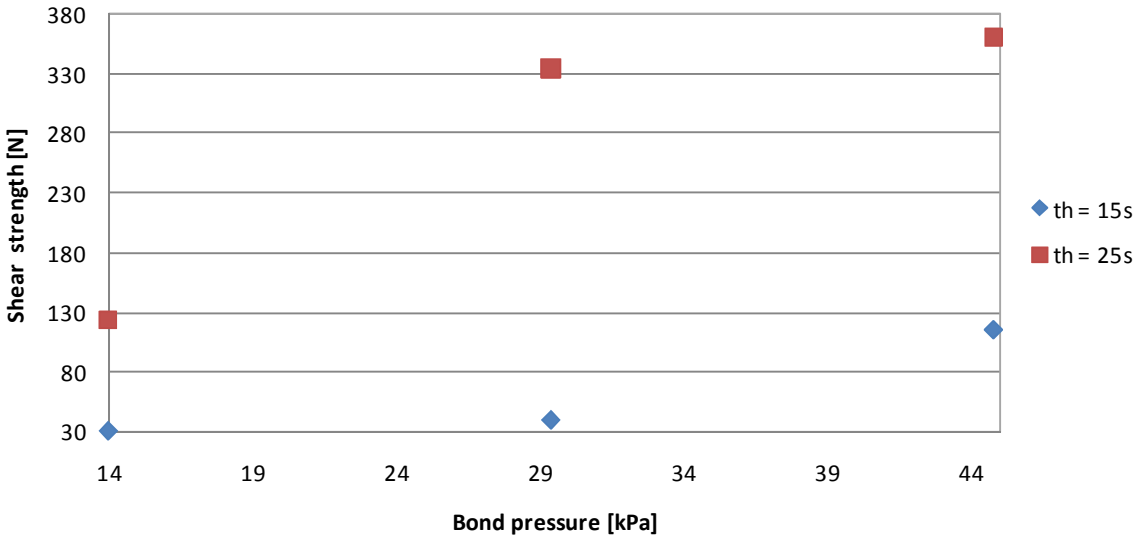

Figure 7-9. Shear strength of bonds created with different bonding pressures and heating times

Using equation 3-1, the bond strength was calculated from bond area (measurements described later in this section) and shear strength as shown in Figure 7-10:

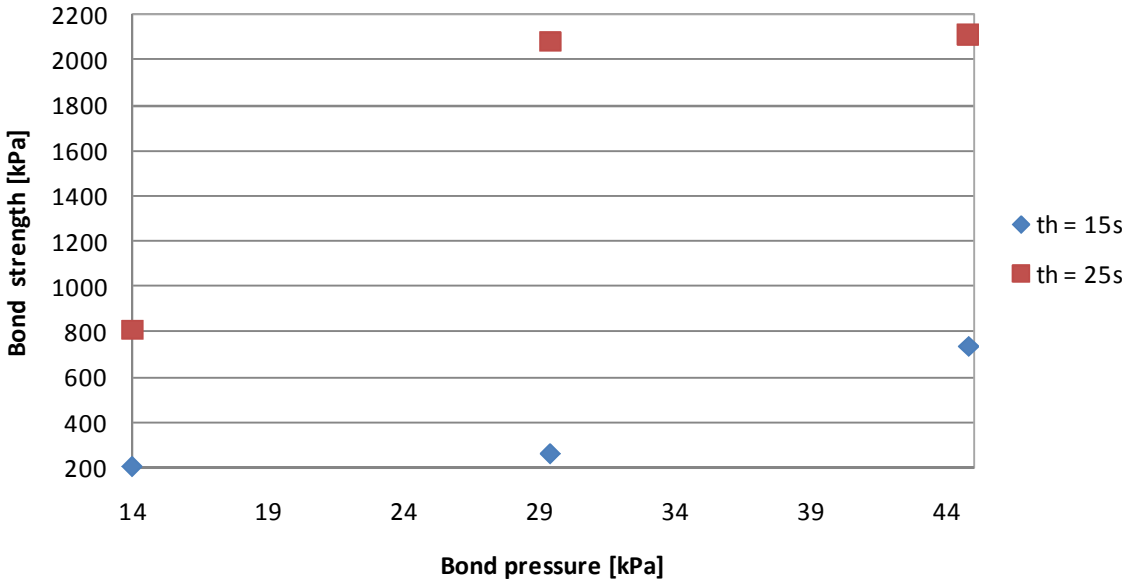

Figure 7-10. Bond strength of bonds created with different bonding pressures and heating times

With longer heating a significant increase in bond strength was seen. Higher bonding pressure also leads to better bonds. This is probably due to the substrates' surfaces having better contact during bonding. It was observed that the samples from experiment 3 withstood higher leakage pressures than samples from experiment 4, although having slightly smaller bond strengths. Apparently higher bonding pressure leads to more complete bonds without voids or un-bonded gaps causing leakage.

After breaking the bonds the surfaces were visually inspected under a microscope to measure the melted zone and the bond area. The nickel ring and surrounding melt area of an example specimen are clearly visible in Figure 7-11. The light region around both sides of the ring is the broken bond.

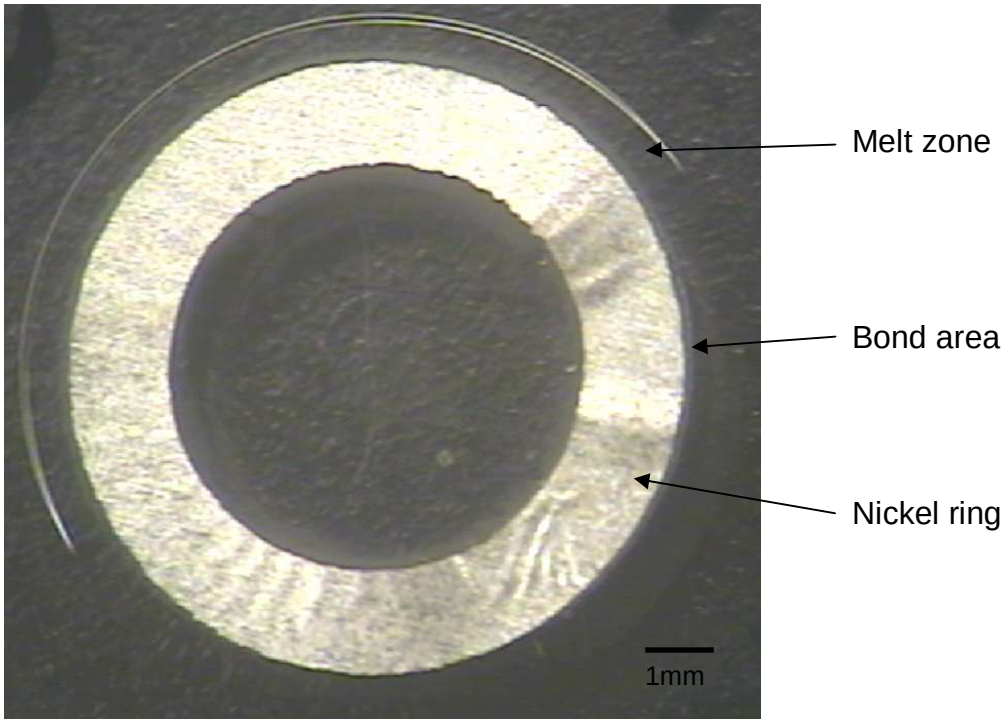

Figure 7-11. Microscopic image of bonded surface after breaking the bond

The widths of bond area and melted zone were measured for all samples on both sides of the Ni ring separately and the average value is plotted against the bonding pressure in Figure 7-12 and Figure 7-13:

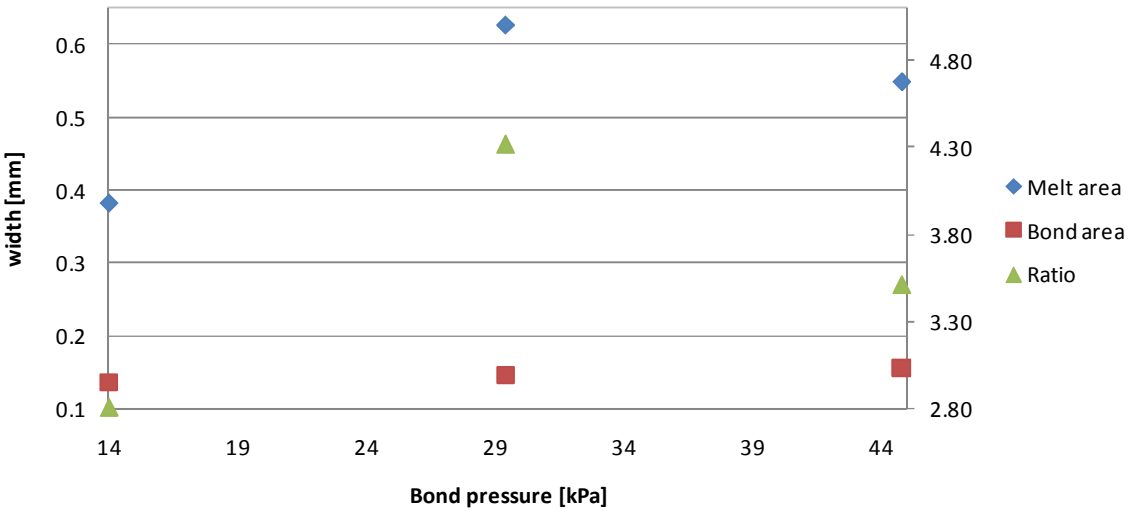

Figure 7-12. Width of melt and bond area after 15s heating. The right hand y-axis is for the ratio of melt over bond width.

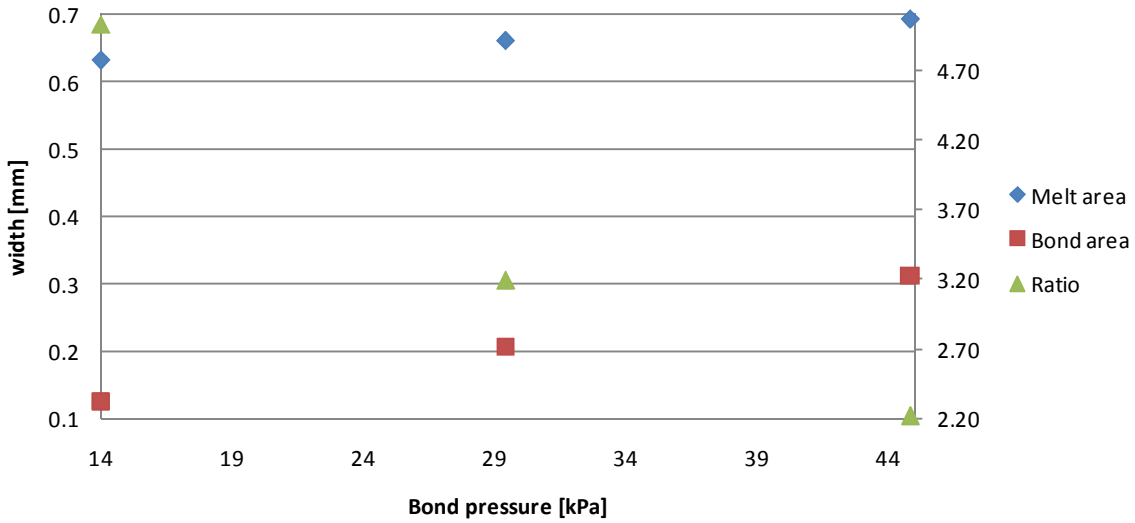

Figure 7-13. Width of melt and bond area after 25s heating. The right hand y-axis is for the ratio of melt over bond width.

The widths of both bond area and melted zone are smaller than 1mm for all experiments and increase with higher bonding pressures but the ratio melt / bond width decreases. A lower ratio means the melt width is closer to the width of the actual bonded area. Hence a high bond pressure is desirable as it reduces that ratio.

In Figure 7-12 there is a runaway value for melt width. This can be attributed to the high standard deviation of the measurements. The standard deviation of the melt area's width for the 14kPa bond pressure measurements is almost 0.2mm, and around 0.14mm for the other two measurement points. The standard deviation of the bond area widths is 0.1, 0.07 and 0.04mm, respectively, for the three measurement points. For the measurements shown in Figure 7-13 the standard deviation is only slightly smaller but with higher absolute values the relative error is much smaller.

The heat affected zone (HAZ) can be made visible using a polarising filter. It then appears as shadow adjacent to the melt zone as shown in Figure 7-14.

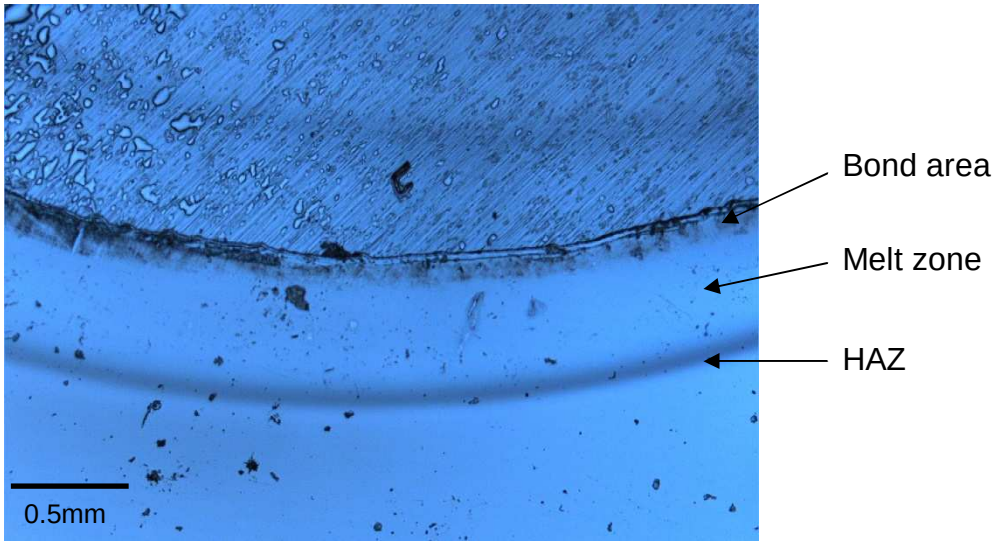

Figure 7-14. Microscopic image with polarising filter showing bond area, melt zone and HAZ

The width of the heat affected zone was measured for all samples and plotted against the bonding pressure as shown in Figure 7-15:

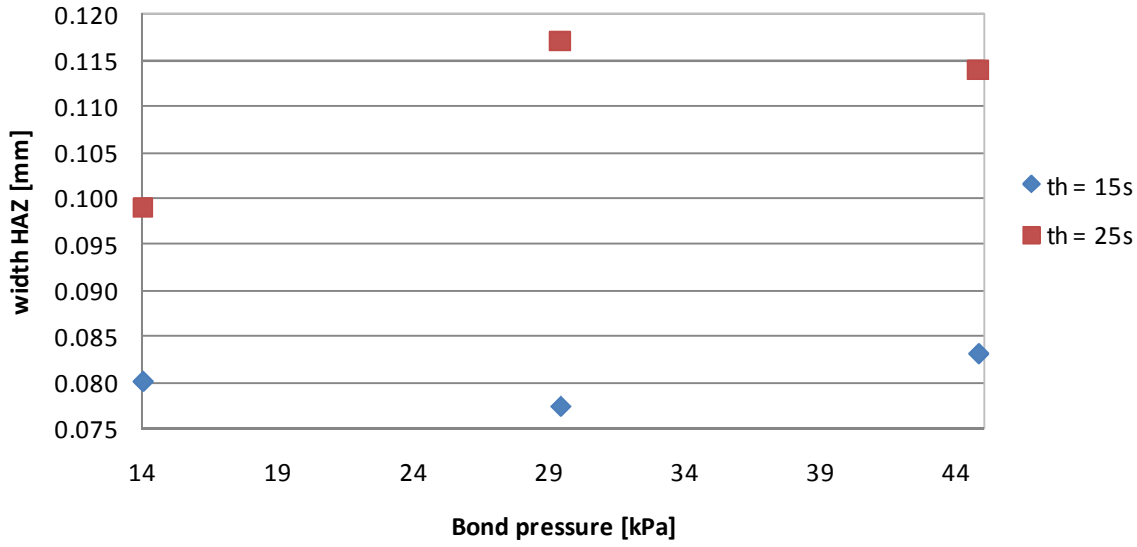

Figure 7-15. Width of heat affected zone for different bond parameters

The HAZ is much larger for longer heating times and increases slightly with higher bonding pressure, similarly to the behaviour seen with the width of the melted zone. As the size of the HAZ also depends on the thermal diffusivity and the temperature, this result was expected. However the size of the HAZ is small compared to the size of the melted zone.

To summarise: in order to reduce the melt area width the heating time has to be reduced. To maintain high leakage pressure the bonding pressure applied during the process has to be increased. To estimate a further reduction of heating time and melt area the results from experiments 3 and 4 were used, as they showed similar bond strengths. The heating time and thus width of melt area could be reduced by 40% and 13%, respectively, by applying a pressure three times greater. This means a bonding pressure of 135kPa is needed to reduce heating time to 9s, thus reducing the melt area width to 0.49mm while still providing good bond strength and high leakage pressure.

7.3 Pulsed Heating

Heating and melting of the polymer only is needed in an area close to the susceptor, but the material needs to be heated for several seconds to form a bond. Delivering the heat continuously leads to larger melt areas and might cause the burning of polymer, as the susceptors reach temperatures above 200°C rather quickly. Hence pulsed heating was considered as a method of limiting the extent of melted zone and heat affected area while still providing good bond strength. Using this technique burning of the polymer can be avoided as well (see section *7.4 Forming of Bonds*).

7.3.1 Design of Experiment

In the bond pressure variation experiments heating times between 15 and 25s were seen to be enough to provide sufficient bond strength to withstand 590kPa of pressure. To compare pulsed heating with continuous heating six different experiments with three and four heating times were designed. In Section *6.1.5 Shape effects* the response times of the heating process were around 2s for different shapes of susceptors. The nickel rings used for the pulsed heating experiments were smaller in active area but with a track width of 1.5mm heating times in the same order should be sufficient to heat the polymer above glass transition temperature. The cumulative length of heating time in the experiments

only varied from 6s to 9s whereas the total bonding times, which varied between 21 and 30s, were similar to the times quoted above (see Table 7-2).

Table 7-2. Bonding parameters - pulsed heating

Exp. No.	Heating time [s]	Cooling time [s]	No. of pulses	Total time [s]	Bonding pressure [kPa]
p1	2	5	3	21	29.4
p2	2	5	3	21	44.8
p3	2	5	4	28	29.4
p4	2	5	4	28	44.8
p5	3	7	3	30	29.4
p6	3	7	3	30	44.8

Experiments p1 and p2 were chosen to have three heating pulses, each followed by 5s of cooling. Experiments p3 and p4 were designed to test four heating pulses. Again cooling time after each pulse was 5s. To test longer heating-cooling-cycles experiments p5 and p6 were designed. Each of the three heating pulses was followed by 7s of cooling. Output current (490A) and distance coil-susceptor (20mm) were the same as during the bond pressure variation experiments.

7.3.2 Results & Discussion

The aim of the investigation was to see if pulsed heating can maintain the bond quality achieved with continuous heating while reducing the size of melted zone and HAZ. Again the samples' failure pressure with air and the shear strength were tested and the widths of melted zone, bond area and heat affected zone were measured.

Samples of all experiments withstood the maximum pressure of 590kPa for more than a minute without failing. The results of the other measurements are shown in Table 7-3:

Table 7-3. Test results of pulse heated samples

Exp. No.	shear str. [N]	bond str. [kPa]	melt area [mm]	bond area [mm]	ratio m/b	HAZ [mm]
p1	24.5	162	0.30	0.10	3.00	0.05
p2	25	164	0.31	0.12	2.58	0.05
p3	26	172	0.29	0.10	2.90	0.06
p4	27	177	0.34	0.12	2.83	0.06
p5	35	231	0.37	0.11	3.36	0.06
p6	35	231	0.38	0.11	3.45	0.06

The size of melted zone, bond area and heat affected zone are similar for all experiments but the longer heating-cooling-cycle of experiments p5 and p6 provided a better shear strength. Quality of all bonds is very good as they showed no leakage in the air pressure tests. That means that pulsed heating can be used to decrease the melted zone area while providing a good bond.

7.4 Forming of Bonds

In order to explain some of the observations described in previous sections it is essential to understand what is happening during melting and bonding of polymers. PMMA, which was used for the experiments presented in this work, is a thermoplastic polymer. That means it can be reversibly softened and hardened by heating and cooling.

When the polymer is heated the polymer chains elongate, thus introducing a stress in the material. This area is referred to as heat affected zone (HAZ). When the glass transition temperature T_G is reached the material plasticises, hence the polymer chains can move more freely.

If the plasticised surfaces of two polymer substrates are brought into contact, bonds can be formed. The application of pressure is critical for the forming of the bonds as it causes the interdiffusing and entangling of the polymer chains, which largely account for the resulting adhesion. During cooling the polymer chains resettle and become rigid again.

To form a bond the area where it is desired needs to be heated at least to glass transition temperature. During induction bonding the heat is generated in the susceptor and the surrounding polymer is heated by conduction. As the coefficient of thermal conductivity of PMMA is small compared to that of metals it takes a few seconds to plasticise an area large enough to form strong bonds. Generating heat continuously provides enough energy to plasticise that area but it might also lead to burnt polymer close to the susceptor. In Section *7.3 Pulsed Heating* pulsed heating is presented as an alternative mode. High energy pulses followed by short cooling periods enable plasticising the polymer without reaching temperatures that might damage the material. Ideally the process is controlled in a manner to only plasticise the polymer (without melting it), thus avoiding extended melt areas as observed for continuous heating. This might explain the good results reported for pulsed heating experiments in Section *7.3 Pulsed Heating*.

The application of pressure is important for the forming of bonds but it also serves another purpose. As reported in Section *7.1 Substrate Issues* the waviness of the substrates' surfaces might lead to thermal barriers hindering the formation of bonds. Applying pressure during the bonding process not only evens out bent or saddle shaped substrates but also leads to better contact of wavy surfaces as soon as they are softened by the heating.

7.5 Sealing of Microfluidic Systems

As mentioned above, there are two main concepts for sealing microfluidic systems. A continuous layer in which the bond to be created is between the susceptor and the polymer slides (metal-plastic bonds) or the susceptor can be structured so that the bond is created between the polymer slides directly (plastic-plastic bonds).

Continuous layers are easier to realise and as more susceptor material is used the coupling with the electromagnetic field is better. On the other hand the metal susceptor is then part of the channel walls or in contact with functional parts of the chip. When using a structured susceptor these problems can be avoided. Also, plastic-plastic bonds are generally stronger than metal-plastic bonds. In addition the susceptor can be designed in a manner to keep the area of the chip containing channels and functional parts transparent. The drawback of this concept is the need for additional process steps to structure the susceptor.

Two sets of experiments were carried out to test the capabilities of both concepts. The aims of the experiments were to investigate the achievable bond strength for continuous layer susceptors and to test if induction heating can be used to seal microfluidic systems without channel distortion.

7.5.1 Continuous Layer Susceptor

It was first investigated whether continuous layer susceptors are feasible for induction bonding of microfluidic devices. The aim of this experiment was to investigate bond strength only, so the bonding of blank substrates without channels and ports was tested rather than bonding / sealing a working device.

7.5.1.1 Design of Experiment

PMMA substrates with a size of 40mm x 40mm x 4mm were coated with a 5µm thick nickel layer by electroplating (see Section *3.2.3.2 Electroplating*). It was attempted to bond these substrates onto blank PMMA slides using induction heating.

The original design of experiment called for nine sets of heating runs with varying settings for output current and heating time at each of three different working distances x. The values of the output current were chosen to be a minimum of 140A and a maximum of 490A (as these were the limitations of the equipment) and a value in between. As the heating rate depends superlinearly from the output current the third value was chosen to be around two thirds of the maximum value (i.e. 350A). In Section *5.1.2 Experimental Validation* nickel foil was heated to temperatures above 100℃ within 5s. Although being slightly thinner a higher heating rate was expected for the electroplated nickel as the susceptor area was much larger. Hence for the experiments described in this section the maximum heating time was 5s. The minimum value was chosen to be 1s and the medium heating time was set at 2.5s, slightly closer to the minimum value as the heating rate depends sublinearly on the heating time. In Section *5.1.2 Experimental Validation* there was hardly any heating measured for working distances above 40mm. Thus the values for working distance were chosen to be 15mm (as this was the minimum possible distance), 25mm and 50mm. The following three tables show the settings for the 27 individual experiments:

Table 7-4. Heating parameters at x = 15mm

Output current [A]	Time [s] 1	2,5	5
140	1	2	3
350	4	5	6
490	7	8	9

Table 7-5. Heating parameters at x = 25mm

Output current [A]	Time [s] 1	2,5	5
140	10	11	12
350	13	14	15
490	16	17	18

Table 7-6. Heating parameters at x = 50mm

Output current [A]	Time [s] 1	2,5	5
140	19	20	21
350	22	23	24
490	25	26	27

The polymer substrates were not stacked covering each other completely. The overlap on both sides was about 10mm as shown in Figure 7-16 so that the bonding area was 30mm x 40mm:

Figure 7-16. Overlapping substrates during bonding

The bonds were to be shear tested later but the jig for shear strength tests shown in Figure 7-8 was not yet available at the time of the experiments. The overlap configuration provided enough space for the clamps of the tensile test equipment.

7.5.1.2 Execution of the Experiments

As metal-plastic bonds are hard to realise the decision was made to enhance the bonding process by applying a high bonding pressure for all samples, rather than consider the pressure as another variable. For all experiments a force of about 3.6N was applied to the stack. With a bonding area of 30mm x 40mm that equals a pressure of 3kPa. This pressure was maintained for 60s during cooling.

The first set of experiments at a working distance of 15mm was the only one actually carried out. For all samples, except sample 1, some melting could be observed but a bond was only created for samples 3 to 9. As the bonds of sample 3 and 5 broke while handling the samples, the decision was made to test the remaining intact samples first, before proceeding with the experiment.

7.5.1.3 Testing the Samples

Shear strength tests as described in Section *3.1.5 Shear Strength Test* were carried out. To avoid a bending moment being imposed on the samples while being inserted into the tensile test machine, that might destroy the bonds, the samples were not fixed using the clamps of the testing equipment but a hole

was drilled in the middle of each overlap. Wires then were anchored in these holes used to apply the tensile force. Some bonds broke during the preparation so only samples six and eight could be actually tested. The measured shear strengths of these samples were 15kPa and 10kPa, respectively. After breaking the bond most of the nickel layer peeled off and only smaller pieces remained adhered to either substrate. Even with the smallest possible working distance it was not possible to create bonds properly and as heating rate decreases with larger distances the experiments were aborted at this point.

7.5.1.4 Conclusion

It appears that the polymer does not bond readily to metal and the bonds that are created are weak. To increase bond strength the metal surface could be roughened to provide keying for mechanical adhesion, but as the metal is coated onto one substrate it is quite complicated to increase the adhesion at that interface. As reported in Section *4.2 Experiments at Hüttinger Elektronik*, bonds directly between the polymer slides can reach high strengths so using structured susceptors to create polymer to polymer bonds seems to be the more promising approach.

7.5.2 Structured Susceptor

As the strength of plastic – plastic bonds had already been investigated the focus of the structured susceptor experiments was to demonstrate the ability of the process to seal channels and ports. Using the knowledge gained in previous sections a working microfluidic device was designed and manufactured, which could be sealed using induction heating.

7.5.2.1 Design of Experiment

The device was a simple mixer for fluids. Channels with a width and depth of approximately 300µm were laser machined into a 20mm x 40mm PMMA substrate (the platform) with a thickness of 2mm. The quality of the channel walls was not considered important. A closed loop susceptor with a track width of 1mm was designed, following the channels on both sides at a distance of 1mm. The susceptor was etched out of a 7.5µm thick Ni foil.

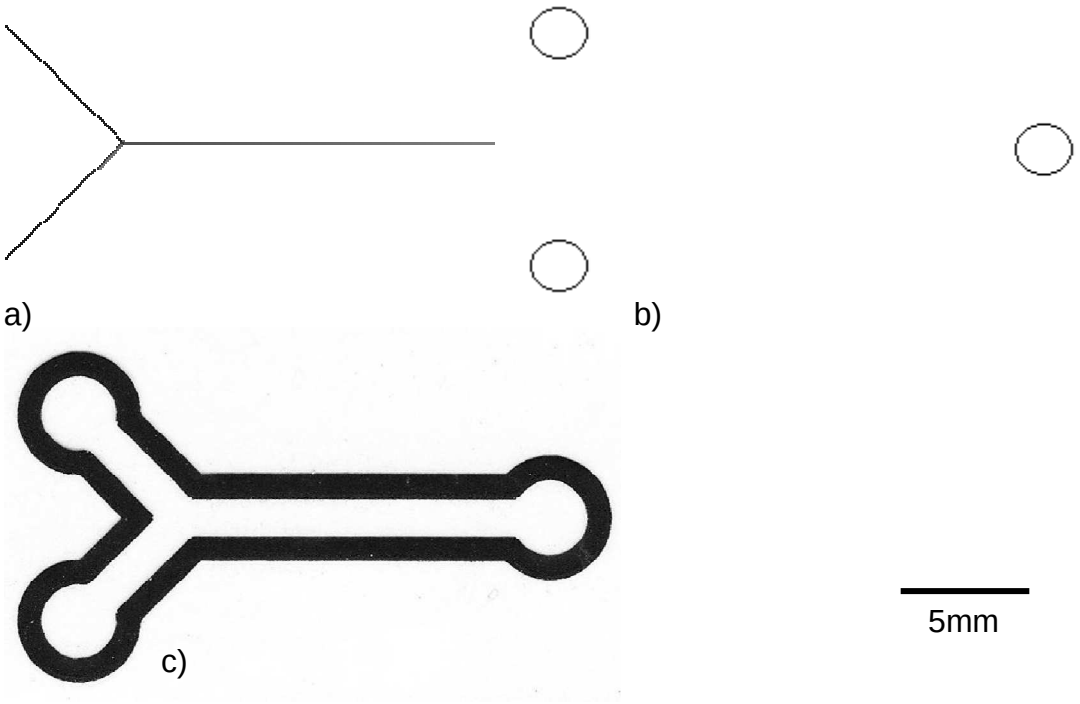

Figure 7-17. a) Design of microfluidic channels, b) hole pattern and c) design of susceptor

To access the channels three holes with a diameter of 2mm were laser machined into another substrate (the lid). To pass around the holes and seal the interconnection the susceptor bulged at all three ends as shown in Figure 7-17c. The track width of the susceptor was smaller than the width of the rings used for the pulsed heating tests. As such, the heating time was increased slightly to compensate. Four different sets of heating parameters were planned. The first two devices were bonded with three and four pulses of 6s. For the third device the four heating pulses were set at 7s each. For all devices a 5s cooling

phase followed each heating pulse. A final sample was bonded with four pulses of 7s followed by 3s cooling. Pressure was applied using weights to provide a bonding pressure of 22.4kPa for all samples.

7.5.2.2 Results & Discussion

The etched nickel susceptor was placed on the platform and the lid was put on top so that the holes covered the end of each channel. To ease the handling the platform was slightly moistened before placing the susceptor. Pressure was applied and the setup was bonded by pulsed heating.

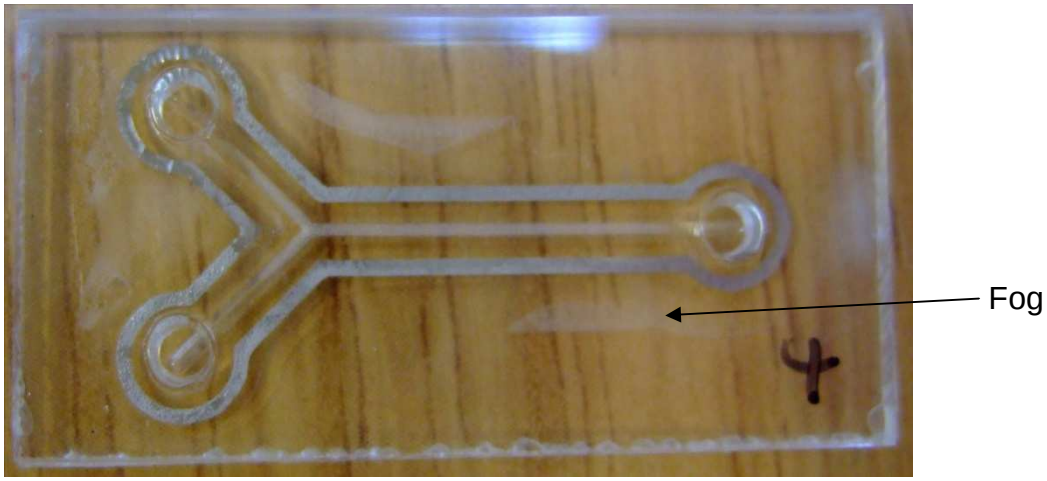

Figure 7-18. Microfluidic device, bonded with four pulses of 7s, followed by 5s cooling

Three samples were successfully produced (samples no. 1, 2 and 4). On the fourth (sample no. 3) the timer was accidently not set correctly so it was bonded with one pulse of 10s. The bond broke on this sample before it could be tested. Using a fifth device (sample no. 5) the experiment was then repeated with a correctly set timer. A ‘fog’ was visible between all bonded substrates, as shown in Figure 7-18. This was attributed to evaporated and recondensed moisture.

To test the devices a syringe was used to fill them with red ink from the lower left port. Although robust to handling the first two devices, which were bonded with three and four pulses of 6s followed by 5s cooling, were not sealed

properly. Small leaks were observed allowing the ink to be sucked between the two substrates as shown in Figure 7-19.

Figure 7-19. Leaking microfluidic device – Sample No. 2 (4 x 6s heating, 5s cooling)

The two devices bonded with 7s pulses showed good sealing at first, as shown in Figure 7-20:

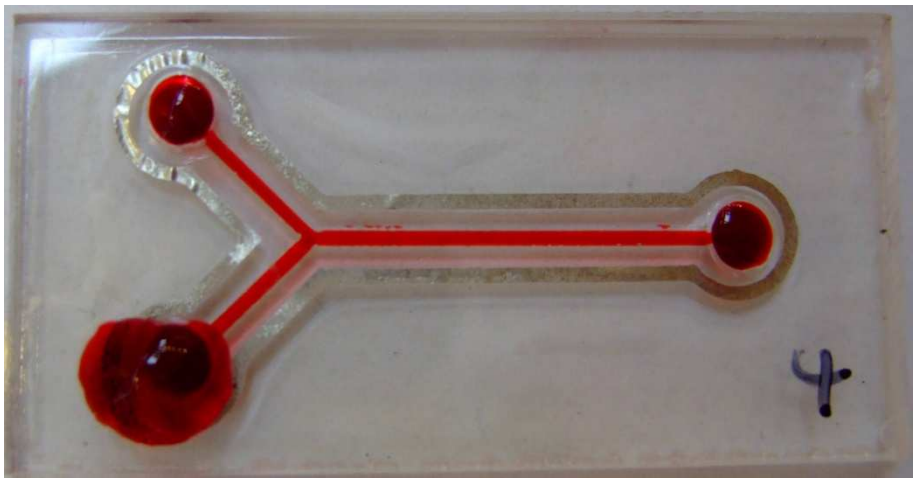

Figure 7-20. Microfluidic device filled with ink – Sample No. 4 (4 x 7s heating, 5s cooling)

However, after being left for more than five minutes the ink started to leak slightly (but still remained inside of the susceptor area). That means the channels were not perfectly sealed.

After testing the devices the channels of samples no. 4 and 5 were flushed by pushing water through the network using a syringe, removing the ink. The samples were then reused. After being filled with ink for a couple of minutes leakage occurred in both. The ink in sample no. 4 (bonded with 7s pulses followed by 5s cooling) was observed to leak further than before, reaching the area outside the susceptor on the second trial. The seal may have been disrupted while cleaning the device or remaining ink from the first run might have reduced the hydrophobicity of the PMMA, increasing the tendency for capillary flow.

To gain more information on the quality of the seal all samples were cut to make a cross section view:

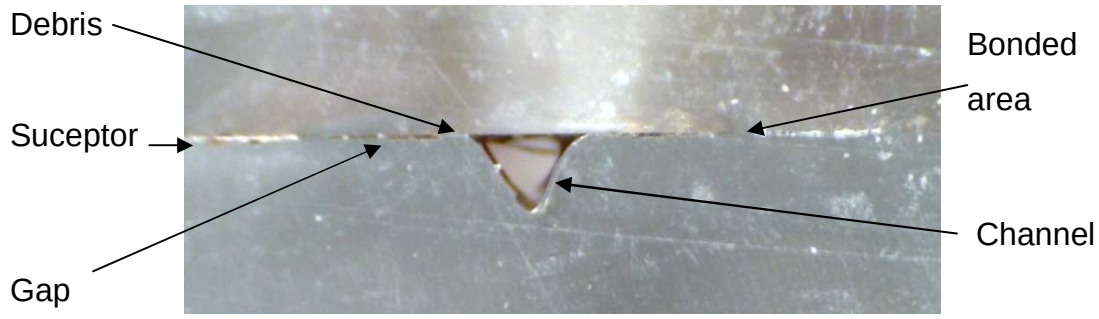

Figure 7-21. Cross section view of induction bonded device – Sample No. 4 (4 x 7s heating, 5s cooling)

As shown in Figure 7-21 a bond area was seen to have been created around the susceptor. Debris from the laser machining was also observed on both sides. This leads to a gap between the lid and platform, thus hindering the bond formation and sealing of the channels. A more controlled laser machining process or a different technique such as hot embossing to create the channels could be used to avoid creation of this gap. However, due to the debris the platform is in good contact with the lid in the area close to the channels. This might explain the delayed leakage described above.

Nevertheless the experiment shows that microfluidic devices can be sealed in seconds using induction bonding. However, placing the susceptor was not easy

and applying homogenous pressure during the bonding process was also tricky. Before being able to use the technique in large scale manufacture, these issues would have to be addressed.

7.5.3 Multi Layer Bond

High selectivity is one of the major advantages of the proposed induction bonding process. Not only is it possible to determine exactly the area were the heat is to be delivered but the several layers of a device can be sealed at once. Tests of this capability were carried out on a multilayer microfluidic device for blood separation, which was designed by Cranfield University in the context of the 3D-Mintegration project [96]. The design consists of five structured PMMA discs that form a microfluidic system when stacked as shown in Figure 7-22:

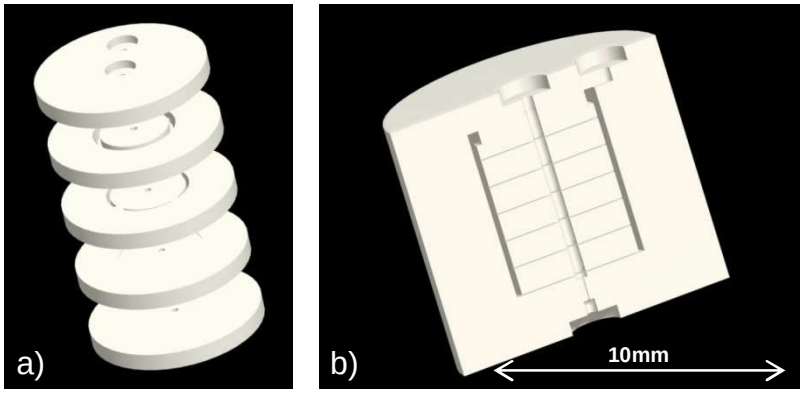

Figure 7-22. a) Polymer discs and b) Cross section view of microfluidic device designed by Cranfield University [96]

7.5.3.1 Design of Experiment

The susceptors were chosen to be rings etched out of 7.5µm thick nickel foil. The diameter of the PMMA discs was 10mm. To allow bonding on both sides of the susceptor ring and maintain a gap between the ring and the structured features, its inner and outer diameters were designed to be 6mm and 9mm, respectively.

To hold the discs in place while being able to apply pressure during bonding, a jig with plunger was designed as shown in Figure 7-23. Two versions of the jig were manufactured. One was made of a non-conductive material for induction bonding and another one was made of steel for the oven bonding as a comparison.

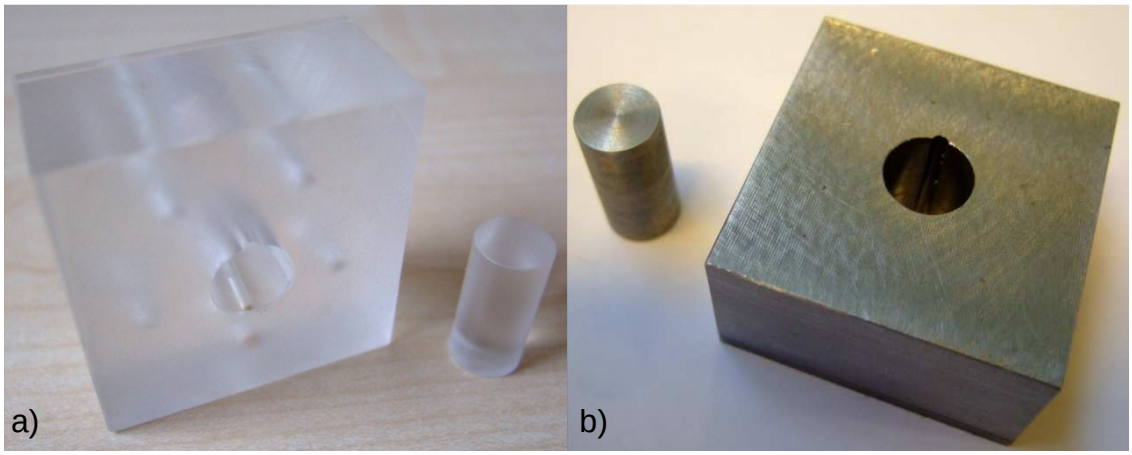

Figure 7-23. Jig with plunger a) made of PMMA and b) made of steel

The PMMA discs were put into the opening and a susceptor ring was placed between each. Using the plunger pressure could be applied during bonding. During induction bonding the pressure was around 170kPa. Pressure during oven bonding could not be measured as pressure was applied by an uncalibrated clamp with screws.

Higher heating rates had to be considered, as there were four susceptors close to each other. Three samples were bonded using different parameters. First a stack of discs was bonded with two pulses of 5s, each followed by 10s cooling (stack 1). Two other stacks were bonded then with three pulses of 1s and 2s followed by 7s cooling each (stacks 2 and 3).

For thermal bonding the setup with the steel jig was placed in a cold vacuum oven. The oven was then heated to 105℃. This took 60min. The temperature was kept constant for 20min before the oven was switched off. The setup was

allowed to cool down for another 20min until the discs were rigid enough to be removed.

For both samples cross-sectional views were prepared to investigate the bond area. Testing the sealing was not possible as no connector was available.

7.5.3.2 Results & Discussion

The heating rate of the induction-bonded sample with two pulses of 5s (stack 1) was found to be too high, such that the polymer burned. The sample bonded with 1s pulses (stack 2) showed good bond strength between the discs close to the inductor coil, but the upper disc fell off while removing the system from the jig. The third sample (stack 3, 2s pulses) showed good bond strength over the whole stack but bubbles appeared in the bottom discs (Figure 7-24):

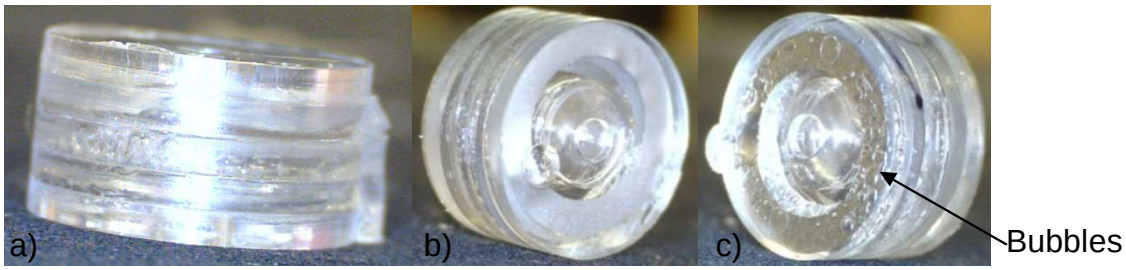

Figure 7-24. Induction bonded stack of polymer discs, a) side, b) top and c) bottom – Stack 3 (3 x 2s heating, 7s cooling)

As shown in Figure 7-24b the susceptor rings were not centrally aligned. Again, the issues of placing the electromagnetic susceptor have to be addressed before being able to use the process industrially.

During cutting stack 3 for examining the cross-sectional area, the stack broke. However, it can be seen in Figure 7-25 that the small gap in the middle between each disc, which is part of the design (see Figure 7-22b) has been successfully maintained and has not collapsed.

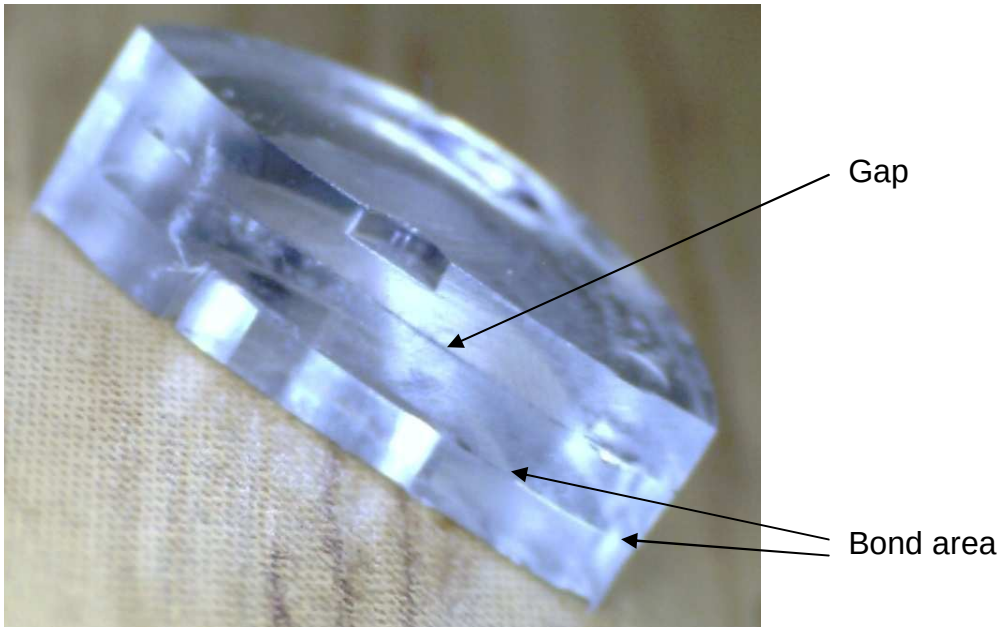

Figure 7-25. Cross section view of induction bonded sample – Stack 3

All discs of the oven-bonded sample were joined successfully. As no susceptor material was introduced the system's middle channel is clearly visible as shown in Figure 7-26.

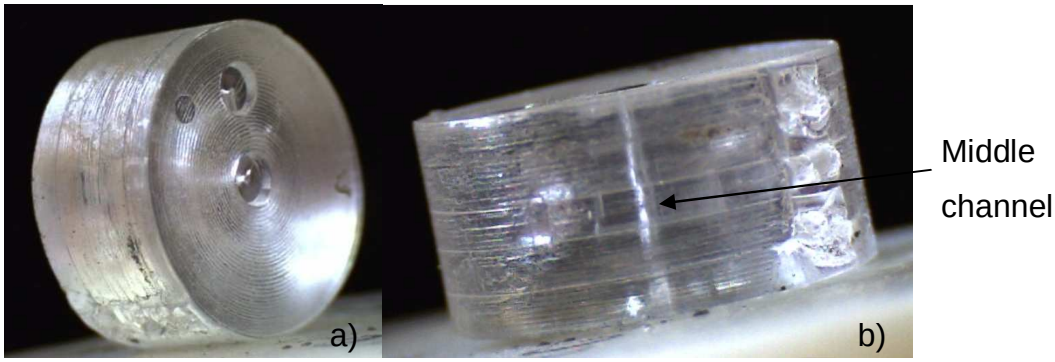

Figure 7-26. Oven bonded sample, a) top view and b) view from side

The inspection of the cross-sectional area revealed that the whole gap between the discs had collapsed as shown in Figure 7-27:

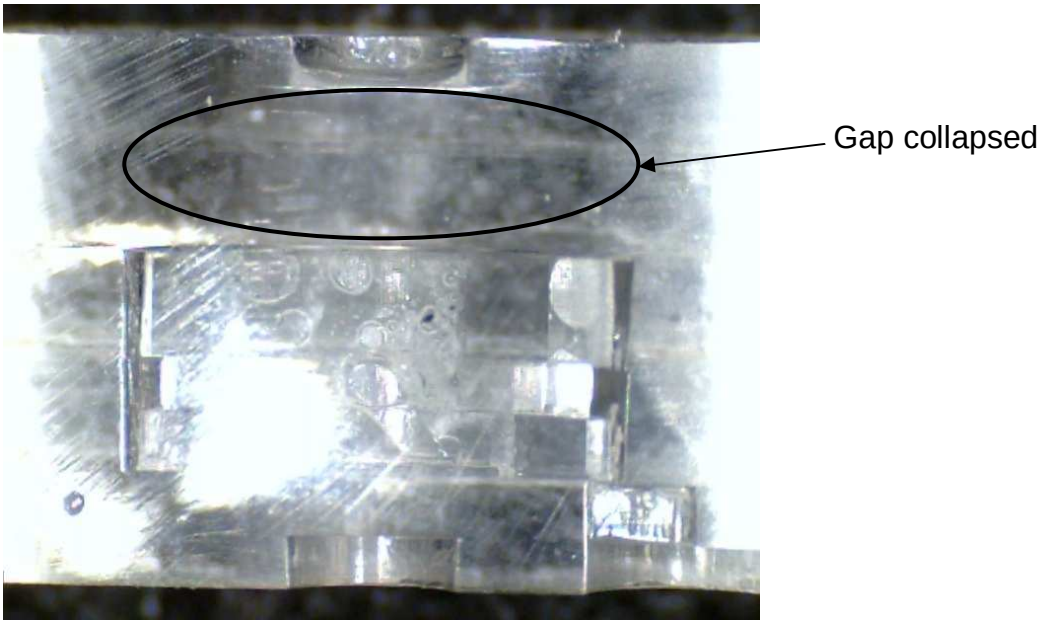

Figure 7-27. Cross section view of oven bonded sample

Thermo-compression bonding is known to have a narrow processing window which would require some effort to find.

It can be concluded that induction bonding appears to be feasible for multi layer bonding of microfluidic devices. During the experiments a flat helix coil was used which lead to a heat concentration in the areas closer to the coil. To get more homogenous heat dissipation the stack could be placed in the middle of a cylindrical coil or in between two flat coils. High selectivity helps to avoid inadvertently destroying features but it is critical to find an efficient technique to place the susceptor. Total bonding time was less than 30s compared to the 100min needed for oven bonding.

8 Conclusions & Future Work

The work presented in this thesis has shown that it is possible to seal microfluidic devices using low frequency induction bonding. It is not recommended to use whole layer susceptors, but structured susceptors showed very good results in terms of bond strength and sealing quality.

Analytical equations describing the heating of a susceptor in an induction field were derived for a simplified situation, to provide the basis for process optimisation and design rules for the low frequency induction heating (LFIH) plastics joining technique. The equations predict a sublinear behaviour of heat generation against heating time, non-linear decrease with increasing working distance and superlinear increase with increasing generator coil current. The predictions were consistent with the results of experiments and simulations. It was found that the model cannot be used to predict exact temperatures but it correctly describes the effect of the heating parameters on the heating rate.

The shape and area of susceptors were also investigated with respect to their influence on the heating rate for low frequency induction bonding. Circular shaped susceptors have the best efficiency and it is important that the susceptors form a closed circuit.

Cooling effects were considered in association with the heating. Those effects do not seem to have a major impact on the heating rate at the temperature regime used during this project (< 250℃).

With good coupling, the response time of the heating process was around 2s. This observation is useful for controlling the bond process (pulsed heating).

Bond parameters such as bonding pressure and pulsed heating were investigated for their effect on the quality of the bond of induction bonded PMMA substrates. Higher bonding pressure was identified as increasing bond

strength and allowing the reduction of heating time and thus the reduction of melt zone width. The use of heating pulses instead of continuous heating also reduced the dimensions of melt zones, while providing good bond strength and high leakage pressure. Such bonded samples withstood an air pressure of 590kPa without leaking. The size of the HAZ was found to be negligible.

To summarise the findings, the following guidelines were drawn up for the design of susceptors and process optimisation:

- Materials with low resistivity perform better;
- For very thin susceptors the effect of permeability on the heating rate is negligible;
- The cross-sectional area of the susceptor should be as large as possible to reduce resistance;
- The thickness of the susceptor should be of the order of the dimensions of the penetration depth or smaller to increase homogeneity of heat dissipation;
- The shape of the susceptor should follow the shape of the inductor coil, or vice-versa, to increase homogeneity of heat dissipation;
- The susceptor should form a closed circuit;
- Higher bonding pressure leads to stronger bonds and allows reduced heating times;
- Pulsed heating performs better in terms of limited melt area and good bond strength.

8.1 Comparison with Other Techniques & Issues to Resolve

Compared to other sealing techniques induction bonding has many advantages. If the susceptor is designed to be encapsulated during bonding, no additional material will be in contact with the processing liquids as might happen with adhesive bonding. Also, a possible blockage of channels can be easily avoided by adjusting the bond parameters to limit the melt area width. High selectivity

leads to bonds only in the desired area in comparison with thermal bonding, but the susceptor has to be designed and positioned correctly. Multi layer bonding is possible. The setup is simple and easy to use and no special lab or protective chamber is needed as it is for example for microwave bonding. Quick bonding times and very good repeatability are possible, making this technique ideal for prototyping and a promising alternative for large-scale manufacture.

But there are drawbacks as well. Introducing additional materials leads to additional process steps. Also, the susceptor was placed manually during this project and that is not feasible for mass manufacture. It is not possible to estimate the exact amount of temperature being generated in the workpiece, so for every design a set of experiments has to be run in order to determine the best bond parameters.

These points are summarised in Table 8-1:

Table 8-1. Advantages and disadvantages of induction bonding

Advantages	Disadvantages
No additional material in contact with processing liquids	Concept of manufacturing susceptor needed
No blockage of channels	Additional process steps
High selectivity	Exact temperature not predictable
Multi layer bond possible	
Simple and easy to use setup	
No extra chamber / lab needed	
Very rapid bonding process	
Very good repeatability	
Ideal for mass manufacture	

To be able to use the technique efficiently a concept of manufacturing the susceptor has to be found to allow precise alignment of complex designs. This additional process step has to be feasible for mass manufacture. Instead of moistening the surface of the device, as it was done during this project,

electrostatic effects can be used to hold the susceptor on place. A reel to reel feed of metal foil that is stamped out onto the surface of the device also might be a workable solution. Another concept might be coating the whole device with a metal layer and structuring that layer by etching or laser machining. During this project an electroplated nickel layer was structured successfully using a fibre laser. Unfortunately the adhesion of the nickel layer was not very good so only larger structures were possible to realise. The idea of filling laser machined channels with metal powder was also put to the test. Channels with a width and depth of 1mm were filled with nickel powder but it was not possible to heat the powder sufficiently. This might be due to oxidisation of the nickel particles which may be avoided by handling the powder in a nitrogen atmosphere.

A concept to apply pressure more homogenously is also needed. The workbench designed for this project is sufficient for testing the technique but in order to improve the bond quality the application of pressure must be more controllable. For large-scale manufacture the working area must be designed in such a way as to allow high throughput.

If these issues can be addressed appropriately, low frequency induction heating is an ideal technique for the sealing / packaging of microfluidic systems in large-scale manufacture.

8.2 Extension of the Process to Interconnection

When sealed the microfluidic device has to be connected to the outer world. The interconnection was not realised during this project, however, it is not impossible. Using induction bonding there are two main concepts to achieve this: the susceptor can be placed at the connector tube's tip or integrated in the lid of the microfluidic device (see Figure 8-1). The integrated susceptor would have the advantage that the tubes used for interconnection do not need special preparation.

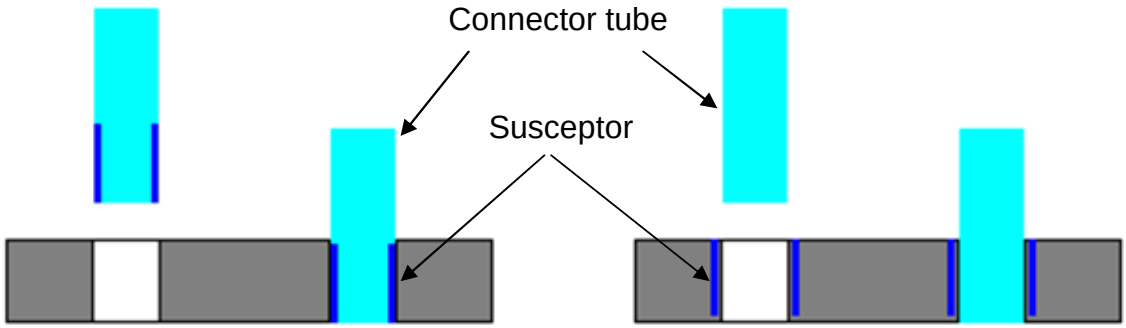

Figure 8-1. Possible design for a) susceptor on connector tube and b) integrated susceptor

Some issues have to be addressed to be able to utilise induction bonding for interconnecting microfluidic devices. The susceptor has to be designed / placed in such a way as to allow plastic – plastic bonds and some sort of pressure has to be applied during bonding to gain sufficient bond strength. The latter could be realised by using tubes with a diameter slightly larger than the port or by inflating the tubes after inserting them.

Another problem is the choice of materials. Very often the tubes are made of Teflon, but adhesion between Teflon and PMMA is not very good. To be more flexible in the choice of materials a heat shrink ferrule containing the susceptor could be part of the microfluidic port. After application of heat the ferrule forms a pressure seal around the connector tube holding it in place.

For connecting different microfluidic chips in a modular system, induction heating would be an ideal solution as the approach is not different to the sealing of microfluidic platforms.

Possible solutions for connecting microfluidic systems to the outer world using induction bonding are manifold. Certain issues have to be addressed but the technique could lead to a rapid, low pitch interconnection method, which would be feasible for mass manufacture as well as use in small medical labs and hospitals, where the microfluidic chips are used.

When introducing a new material to a system, as it is done with susceptors for induction bonding, it is desirable to functionalise that material even after it has served its main purpose. The susceptor can be designed in such a way as to be of use after the bonding process.

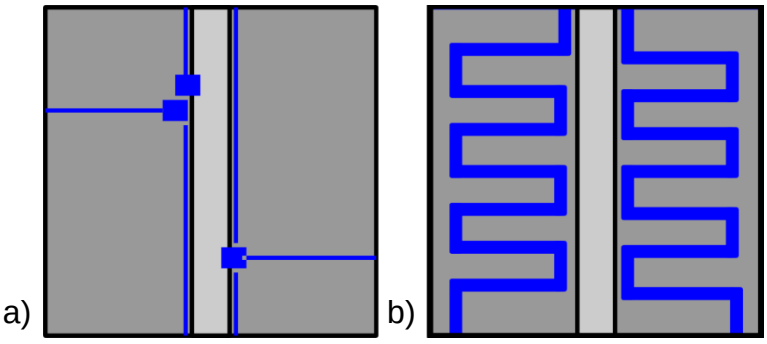

Figure 8-2. Functionalised susceptor: a) as electrical connector and b) as heating meander

Figure 8-2 shows two possible designs. The susceptor could work as an electrical connector in contact with or being sealed from the processing liquid. Also, it could be designed in form of a heating meander to deliver heat for specific areas of the microfluidic systems.

Different materials could be used for different applications. But as said above: it is critical to find a reliable and feasible way of placing the susceptor.

References

[1] J. Wang, "Lab-on-valve mesofluidic analytical system and its perspectives as a “world-to-chip” front-end," Analytical and Bioanalytical Chemistry, vol. 381, pp. 809-811, 02/01. 2005.

[2] P. Abgrall and A. M. Gué, "Lab-on-chip technologies: making a microfluidic network and coupling it into a complete microsystem - a review," J Micromech Microengineering, vol. 17, pp. R15-R49, 2007.

[3] D. R. Reyes, D. Iossifidis, P. A. Auroux and A. Manz, "Micro total analysis systems. 1. Introduction, theory, and technology," Anal. Chem., vol. 74, pp. 2623-2636, 06/02. 2002.

[4] Y. Peles, V. T. Srikar, T. S. Harrison, C. Protz, A. Mracek and S. M. Spearing, "Fluidic packaging of microengine and microrocket devices for high-pressure and high-temperature operation," Microelectromechanical Systems, Journal of, vol. 13, pp. 31-40, 2004.

[5] C. H. Lin, G. B. Lee, L. M. Fu and S. H. Chen, "Integrated optical-fiber capillary electrophoresis microchips with novel spin-on-glass surface modification," Biosensors and Bioelectronics, vol. 20, pp. 83-90, 07/04. 2004.

[6] C. H. Lin, G. B. Lee, Y. H. Lin and G. L. Chang, "A fast prototyping process for fabrication of microfluidic systems on soda-lime glass," J Micromech Microengineering, vol. 11, pp. 726-732, 2001.

[7] C. G. J. Schabmueller, M. Koch, A. G. R. Evans and A. Brunnschweiler, "Design and fabrication of a microfluidic circuitboard," J Micromech Microengineering, vol. 9, pp. 176-179, 1999.

[8] V. L. Spiering, J. N. van der Moolen, G. J. Burger and A. van den Berg, "Novel microstructures and technologies applied in chemical analysis techniques," in Solid State Sensors and Actuators, 1997. TRANSDUCERS '97 Chicago., 1997 International Conference on, 1997, pp. 511-514 vol.1.

[9] W. van der Wijngaart, H. Andersson, P. Enoksson, K. Noren and G. Stemme, "The first self-priming and bi-directional valve-less diffuser micropump for both liquid and gas," in Micro Electro Mechanical Systems, 2000. MEMS 2000. the Thirteenth Annual International Conference on, 2000, pp. 674-679.

[10] S. Garst, M. Schuenemann, M. Solomon, M. Atkin and E. Harvey, "Fabrication of multilayered microfluidic 3D polymer packages," in Electronic Components and Technology Conference, 2005. Proceedings. 55th, 2005, pp. 603-610 Vol. 1.

[11] Z. F. Wang, R. T. Tjeung, N. De Rooij and S. H. Ng, "Process issues for a multi-layer microelectrofluidic platform," Symposium on Design, Test, Integration and Packaging of MEMS/MOEMS - DTIP'06, 04/06. 2006.

[12] D. C. Duffy, J. C. McDonald, O. J. A. Schueller and G. M. Whitesides, "Rapid Prototyping of Microfluidic Systems in Poly(dimethylsiloxane)," Anal. Chem., vol. 70, pp. 4974-4984, 1998.

[13] S. Tuomikoski, "Fabrication Of SU-8 Microstructures For Analytical Microfluidic Applications," 2007.

[14] M. A. Roberts, J. S. Rossier, P. Bercier and H. Girault, "UV Laser Machined Polymer Substrates for the Development of Microdiagnostic Systems," Anal. Chem., vol. 69, pp. 2035-2042, 1997.

[15] J. R. Anderson, D. T. Chiu, R. J. Jackman, O. Cherniavskaya, J. C. McDonald, H. Wu, S. H. Whitesides and G. M. Whitesides, "Fabrication of

Topologically Complex Three-Dimensional Microfluidic Systems in PDMS by Rapid Prototyping," Anal. Chem., vol. 72, pp. 3158-3164, 2000.

[16] D. Armani, C. Liu and N. Aluru, "Re-configurable fluid circuits by PDMS elastomer micromachining," in Micro Electro Mechanical Systems, 1999. MEMS '99. Twelfth IEEE International Conference on, 1999, pp. 222-227.

[17] C. H. Lin, C. H. Chao and C. W. Lan, "Low azeotropic solvent for bonding of PMMA microfluidic devices," Sensors and Actuators B: Chemical, vol. 121, pp. 698-705, 02/07. 2007.

[18] S. Lai, X. Cao and L. J. Lee, "A Packaging Technique for Polymer Microfluidic Platforms," Anal. Chem., vol. 76, pp. 1175-1183, 2004.

[19] J. Oberhammer and G. Stemme, "BCB contact printing for patterned adhesive full-wafer bonded 0-level packages," Microelectromechanical Systems, Journal of, vol. 14, pp. 419-425, 2005.

[20] B. Bilenberg, T. Nielsen, B. Clausen and A. Kristensen, "PMMA to SU-8 bonding for polymer based lab-on-a-chip systems with integrated optics," J Micromech Microengineering, vol. 14, pp. 814-818, 2004.

[21] K. W. Oh, A. Han, S. Bhansali and C. H. Ahn, "A low-temperature bonding technique using spin-on fluorocarbon polymers to assemble microsystems," J Micromech Microengineering, vol. 12, pp. 187-191, 2002.

[22] Z. Chen, Y. Gao, J. Lin, R. Su and Y. Xie, "Vacuum-assisted thermal bonding of plastic capillary electrophoresis microchip imprinted with stainless steel template," Journal of Chromatography A, vol. 1038, pp. 239-245, 06/04. 2004.

[23] G. Chen, J. Li, S. Qu, D. Chen and P. Yang, "Low temperature bonding of poly(methylmethacrylate) electrophoresis microchips by in situ polymerisation," Journal of Chromatography A, vol. 1094, pp. 138-147, 11/05. 2005.

[24] R. T. Kelly and A. T. Woolley, "Thermal Bonding of Polymeric Capillary Electrophoresis Microdevices in Water," Anal. Chem., vol. 75, pp. 1941-1945, 2003.

[25] D. Sparks, G. Queen, R. Weston, G. Woodward, M. Putty, L. Jordan, S. Zarabadi and K. Jayakar, "Wafer-to-wafer bonding of nonplanarized MEMS surfaces using solder," J Micromech Microengineering, vol. 11, pp. 630-634, 2001.

[26] J. Lai, X. Chen, X. Wang, X. Yi and S. Liu, "Laser bonding and packaging of plastic microfluidic chips," in Electronic Packaging Technology Proceedings, 2003. ICEPT 2003. Fifth International Conference on, 2003, pp. 168-171.

[27] R. Witte, H. J. Herfurth and I. Bauer, "Microjoining of dissimilar materials for optoelectronic and biomedical applications," vol. 4979, pp. 233, 01/25/. 2003.

[28] A. A. Yussuf, I. Sbarski, J. Hayes and M. Solomon, "Sealing and Bonding Techniques for Polymer-Based Microfluidic Devices," pp. 269-275, 2001.

[29] J. I. Rotheiser, Joining of Plastics: Handbook for Designers and Engineers. ,1st ed.München; Wien: Carl Hanser Verlag, 1999,

[30] H. Kuckert, C. Born, G. Wagner and D. Eifler, "Helium-tight Sealing of Glass with Metal by Ultrasonic Welding," Advanced Engineering Materials, vol. 3, pp. 903-905, 2001.

[31] A. Y. Hui, G. Wang, B. Lin and W. T. Chan, "Microwave plasma treatment of polymer surface for irreversible sealing of microfluidic devices," Lab Chip, vol. 5, pp. 1173-1177, 10/02. 2005.

[32] P. Miller, I. Sbarski, A. Taube and D. Nicolau, "Sealing of Microfluidic Devices using Microwave Technology," pp. 243-247, 2001.

[33] N. K. Budraa, H. W. Jackson, M. Barmatz, W. T. Pike and J. D. Mai, "Low pressure and low temperature hermetic wafer bonding using microwave heating," in Micro Electro Mechanical Systems, 1999. MEMS '99. Twelfth IEEE International Conference on, 1999, pp. 490-492.

[34] K. F. Lei, S. Ahsan, N. K. Budraa, W. J. Li and J. D. Mai, "Microwave bonding of polymer-based substrates for potential encapsulated micro/nanofluidic device fabrication," Sensors and Actuators A: Physical, vol. 114, pp. 340-346, 09/04. 2004.

[35] A. A. Yussuf, J. Hayes, M. Solomon and I. Sbarski, "Microfluidic Sealing," WO/2004/092048, 28 Oct 2004, 2004.

[36] A. A. Yussuf, I. Sbarski, M. Solomon and J. Hayes, "Sealing of polymeric-microfluidic devices by using high frequency electromagnetic field and screen printing technique," Journal of Materials Processing Technology, vol. 189, pp. 401-408, 6 July 2007. 2007.

[37] H. A. Yang, M. Wu and W. Fang, "Localized induction heating solder bonding for wafer level MEMS packaging," J Micromech Microengineering, vol. 15, pp. 394-399, 2005.

[38] W. Suwanwatana, S. Yarlagadda and J. W. Gillespie, "Hysteresis heating based induction bonding of thermoplastic composites," Composites Science and Technology, vol. 66, pp. 1713-1723, 09/06. 2006.

[39] W. Suwanwatana, S. Yarlagadda and J. W. Gillespie, "Influence of particle size on hysteresis heating behavior of nickel particulate polymer films," Composites Science and Technology, vol. 66, pp. 2825-2836, 12/06. 2006.

[40] W. Suwanwatana, S. Yarlagadda and J. W. Gillespie, "An investigation of oxidation effects on hysteresis heating of nickel particles," J. Mater. Sci., vol. 38, pp. 565-573, 02/01. 2003.

[41] H. A. Yang, C. W. Lin, C. Y. Peng and W. Fang, "On the selective magnetic induction heating of micron scale structures," J Micromech Microengineering, vol. 16, pp. 1314-1320, 2006.

[42] Y. A. Monovoukas, "Induction heating of loaded materials," US 5378879, 3 Jan 1995, 1995.

[43] J. Liu, C. Hansen and S. R. Quake, "Solving the "World-to-Chip" Interface Problem with a Microfluidic Matrix," Anal. Chem., vol. 75, pp. 4718-4723, 2003.

[44] S. B. Schaevitz, T. Boone and T. O. Bjornson, "Efficient microfluidic sealing," US 6908594 B1, 21 Jun 2005, 2005.

[45] C. Gonzalez, S. D. Collins and R. L. Smith, "Fluidic interconnects for modular assembly of chemical microsystems," in Solid State Sensors and Actuators, 1997. TRANSDUCERS '97 Chicago., 1997 International Conference on, 1997, pp. 527-530 vol.1.

[46] B. L. Gray, S. D. Collins and R. L. Smith, "Interlocking mechanical and fluidic interconnections for microfluidic circuit boards," Sensors and Actuators A: Physical, vol. 112, pp. 18-24, 4/15. 2004.

[47] T. S. J. Lammerink, V. L. Spiering, M. Elwenspoek, J. H. J. Fluitman and A. van den Berg, "Modular concept for fluid handling systems. A demonstrator micro analysis system," in Micro Electro Mechanical Systems, 1996, MEMS '96, Proceedings. 'an Investigation of Micro Structures, Sensors, Actuators, Machines and Systems'. IEEE, the Ninth Annual International Workshop on, 1996, pp. 389-394.

[48] P. F. Man, D. K. Jones and C. H. Mastrangelo, "Microfluidic plastic interconnects for multibioanalysis chip modules," in 1997, pp. 196-200.

[49] T. Liu, S. Masood, P. Iovenitti and E. Harvey, "Development of Packaging Systems and Interconnects for Microfluidics Applications," Packaging India, vol. 40, pp. 9-14, 2007.

[50] E. Igata, M. Arundell, H. Morgan and J. M. Cooper, "Interconnected reversible lab-on-a-chip technology," Lab Chip, vol. 2, pp. 65-69, 05/02. 2002.

[51] T. Hasegawa and K. Ikuta, "Novel interconnection for micro fluidic devices," in *Micromechatronics and Human Science, 2002. MHS 2002. Proceedings of 2002 International Symposium on,* 2002, pp. 169-174.

[52] P. C. Galambos and G. L. Benavides, "Electrical and fluidic packaging of surface micromachined electromicrofluidic devices," in 2000, pp. 186-193.

[53] C. K. Fredrickson and Z. H. Fan, "Macro-to-micro interfaces for microfluidic devices," *Lab Chip,* vol. 4, pp. 526-533, 2004.

[54] A. A. S. Bhagat, P. Jothimuthu, A. Pais and I. Papautsky, "Re-usable quick-release interconnect for characterization of microfluidic systems," *J Micromech Microengineering,* vol. 17, pp. 42-49, 2007.

[55] Z. Yang and R. Maeda, "Socket with built-in valves for the interconnection of microfluidic chips to macro constituents," *Journal of Chromatography A,* vol. 1013, pp. 29-33, 2003.

[56] C. H. Chiou and G. B. Lee, "Minimal dead-volume connectors for microfluidics using PDMS casting techniques," *J Micromech Microengineering,* vol. 14, pp. 1484-1490, 2004.

[57] J. H. Tsai and L. Lin, "Micro-to-macro fluidic interconnectors with an integrated polymer sealant," *J Micromech Microengineering,* vol. 11, pp. 577-581, 2001.

[58] S. Li and S. Chen, "Polydimethylsioxane fluidic interconnects for microfluidic systems," *Advanced Packaging, IEEE Transactions on [See also Components, Packaging and Manufacturing Technology, Part B: Advanced Packaging, IEEE Transactions on],* vol. 26, pp. 242-247, 2003.

[59] E. Meng, S. Wu and Y. C. Tai, "Silicon couplers for microfluidic applications," *Fresenius J. Anal. Chem.,* vol. 371, pp. 270-275, 09/01. 2001.

[60] B. L. Gray, D. Jaeggi, N. J. Mourlas, B. P. van Drieënhuizen, K. R. Williams, N. I. Maluf and G. T. A. Kovacs, "Novel interconnection technologies for integrated microfluidic systems," *Sensors and Actuators A: Physical,* vol. 77, pp. 57-65, 9/28. 1999.

[61] G. T. A. Kovacs, "Micromachined fluidic coupler," US 5890745, 6 Apr 1999, 1999.

[62] C. R. Friedrich, R. R. K. Avula and S. Gugale, "A fluid microconnector seal for packaging applications," *J Micromech Microengineering,* vol. 15, pp. 1115-1124, 2005.

[63] E. S. Lee, D. Howard, E. Liang, S. D. Collins and R. L. Smith, "Removable tubing interconnects for glass-based micro-fluidic systems made using ECDM," *J Micromech Microengineering,* vol. 14, pp. 535-541, 2004.

[64] T. J. Yao, S. Lee, W. Fang and Y. C. Tai, "Micromachined rubber O-ring micro-fluidic couplers," in *Micro Electro Mechanical Systems, 2000. MEMS 2000. the Thirteenth Annual International Conference on,* 2000, pp. 624-627.

[65] Y. C. Tai and T. J. Yao, "Micromachined rubber O-ring microfluidic couplers," US 6698798 B2, 2 Mar 2004, 2004.

[66] A. Puntambekar and C. H. Ahn, "Self-aligning microfluidic interconnects for glass- and plastic-based microfluidic systems," *J Micromech Microengineering,* vol. 12, pp. 35-40, 2002.

[67] A. V. Pattekar and M. V. Kothare, "Novel microfluidic interconnectors for high temperature and pressure applications," *J Micromech Microengineering,* vol. 13, pp. 337-345, 2003.

[68] V. Saarela, S. Franssila, S. Tuomikoski, S. Marttila, P. Östman, T. Sikanen, T. Kotiaho and R. Kostiainen, "Re-usable multi-inlet PDMS fluidic connector," *Sensors and Actuators B: Chemical,* vol. 114, pp. 552-557, 03/06. 2006.

[69] A. M. Christensen, D. A. Chang-Yen and B. K. Gale, "Characterization of interconnects used in PDMS microfluidic systems," *J Micromech Microengineering,* vol. 15, pp. 928-934, 2005.

[70] T. Pan, A. Baldi and B. Ziaie, "A reworkable adhesive-free interconnection technology for microfluidic systems," *Microelectromechanical Systems, Journal of,* vol. 15, pp. 267-272, 2006.

[71] G. L. Benavides, P. C. Galambos, J. A. Emerson, K. A. Peterson, R. K. Giunta, D. L. Zamora and R. D. Watson, "Packaging of electro-microfluidic device," US 6548895 B1, 15 Apr 2003, 2003.

[72] Upchurch, "Micro fluidic interconnects," *Technical Resources,* pp. 148-158, 2007.

[73] D. P. Webb, D. A. Hutt, N. Hopkinson, P. J. Palmer and P. P. Conway, "Integration and Packaging of Microsystems by Polymer Overmoulding,"

Electronics Systemintegration Technology Conference, 2006. 1st, vol. 1, pp. 567-574, 2006.

[74] D. P. Webb, C. C. Hsu, D. A. Hutt, N. Hopkinson, P. P. Conway and P. J. Palmer, "Polymer Overmoulding for Microfluidic Device Packaging and System Integration," *Polymers and Adhesives in Microelectronics and Photonics, Polytronic, 2005. Polytronic 2005. 5th International Conference on,* pp. 134-139, 2005.

[75] G. Dahake, "Precision Induction Heating With Advanced Solid State Technology," *Ameritherm Inc.,* 01/99. 1999.

[76] J. Callebaut, "Induction Heating," *Power Quality & Utilisation Guide,* 02/07. 2007.

[77] Anonymous "Induction Heating Technology," *TechCommentary,* vol. 2, 1993.

[78] C. Tudbury, "Electromagnetics in induction heating," *Magnetics, IEEE Transactions on,* vol. 10, pp. 694-697, 1974.

[79] S. C. Chen, W. R. Jong, Y. J. Chang, J. A. Chang and J. C. Cin, "Rapid mold temperature variation for assisting the micro injection of high aspect ratio micro-feature parts using induction heating technology," *J Micromech Microengineering,* vol. 16, pp. 1783-1791, 2006.

[80] G. Dahake, "Heat Staking: Inserting Metal into Plastic," *Ameritherm Inc.,*

[81] R. J. Nichols, D. P. LaMarca and B. Agosto, "Performance of Susceptor Materials in High Frequency Magnetic Fields," *Proc. of ANTEC, SPE,* 2006.

[82] Cheltenham Induction Heating Ltd, "Tamper-Evident Cap Sealing," 2006.

[83] W. C. Moreland, "The Induction Range: Its Performance and Its Development Problems," *Industry Applications, IEEE Transactions on,* vol. IA-9, pp. 81-85, 1973.

[84] Fairchild Semiconductor, "Induction Heating System Topology Review," 07/00. 2000.

[85] H. A. Yang, C. W. Lin and W. Fang, "Wafer level self-assembly of microstructures using global magnetic lifting and localized induction welding," *J Micromech Microengineering,* vol. 16, pp. 27-32, 2006.

[86] Y. W. Yi and C. Liu, "Magnetic actuation of hinged microstructures," *Microelectromechanical Systems, Journal of,* vol. 8, pp. 10-17, 1999.

[87] K. Thompson, Y. B. Gianchandani, J. Booske and R. F. Cooper, "Direct silicon-silicon bonding by electromagnetic induction heating," *Microelectromechanical Systems, Journal of,* vol. 11, pp. 285-292, 2002.

[88] H. Kuchling, *Taschenbuch Der Physik.* ,17th ed.München; Wien: Carl Hanser Verlag, Fachbuchverlag Leipzig, 2001,

[89] R. E. Haimbaugh, "Theory of heating by induction," in *Practical Induction Heat Treating* ASM International, Ed. Ohio: 2001, pp. 5-18.

[90] J. Davis and P. Simpson, *Induction Heating Handbook.* London; New York: McGraw-Hill, 1979,

[91] H. Stöcker, *Taschenbuch Der Physik.* ,5th ed.Frankfurt am Main: Wissenschaftlicher Verlag Harry Deutsch, 2004,

[92] S. Zinn and S. L. Semiatin, "Coil design and fabrication: basic design and modifications," *Heat Treating,* pp. 32-41, 06/88. 1988.

[93] M. J. Madou, *Fundamentals of Microfabrication: The Science of Miniaturization.* ,2nd ed.Boca Raton; London; New York; Washington, D.C.: CRC Press LLC, 2002,

[94] The Sabreen Group, "Preparing Plastics for Painting,"

[95] W. MovGP0, "Biot-Savart-Gesetz," pp. 1, 08.03.2007. 2007.

[96] S. Marson, U. Attia, D. M. Allen, P. Tipler, T. Jin, J. Hedge and J. R. Alcock, "Reconfigurable Micro-mould for the Manufacture of Truly 3D Polymer Microfluidic Devices," *Proceedings of the 19th CIRP Design Conference – Competitive Design, Cranfield University,* pp. 343-346, 31 March 2009. 2009.

Appendix

A1 Penetration depth

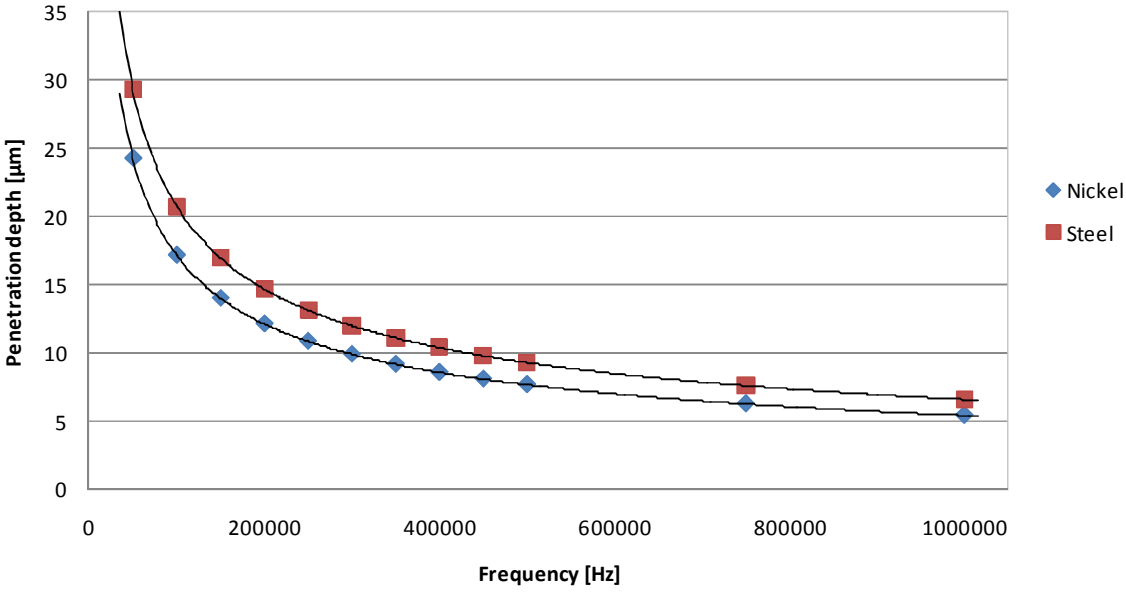

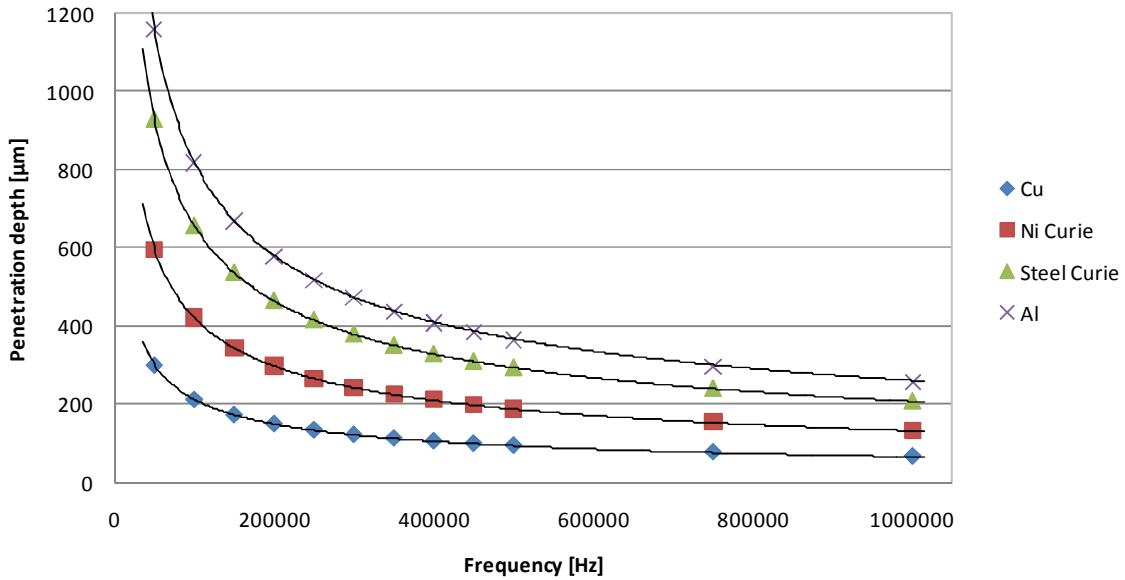

A2 Test Setup

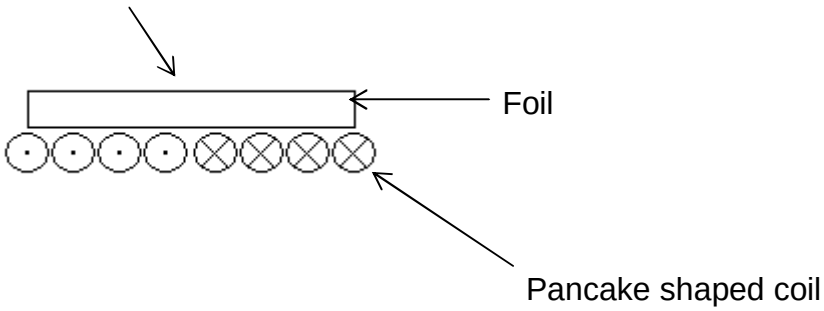

The questions we would like to be answered are:

Is it possible to heat up the foils using induction heating?
Does the temperature at top of the foil reach 250℃ ?
How long does it take to reach 250℃?
What is the highest possible temperature?
How long does it take to reach this temperature?

A3 Differential Scanning Calorimetry (DSC)

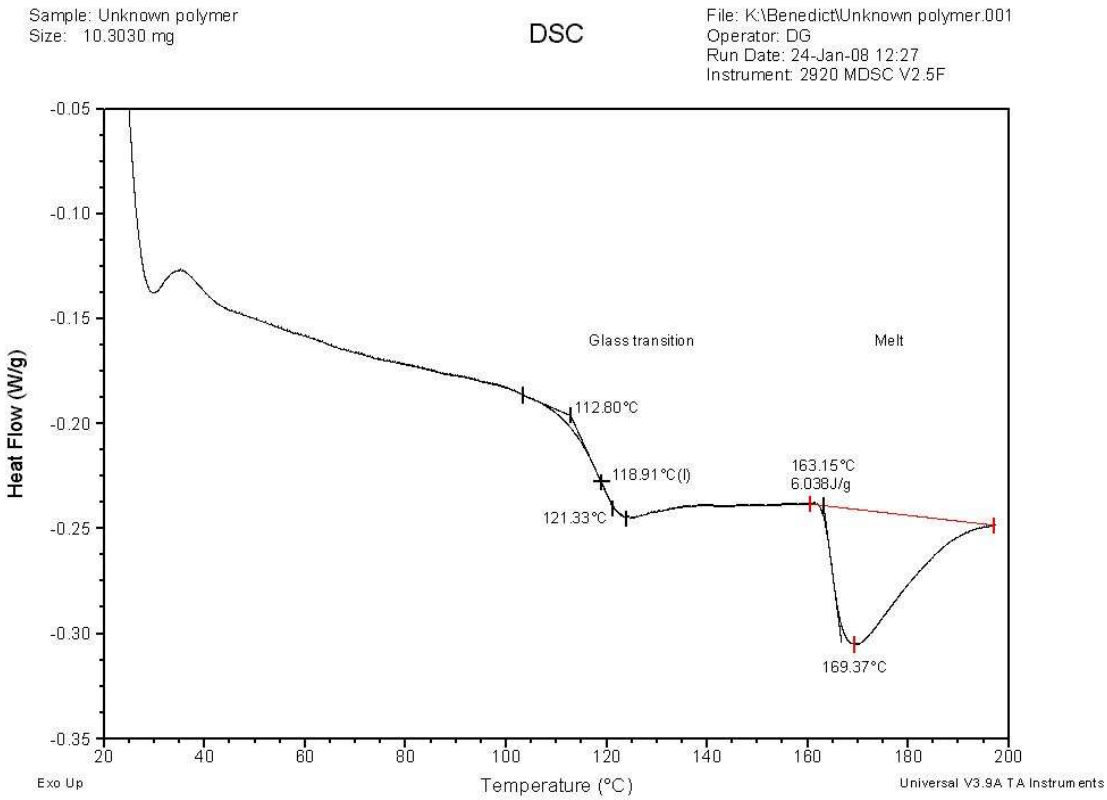

A4 Recipes for Electrolyte Bath

A4.1 Watts Nickel Bath

Composition: NiSO4.6H2O: 330 g/L
NiCl2.6H2O: 45 g/L
H3BO3: 37 g/L

Temperature: 55 ℃
pH = 4
Recommended current density during plating process: 500 A/m2

A4.2 Nickel Sulfamate Bath

Composition: Nickel Sulfamate: 350 g/L
H3BO3: 35 g/L

Temperature: 50 ℃
pH = 3.5
Recommended current density during plating process: 6 A/dm2

A5 Test Series at Hüttinger Elektronik

Time [s]	Output Power [%] of Pmax	Tmax ℃
5	20	<75
5	40	<75
5	50	95
5	60	123
5	70	140
5	80	170
5	85	175
7.5	80	195
10	80	195
15	80	210
7.5	85	200
7.5	90	205
7.5	95	218
7.5	100	228
25	100	260

A6 COMSOL Models

A6.1 Eddy Current Model

COMSOL package: AC / DC Module; Quasi-Statics, Magnetic; Azimuthal Induction Currents, Vector Potential; Time-harmonic analysis

Workpiece:	Steel disc	
	Radius:	100mm
	Thickness:	100μm
Inductor coil:	Point source	
	Radius:	40mm
	Current:	140A or varied 1A-500A
	Frequency:	220kHz
Working distance:		60mm or varied 25mm-50mm

A6.2 Induction Heating Model

COMSOL package: AC / DC Module; Electro-Thermal Interaction; Azimuthal Induction Heating; Transient analysis

Workpiece:	Steel disc	
	Radius:	100mm
	Thickness:	100μm
Inductor coil:	Point source	
	Radius:	40mm
	Current:	140A or varied 1A-500A
	Frequency:	220kHz
Working distance:		60mm or varied 25mm-50mm
Heating time:		5s or varied 0s-5s
Note:	Temperature dependence of resistivity was ignored	

A6.3Modelling Area Effects

COMSOL package: AC / DC Module; Electro-Thermal Interaction; Azimuthal Induction Heating; Transient analysis

Workpiece:	Copper disc	
	Radius:	varied 1mm-80mm
	Thickness:	1mm
Inductor coil:	Point source	
	Radius:	100mm
	Current:	2kA
	Frequency:	200Hz
Working distance:		20mm
Heating time:		200s
Note:	Temperature dependence of resistivity was included (equation 3-5)	

A6.4Modelling Effect of Permeability

COMSOL package: AC / DC Module; Electro-Thermal Interaction; Azimuthal Induction Heating; Transient analysis

Workpiece:	Copper ring	
	Radius:	inner: 3mm
		outer: 4.5mm
	Thickness:	7.5µm; 1mm
Inductor coil:	Point source	
	Radius:	40mm
	Current:	490A
	Frequency:	220kHz
Working distance:		20mm
Heating time:		10s

Note: Workpieces' permeabilities were set to 1 and 100; Temperature dependence of resistivity was included (equation 3-5)

A6.5Modelling Effect of Air Gaps

COMSOL package: Heat Transfer; Convection and Conduction; Steady-state analysis

Model design:

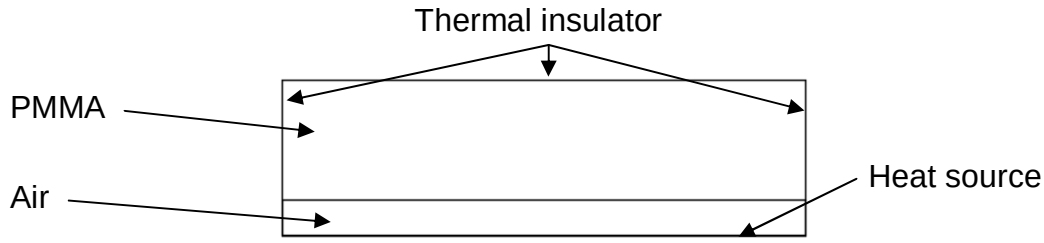

Figure 0-1. COMSOL model for simulating heat conduction with boundary conditions

PMMA:	Size of area: 20mm x 2mm
Air:	Size of area: 20mm x [0µm; 5µm; 20µm; 100µm]
Heat source:	400K
Heating time:	10s
Note:	Thermal conductivity was constant